Sister Rod Destructive Examinations (FY23)

Appendix E: Mechanical Testing

Spent Fuel and Waste Disposition

Prepared for
US Department of Energy
Spent Fuel and Waste Science
and Technology

Oak Ridge National Laboratory
Rose Montgomery,
Paul Cantonwine, Oscar Martinez,
Muhammet Ayanoglu, Darren Skitt,
Yong Yan, Ben Garrison,
Ricardo Muse, Dominic Giuliano

January 31, 2024
M2SF-24OR010201024
ORNL/TM-2023/3184

SUMMARY

This report documents work performed under the Spent Fuel and Waste Disposition's Spent Fuel and Waste Science and Technology program for the US Department of Energy (DOE) Office of Nuclear Energy (NE). This work was performed to fulfill Level 2 Milestone M2SF-24OR010201024, "FY23 ORNL Testing on Sibling Pins," within work package SF-24OR01020102 and is an update to the work reported in M2SF-23OR010201024, M2SF-22OR010201047, M2SF-21OR010201032, M2SF-19ORO010201026, and M2SF-19OR010201028.

As a part of the DOE NE High Burnup Spent Fuel Data Project, Oak Ridge National Laboratory (ORNL) is performing destructive examinations (DEs) of high burnup (HBU) (>45 GWd/MTU) spent nuclear fuel (SNF) rods from the North Anna Nuclear Power Station operated by Dominion Energy. The SNF rods, called *sister rods* or *sibling rods*, are all HBU and include four different kinds of fuel rod cladding: standard Zircaloy-4 (Zirc-4), low-tin Zirc-4, ZIRLO, and M5. The DEs are being conducted to obtain a baseline of the HBU rod's condition before dry storage and are focused on understanding overall SNF rod strength and durability. Composite fuel and defueled cladding will be tested to derive material properties. Although the data generated can be used for multiple purposes, one primary goal for obtaining the post-irradiation examination data and the associated measured mechanical properties is to support SNF dry storage licensing and relicensing activities by (1) addressing identified knowledge gaps and (2) enhancing the technical basis for post-storage transportation, handling, and subsequent disposition.

This report documents the status of the ORNL Phase 1 DE activities related to the mechanical testing of selected sister rods in Phase 1 of the sister rod test program.

Table ES-1 summarizes the mechanical test status.

Table ES-1. DE status.

Planned DE		**Status**	**Comments**
DE.07	Conduct four-point bend (4PB) tests	In progress	(FY21) All Phase 1 tests are complete except for those planned for aerosol collection. Tests were conducted at room temperature (RT) and at 200°C. Data evaluation is in progress. The flexural strength and strain at fracture, 0.2% offset yield strength, and flexural modulus were calculated for the tests completed. Generally, the heat-treated M5 and ZIRLO-clad specimens have higher ductility than the baseline specimens. The mass loss from the specimen resulting from fracture was measured during the 4PB tests. There was no trend of pellet mass loss related to test temperature, although the RT fractures seemed more energetic than the 200°C fracture. Each pellet weighed approximately 5.1–7.0 g, so the maximum mass released from the cladding represents about ¼ of a pellet, whereas the more typical 0.4 g mass released is less than ⅒ of a full pellet. The uncertainty of the 4PB test in ORNL's configuration was calculated and integrated with the results. In the process of calculating the uncertainties, errors in the stress and strain

Planned DE		Status	Comments
			calculation results tabulated in the 11/30/2020 report were found and corrected. (FY22) Five RT tests remain to be completed in conjunction with aerosol testing. To better understand the results of the 4PB tests and the functionality of the pellet in the composite rod in bending, finite element models of the test segment with an explicit crack geometry were developed. The results indicate that pellet-to-cladding bonding and pellet cracks play a large role in the strength of the composite rod. A more realistic crack geometry will be used to further refine the model in FY23. These results provide important insight for higher order simplified modeling of the larger system in transportation or other scenarios. Unfortunately, the Instron load frame succumbed to the high radiation environment in the hot cell early in FY22 and is no longer functional. (FY23) A replacement load frame has been procured and is expected to be available for continued testing in FY24. In the meantime, a load frame was developed and fabricated by ORNL for use in four-point bend testing with aerosol collection. One test was completed in FY23 and the results will be reported in FY24.
DE.08	Conduct axial tensile tests	In progress	(FY21) ORNL tested a specimen available from a previous program (M5 clad pressurized water reactor [PWR] rod). Four trials were performed, and the specimen broke every time at the clamp on the upper axial tension jaws. This indicates a sensitivity of the cladding and is consistent with Pacific Northwest National Laboratory's (PNNL's) experience. An alternative method to clamp the specimens in the load frame is being investigated. (FY22) A new grip was procured, and out-of-cell testing is underway. In cell tests must wait for a new load frame to be installed. (FY23) The tensile grip was further evaluated out-of-cell and waits for the new load frame.
DE.09	Test for American Society for Testing and Materials (ASTM) microhardness	In progress	In FY21, microhardness tests were performed on one defueled polished sample prepared from segment F35P17-2735-2754 (heat-treated Zirc-4 cladding). Each quadrant of the cladding (Quad A, B, C, D) was indented across its thickness, and a fifth test was performed at a location where extensive waterside oxide spalling occurred (Quad AB). The

Planned DE		**Status**	**Comments**
			measured HV increased from cladding ID to OD across the cladding thickness and ranged from 251± 9 to 298± 11 HV. The oxide layer was found to be significantly harder than the base cladding, at an average measured HV of 947 ± 67. The results are consistent with those from PNNL. (FY22) 8 specimens (28 indents per specimen) were tested with a total of 224 indents performed and the results are consistent with previous tests. The hardness of LT Zirc-4, Zirc-4, and ZIRLO are well correlated with local burnup, while M5 has a relatively flat hardness near 230 HV. Although there are differences in hardness between the FHT and baseline samples, the source of the difference is not clear, and the difference is very near the measurement uncertainty. (FY23) A replacement microhardness tester has been procured and will be ready for hot cell use in FY24.
DE.10	Conduct fueled ring compression tests (RCTs)	Complete	(FY21) Fueled RCTs are complete. There is no appreciable difference in the maximum load-bearing capability of the segments from RT to 200°C. Cladding type also does not greatly influence the load-bearing capability, and there does not appear to be a difference related to the heat-treatment applied to some of the rods. The main observed variant is the orientation of the major cracks in the pellet because these appear to nucleate fracture of the adjacent cladding and determine the pellet fracture plane. The observed transverse bearing load of the specimen is 16.4 kN (3,690 lb_f) on average, with a minimum load-bearing capability of 12.3 kN (2,766 lb_f) for the tested segments. (FY22) Finite element analyses of the RCT test were performed to better understand the results of the fueled RCT tests and the functionality of the pellet in the transverse compression. The models of the test segment include an explicit crack geometry and the results indicate that pellet-to-cladding bonding and pellet cracks play a large role in the strength of the composite rod. (FY23) Additional refinements of the finite element model have improved the model's ability to match the observed behavior.
DE.14	Perform burst tests	Discontinued by the project	(FY21) Existing equipment at the Irradiated Fuels Examination Laboratory (IFEL) is not capable of achieving the pressures needed at the proposed test temperatures. ORNL is collaborating with PNNL to design a new system to pressurize segments for burst that is similar to their system for cladding burst, with the exception that ORNL

Planned DE		Status	Comments
			will use a gas. With a basic design in hand, ORNL plans to acquire the necessary equipment in FY22. (FY22) ORNL has developed a pressurization system; however, pressures high enough to induce burst have not been possible with this system. Further development is required. (FY23) This work scope has been eliminated.

ACKNOWLEDGMENTS

Many thanks to our US Department of Energy Office of Nuclear Energy sponsor Ned Larson, along with the Spent Fuel and Waste Science and Technology storage and transportation program leadership for their continued support. The sister rod project would not have been possible without the vision and support of the Electric Power Research Institute, Westinghouse, Framatome, and Dominion Energy.

This work would not have been possible without the support and expertise provided by the leadership and staff members of the ORNL’s Irradiated Fuel Examination Laboratory. Special thanks go to Jerid Metcalf, Scott Thurman, John Hinds, and Brian Woody for their assistance with in-cell testing activities. Rick Henry, and now Martino Hooghkirk, have the unenviable task of tracking the bits and pieces of sister rods and their moves around the hot cell and to other facilities, and we very much appreciate his patience and continued support. Jim Miller, Mark Delph, and Russ Smith have been vital in supporting the deployment of new equipment to the cell, and we appreciate their continued support.

This page is intentionally left blank.

CONTENTS

This page is intentionally left blank.

LIST OF FIGURES

LIST OF TABLES

This page is intentionally left blank.

REVISION HISTORY

Date	Changes
10/29/2020	This appendix contains new information on the mechanical testing results.
11/30/2020	Comments received on the 10/29/2020 draft were incorporated, and the document numbering was revised to reflect its M2 status.
10/29/2021	The appendix has been revised to incorporate new data (Section E-4) and to correct calculated results of the 4PB tests (modified Table E-2 and Figs. E-10 through E-13, added Fig. E-14). Minor changes in the text were made in Sections E-3, E-6, E-2.6, and E-2.4. The summary has been updated.
3/31/2022	Comments received on the 10/29/2021 draft were incorporated, the document number was revised to reflect its M2 status, and the document date was changed. More information was added in section 2.1.4 relative to the use of elastic beam theory in the four point bend data reduction.
10/28/2022	Table ES-1 has been updated to include work completed since the last report; the last paragraph of section E-1 was added; Section E-2.4 has been added (Finite element modeling of 4PB test results); Section E-3 was added, and Section E-4 has been modified to include new data.
1/13/2023	Comments received from the team were incorporated throughout and the document ID number was revised to reflect its M2 status and the issue date was changed.
10/31/2023	Updated sections E-1, E-2, E-5.4, and E-6.
1/31/2024	The document was updated to incorporate comments received and the document ID number was revised to reflect its M2 status. The issue date was changed.

This page is intentionally left blank.

ACRONYMS

4PB	four-point bend
ANL	Argonne National Laboratory
ASTM	American Society for Testing and Materials
CIRFT	cyclic integrated reversible-bending fatigue tester
DE	destructive examination
DOE	US Department of Energy
EI	flexural rigidity
FHT	full-length fuel rod heat treatment
HBU	high burnup
HV	Vickers hardness
IFEL	Irradiated Fuels Examination Laboratory
LAMDA	Low Activation Materials Development and Analysis
LT	low tin
MET	metallography
NDE	nondestructive examination
NE	Office of Nuclear Energy
ORNL	Oak Ridge National Laboratory
PNNL	Pacific Northwest National Laboratory
PWR	pressurized water reactor
RCT	ring compression test
RT	room temperature
SNF	spent nuclear fuel

This page is intentionally left blank.

E-1. Mechanical Test Frame Installation

As a part of the US Department of Energy (DOE) Office of Nuclear Energy (NE) High Burnup Spent Fuel Data Project [E-1], Oak Ridge National Laboratory (ORNL) is performing destructive examinations (DEs) of high burnup (HBU) (>45 GWd/MTU) spent nuclear fuel (SNF) rods from the North Anna Nuclear Power Station operated by Dominion Energy. The SNF rods, called *sister rods* or *sibling rods*, are all HBU and include four different kinds of fuel rod cladding: standard Zircaloy-4 (Zirc-4), low-tin (LT) Zirc-4, ZIRLO, and M5. The Phase 1 DEs [E-2, E-3] are being conducted to obtain a baseline of the HBU rod's condition before dry storage and are focused on understanding overall SNF rod strength and durability. Composite fuel and defueled cladding will be tested to derive material properties. Although the data generated can be used for multiple purposes, one primary goal for obtaining the post-irradiation examination data and the associated measured mechanical properties is to support SNF dry storage licensing and relicensing activities by (1) addressing identified knowledge gaps and (2) enhancing the technical basis for post-storage transportation, handling, and subsequent disposition.

To provide the capability for mechanical testing, a large Instron load frame (65 × 31 × 29 in.) with a 30 kN capacity (~1 ton of loading force) was installed in the Irradiated Fuels Examination Facility (IFEL) north hot cell. The cell location was selected based on its accessibility and its lower dose rates (~150 R/h).

During FY20, the load frame was modified for durability in the radiation field and to provide remote manipulation capabilities. Lead shielding was placed around the load frame's instrumentation string to provide more protection from radiation damage.

The load frame was successfully installed in the cell in June 2020. It was carefully rigged, lifted, and transported to the hot cell loading bay (Figure E-1, left) where it was placed on a forklift. The rigging was left in place for in-cell handling. The load frame was moved to the hot cell charging area and was then moved into the cell using the primary airlock (Figure E-1, right). From there, the in-cell crane used the same rigging to lift the load frame and move it to the north cell operating position, as shown in Figure E-2 (left). Standard bubble levels were used to check the level and plumb of the installed load frame.

To connect the control unit in the operating area of the hot cell with the load frame in the cell, instrumentation and power cabling were run through the cell's 3 ft thick wall using a service plug. As shown in Figure E-2 (right), this required removing the existing plug—which momentarily left an open path from the hot cell interior to the operating area—and then replacing it with the new plug. All cables were preinstalled in the service plug, and it was sealed before the evolution. The challenge was to install the heavy lead-shielded service plug without damaging the cables.

After the load frame was installed in the hot cell, it was cycled through several tests using surrogate materials to verify its operation.

Unfortunately, the Instron load frame succumbed to the high radiation environment in the hot cell early in FY22 and is no longer functional. A replacement load frame has been procured and is expected to be available for continued testing in FY24.

In the interim, the "MiniMight," shown in Figure E-3 was designed and fabricated to provide a load frame for the 4PB tests within the limited hot cell space and within the near-term time frame. The MiniMight consists of a load frame constructed out of 0.25 in. thick 304 stainless-steel tubing, a DC electric motor driven linear actuator, a load cell at the bottom of the unit, an LVDT, and an Instron four-point bend fixture consisting of an upper and lower anvil. The LVDT provides the necessary crosshead travel data and was manufactured by Alliance Sensors Group, model LVE45-100R-01-10S. It has a 100 mm stroke, 0–10 VDC output, 12–30 VDC input, with a sensor resolution of 0.025% of full scale, ±0.15% linearity, and uses 5 wires on a 5-pin M12 quick disconnect. It measures the relative displacement of the upper four-point bend anvil. The bottom of the MiniMight contains the load cell, lower anvil (connected with lower 4PB fixture anvil coupling), and aerosol collection box. The load cell is a model 1100 series ultra-precision low profile load cell with a load capacity of 5 kN. The anvil is coupled to the lower anvil, which is a stock Instron (2810-400A1) lower support anvil with a load capacity of 5kN. The aerosol collection box sits on the lower anvil.

The force is applied to the test piece by the combination direct current (DC) brushed gear motor and screw-driven linear actuator. The DC brushed gear motor provides a continuous torque of 50 N-m (443 in.–lb) at a maximum speed of 0.3 RPM which is achieved through the 2,076:1 gear head reduction. The DC gear motor was chosen over other motor options because of its robustness, radiation tolerance, and low number of required wires. It is mechanically mounted and coupled to a Versatile Thrust (VT) screw-driven linear actuator, part number VT320S-06-FF-F-L0-00-x00, from EDrive. The combination gear motor and linear actuator produces a thrust which is limited by the actuator construction of 8.9 kN and can be applied at a velocity between 1 and 3 mm/min with a stroke of 6 inches.

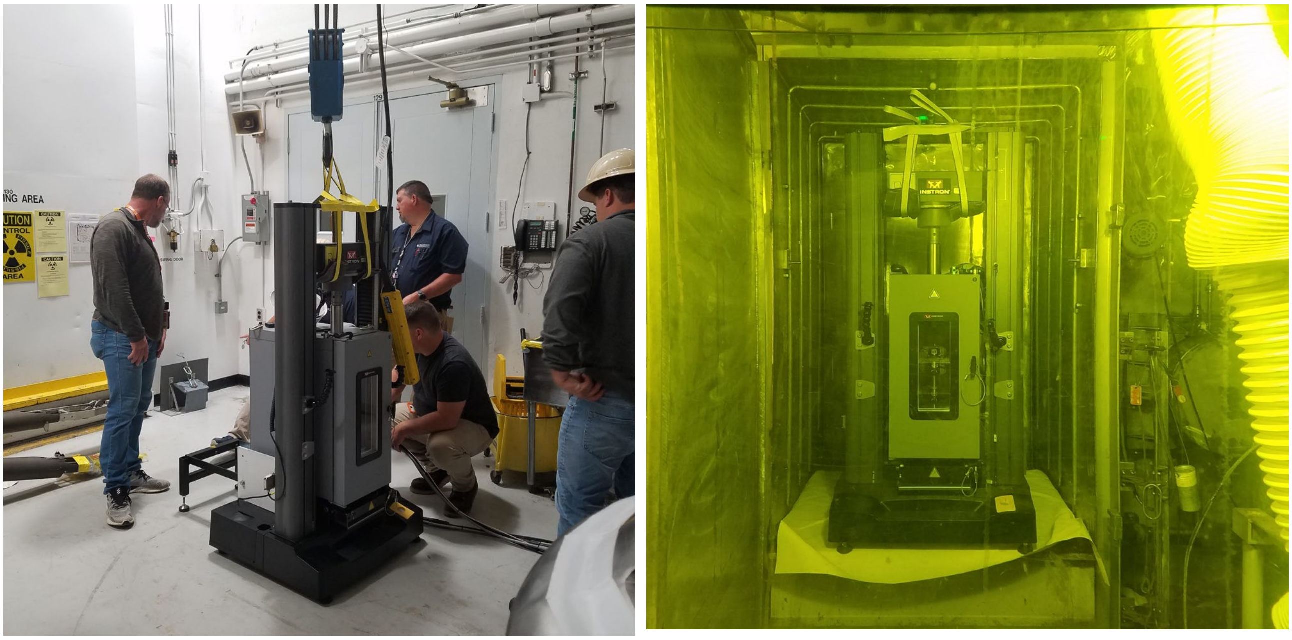

Figure E-1. The Instron load frame and furnace were moved to the hot cell loading bay (left) and into the hot cell through the cell's primary airlock (right).

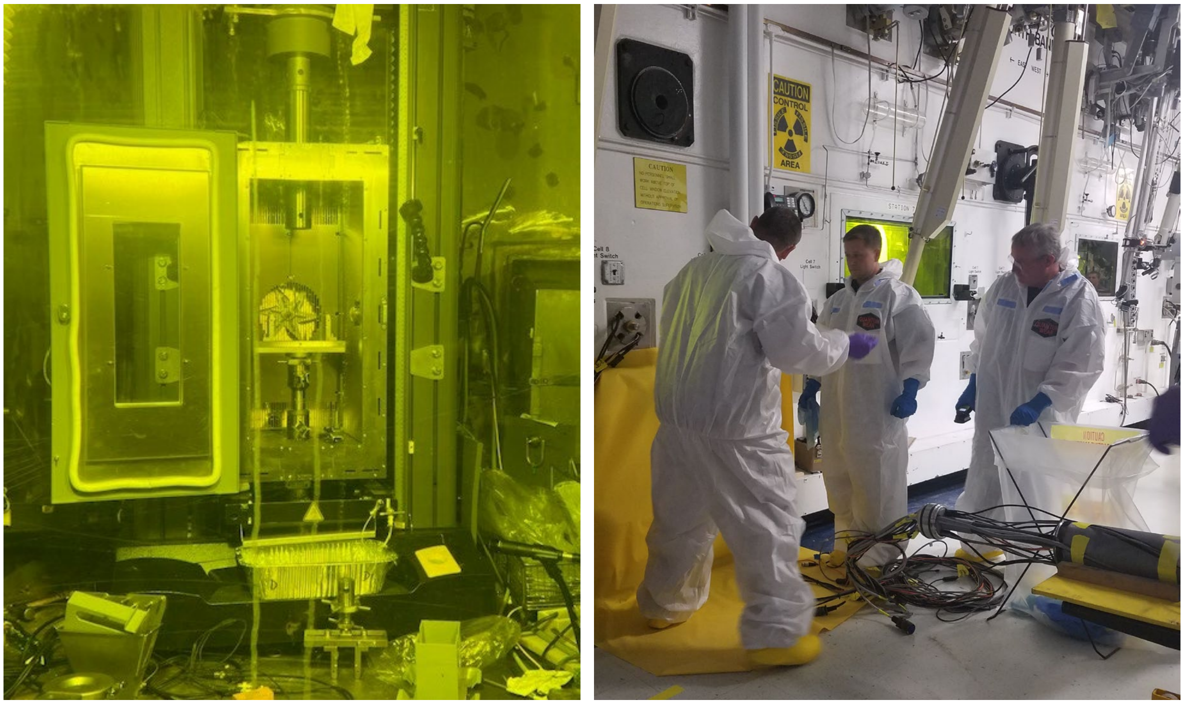

Figure E-2. The Instron load frame and furnace were placed in the north hot cell (left), and the service plug containing all instrumentation and power was installed (right).

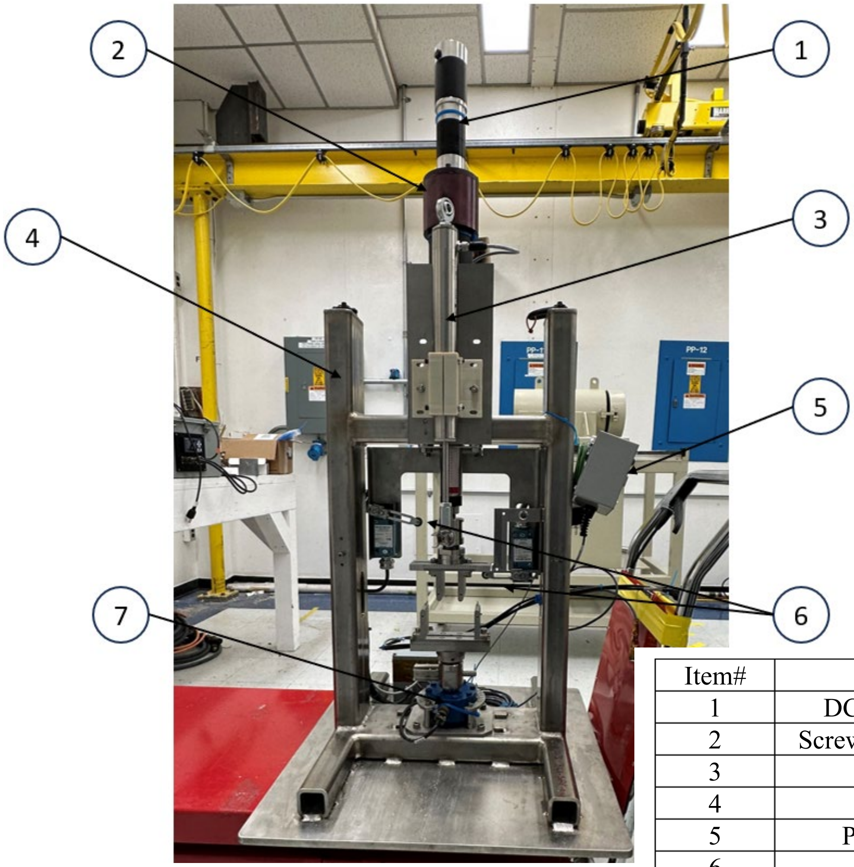

Item#	Description
1	DC brushed gear motor
2	Screw driven linear actuator
3	LVDT
4	Structural frame
5	Pressure connection
6	Limit switch
7	Load cell

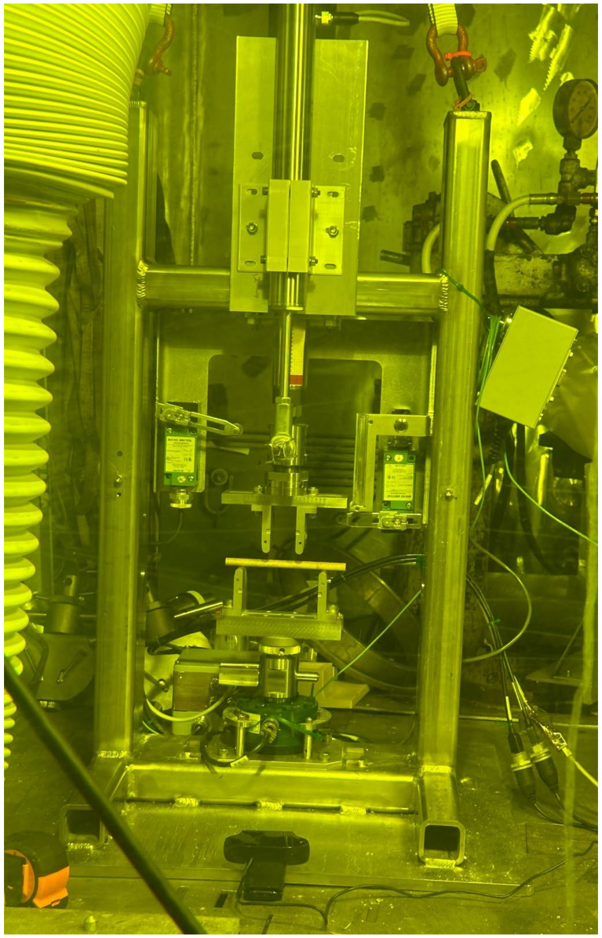

Figure E-3. MiniMight load frame for 4PB with aerosol collection tests (left) and its basic configuration; (right) as installed in the IFEL North hot cell.

E-2. Four-Point Bend Tests

The four-point bend (4PB) test provides values for the modulus of elasticity in bending (the *flexural modulus*), as well as the flexural stress and flexural strain response. It is traditionally the test used to study brittle materials in which the number and severity of flaws exposed to the maximum stress is directly related to the flexural strength and crack initiation.

ORNL is testing fuel rod segments with pellets (termed a “composite rod) and PNNL is testing the defueled cladding. The composite rod’s performance is different from the empty cladding’s performance. The presence of the pellets is expected to provide stiffening and support to the cladding, but the discontinuities inherent in the pellets also locally increase stress in the cladding. Therefore, the results of the ORNL composite rod tests can be compared with the PNNL defueled cladding tests to provide an indication of the overall strength of the composite rod and the inherent effect of the pellets, but the composite rod test results should not be construed as cladding properties.

Several ASTM standards are available for 4PB, including Standard Test Method for Flexural Strength of Advanced Ceramics at Ambient Temperature[E-4] and Standard Test Methods for Flexural Properties of Polymer Matrix Composite Materials [E-5], which were used to guide selection of the fixture geometry and test gauge length. There is not a specific ASTM test method to measure the flexural properties of SNF rods, but ASTM C1161 [E-4] and ASTM D7264/D7264M [E-5] provide guidance and information used to inform the approach used to test the spent fuel rod segments. The ASTM guidelines for these tests typically call for rectangular specimens, while the shape of the fuel rods tested can be generalized as cylindrical. ASTM C1161 discusses the use of a four-point bend test on single-material ceramic coupons and ASTM D7264/D7264M addresses testing of multi-material coupons such as fiber-reinforced polymers. The fuel rod segments being tested are composites consisting of multiple pellets within a cladding, and as discussed by ASTM D7264/D7264M, no composite material is perfectly symmetric. Additionally, the pelleted rods contain many discontinuities that can affect local stress, such as the end features on the pellets (chamfers and dishes), cracks in the pellets developed during reactor operation, bonded areas between the pellets and the cladding, and cladding precipitated hydrides.

Room temperature (RT) and 200°C tests were completed. The list of specimens is provided in Table E-1. Video and audio records of the tests were acquired, along with the displacement and load results. Each test segment was weighed before testing. A tray was placed below the specimen to catch debris, and the broken segments and debris were weighed after each test.

Several 4PB tests will be completed with the aerosol collection system to better quantify the size distribution and quantity of aerosol particles released during fracture. The aerosol tests have not yet been completed, as discussed in Appendix I.

The load frame and associated test fixturing (shown in Figure E-4) applies load at four points on the fuel rod specimen. The upper fixture is advanced at a selected fixed displacement rate in the downward direction, whereas the lower fixture is fixed and does not move. The fixture used is standard off-the-shelf equipment for 4PB, except that wire stops were added to ensure that the rod would not roll off the back of the fixture before the test could start. For tests at temperature, the load frame’s furnace is pulled forward. The specimen is placed on the fixture, and the two are heated simultaneously to the test temperature. The stock furnace thermocouple was used to measure chamber temperature, and a minimum 15 minutes of hold time at temperature was allotted to let the fixture and specimen reach steady state. ASTM C1161–18 [E-4] and ASTM D7264/D7264M–15 [E-5] were used in setting up and evaluating the test data. ASTM E8/E8M–16a [E-6] was used in evaluating the 0.2% offset yield strength.

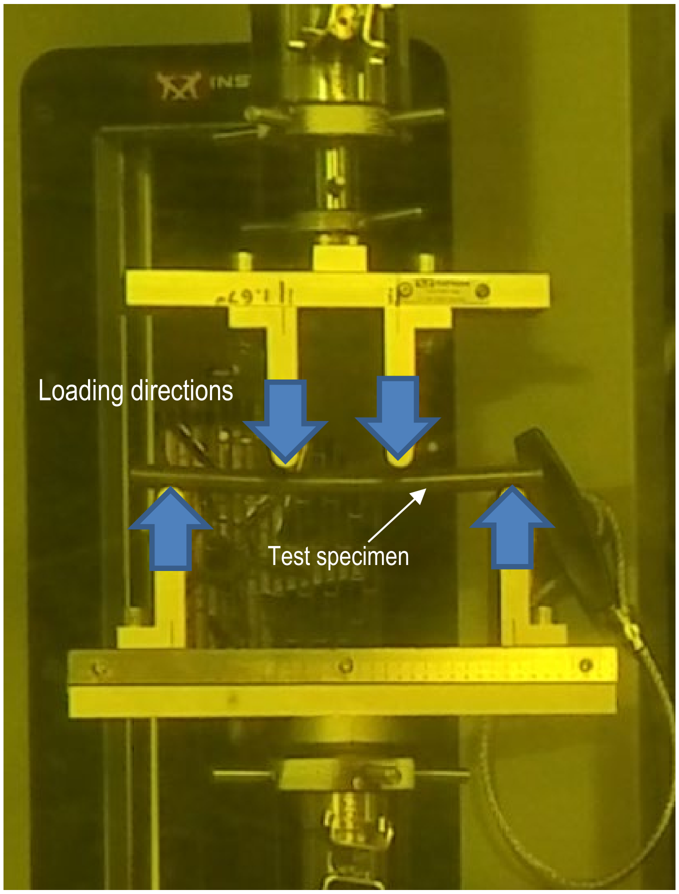

Figure E-4. The load frame configured for 4PB tests of a sister rod specimen.

Table E-1. List of specimens for 4PB.

Specimen ID#			Cladding alloy	Test temp. (°C)	Specimen heat treatment before test	Specimen average burnup (GWd/MTU)	Specimen average oxide thickness (µ)	Test status
30AD05	850	1003	M5	200	None	60	3	Complete
30AD05	1003	1156	M5	RT	None	60	3	Future test with aerosol collection
30AD05	1299	1452	M5	RT	None	60	4	Complete
30AD05	1800	1953	M5	200	None	59	4	Complete
30AE14	825	978	M5	200	FHT[*]	58	4	Complete
30AE14	978	1131	M5	RT	FHT	59	4	Complete
30AE14	1800	1953	M5	RT	FHT	60	9	Future test with aerosol collection
30AE14	2050	2203	M5	200	FHT	60	10	Complete
3D8E14	872	1025	ZIRLO	200	None	64	10	Complete
3D8E14	1025	1178	ZIRLO	RT	None	64	11	Complete
3D8E14	1907	2060	ZIRLO	200	None	64	21	Complete
3D8E14	2810	2963	ZIRLO	RT	None	63	41	Complete
3F9N05	872	1025	ZIRLO	200	FHT	59	10	Complete
3F9N05	1910	2063	ZIRLO	200	FHT	59	23	Complete
3F9N05	2063	2216	ZIRLO	RT	FHT	59	28	Complete
3F9N05	2882	3035	ZIRLO	RT	FHT	58	46	Future test with aerosol collection
3A1F05	1279	1432	LT Zirc-4	RT	None	57	23	Complete
3A1F05	1432	1585	LT Zirc-4	200	None	56	34	Complete
3A1F05	2230	2383	LT Zirc-4	200	None	54	72	Complete
3A1F05	2402	2555	LT Zirc-4	RT	None	55	117	Complete
F35P17	1319	1472	Zirc-4	RT	FHT	52	26	Complete
F35P17	1472	1625	Zirc-4	200	FHT	53	37	Complete
F35P17	2230	2383	Zirc-4	200	FHT	51	72	Complete
F35P17	2402	2555	Zirc-4	RT	FHT	52	117	Future test with aerosol collection

[*] FHT = full-length fuel rod heat treatment

E-2.1 Test Procedure and Data Processing

E-2.1.1 Test Protocol

Instrument and software testing equipment description:

Load frame	Instron 5967
Bend fixture capacity:	30 kN
Voltage:	110/220 V
Software:	Bluehill-3
Furnace:	CP122117 Environmental Chamber and Control Unit
Furnace max temperature:	≤400°C
Scale:	Ohaus Scout NV1201

The 4PB fixture was adjusted and the fixed positions measured before being inserted into the hot cell. The lower support positions are fixed at 5 in. center-to-center, and the upper loading positions are fixed at 1.67 in. center-to-center. The upper fixture is centered on the lower fixture, providing a symmetric loading of the rod specimen. Calibration of the Instron load cell and displacement and uncertainty evaluations for the four-point bend test are provided in Appendix H of this report.

Each test specimen is stored separately, and only one specimen is removed from its labeled storage container at a time. Each specimen is weighed and then placed on the lower 4PB support fixture and pushed back until it rests against the provided stops. The upper 4PB fixture is lowered to within ~1⁄32 in. of the top of the test specimen.

If the test will be at temperature, then the furnace door is closed, and heating is initiated. During heating, the upper 4PB fixture is raised as needed to avoid preload of the specimen caused by thermal expansion of the system.

Once the system is at the specified temperature, the upper 4PB fixture is lowered to contact with the test specimen, as indicated by an increase in load. Care is taken to keep the amount of initial loading small.

The test system is then zeroed, and the test is initiated. All tests are run using a fixed displacement speed of 0.050 mm/s. The load and crosshead displacement are collected for the entire test, and the test proceeds until the specimen is fractured.

Following fracture, the specimen, as defined by the fueled pieces within the cladding, is weighed. Any loose particles are weighed. The post-test specimen is placed in a labeled capsule and returned to storage.

E-2.1.2 Corrections for Machine Compliance

The load vs. crosshead extension data necessarily includes information on machine compliance. When the load frame applies a force, the entire system, including the frame, load cell, grips, couplings, and specimen, experiences some amount of deflection. The load frame's reported displacement is the sum of the entire system's deformation. To determine the displacement of the specimen only, the machine compliance (deformation associated with the load frame, load cell, and grips) is removed from the load frame's reported displacement data.

Machine compliance is measured by testing a rigid specimen using the 4PB setup. In this case, a high-strength steel rod (OD = 2.00 in.) was used. The corrected displacement is calculated by subtracting the displacement reported in the machine compliance test from the displacement reported in the test of each sister rod specimen.

Because the 4PB specimen fractures at a load that is much lower than the load frame's limit (typically less than 10% of capacity), the corrections made to the 4PB displacements are small.

E-2.1.3 Test Specimen

Rough-cut 152 mm (6 in.) long fueled segments are used directly for 4PB. The specimens are unpressurized and have open ends.

E-2.1.4 Data Reduction

The 4PB test can be evaluated using simple beam theory given the nominal dimensions of the rod specimen and test fixture, idealizing the composite fuel rod segment as a solid cylindrical geometry made of an isotropic material. The uncertainties associated with these assumptions are discussed within this Appendix E and are further evaluated with respect to the measurement uncertainty in Appendix H of this report.

The four-point loaded beam is preferred for determining strength properties because the center span is uniaxially stressed (i.e., no shear stresses exist). The bending moment applied is constant over the inner span between the two upper fixture loading points. The load applied on the specimen at each fixture loading point, P, is half the load recorded by the load frame. The deflection of the specimen at the loading points, Δ_f, is the measured crosshead displacement of the upper test fixture recorded by the load frame minus the machine compliance.

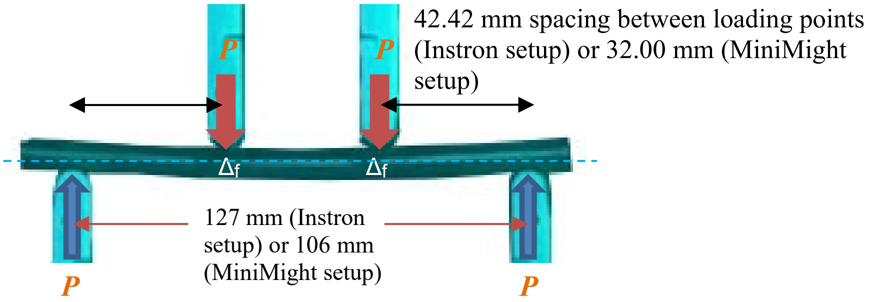

Figure E-5. Simple beam representation of the 4PB test.

The idealized composite rod performance is evaluated using classical elastic beam theory. As a reminder, many of the assumptions inherent in beam theory are not met within the composite rod, including the following:

- As previously discussed, an SNF composite rod is not a homogeneous isotropic material.
- Transverse planes perpendicular to the longitudinal axis of the composite rod might not remain planar after it is deflected because of the many cracks and discontinuities inherent in the pellet stack.
- It is unclear whether any local plastic strain or twist of the rod occurs during the test.

Nevertheless, beam theory is used to provide points of comparison of the SNF composite rod response under a bending load with other engineered materials.

Data reduction equations are provided for both the Instron setup and the MiniMight setup. To determine the maximum stress and strain on the specimen, the maximum bending moment between the upper loading points, M_{max}, is calculated using the spacing between the fixed support and the moving loading points and the load at each loading point (the load reported by the load frame divided by two):

$$42.42\ mm\ P \text{ (Instron) } \underline{\text{or}}\ 32.00\ mm\ P \text{ (MiniMight).} \tag{E-1}$$

Using classical beam theory, Δmax, the maximum beam deflection at the idealized rod's axial center, can be calculated as

$$\frac{Pa}{24EI}(3l^2 - 4a^2) = \frac{42.42\ mm\ P}{24EI}(3[127\ mm]^2 - 4[42.42\ mm]^2) \text{ for Instron, } \underline{\text{or}} \tag{E-2}$$
$$\frac{Pa}{24EI}(3l^2 - 4a^2) = \frac{32.00\ mm\ P}{24EI}(3[106\ mm]^2 - 4[32.00\ mm]^2) \text{ for MiniMight}$$

where *E* is the elastic modulus of the idealized fuel rod (assuming that it is a single material having a solid circular cross-section), and *I* is the first moment of inertia, approximated as $\frac{1}{4}\pi\left(\frac{OD}{2}\right)^4 \approx\ 400\ mm^4$; the product *EI* is referred to as the idealized rod's flexural rigidity. Simplifying,

$$\Delta\max = \frac{182.1\ mm^{-1} * P\ (in\ N)}{E\ (in\ N/mm^2)} \text{ for Instron, } \underline{\text{or}} \frac{98.751\ mm^{-1} * P\ (in\ N)}{E\ (in\ N/mm^2)} \text{ for MiniMight.} \tag{E-3}$$

Δ_f can also be related to the elastic modulus of the composite fuel rod using beam theory:

$$\frac{Px}{6EI}(3la - 3a^2 - x^2),$$

which simplifies as:

$$\frac{158.5\ mm^{-1} * P\ (in\ N)}{E\ (in\ N/mm^2)} \text{ for Instron, } \underline{\text{or}} \frac{81.1\ mm^{-1} * P\ (in\ N)}{E\ (in\ N/mm^2)} \text{ for MiniMight.} \tag{E-4}$$

and allowing an estimate of the idealized single-material, solid circular section elastic modulus:

$$E = \frac{158.5\ mm^{-1} * P\ (in\ N)}{\Delta_f} \text{ for Instron, } \underline{\text{or}} \frac{81.1\ mm^{-1} * P\ (in\ N)}{\Delta_f} \text{ for MiniMight.} \tag{E-5}$$

Substituting Eq. (E-5) into Eq. (E-3) yields an estimate of the maximum deflection at the center of the 4PB specimen for use in calculating the maximum stress and strain:

$$\Delta\max = (182.1 / 158.5)\ \Delta_f \text{ (Instron setup) } \underline{\text{or}}\ (98.751/ 81.1)\ \Delta_f \text{ (MiniMight setup)} \tag{E-6}$$

The maximum stress, σ_{max}, of the idealized composite rod segment is estimated as

$$\frac{42.42\,mm\,P\,(OD/2)}{I}\text{ for Instron, }\underline{\text{or}}\ \frac{32.00\,mm\,P\,(OD/2)}{I}\text{ for MiniMight.} \qquad \text{(E-7)}$$

For more accurate estimates, the measured outer diameter (OD) of the rod at the segment elevation [E-7] is used.

The radius of curvature, ρ, is calculated using the displacements Δ_f and Δ_{max} assuming the displaced shape of the fuel rod segment in the region of pure bending is circular, as described in Appendix F, and the maximum strain on the idealized rod segment, ε, is calculated as

$$\frac{(OD/2)}{\rho}. \qquad \text{(E-8)}$$

Ideally, the elastic modulus is equivalent to the flexural, or *bending*, modulus. Realistically, these values might be different. An elastic modulus, E, is evaluated from the test data as the slope of a least-squares fit line to the stress-strain data in the elastic region, and a plastic modulus, E_p, is evaluated as the slope of a least-squares fit line to the stress-strain data in the plastic region above the evaluated yield point. The elastic and plastic average flexural rigidities are calculated by multiplying E and E_p by the tested segment's calculated I.

To summarize, idealization of the fuel rod segment as a simplified elastic beam is used here as a practical approach to evaluate the test data and allow for comparisons with other materials, but the resulting evaluated properties should not be considered cladding material properties. Also, *elastic* beam equations are used to evaluate yield strength and ultimate strength for the idealized fuel rod segment. Elastic theory isn't strictly applicable in the plastic region (here defined as the region of the load versus displacement and stress versus strain that departs from linearity), but the strain at fracture is relatively small and deviation from elastic theory is therefore expected to be small. To verify this assumption, measurements were taken in the plastic region using the visual record of the tests performed with the Instron setup. It should be noted that the video record was not planned to be used for this purpose, and not all of the video records were usable for this purpose. The measured ratio Δ_{max}/Δ_f ranged from 1.129 to 1.161 (average of 1.148 for the 7 Instron tests measured) just beyond the yield point, and from 1.127 to 1.159 (average of 1.144 for the 8 Instron tests measured) very near the point where fracture occurred. Elastic theory predicts the ratio as 1.149 for the Instron test setup used.

E-2.2 Measured Load and Displacement Data

The load vs. crosshead extension (i.e., displacement of the fixture) was recorded for each test and is provided in Figure E-6 for the baseline and heat-treated Zirc-4-clad and LT Zirc-4-clad specimens, in Figure E-7 for the baseline and heat-treated M5-clad specimens, and in Figure E-8 for the baseline and heat-treated ZIRLO-clad specimens. Figure E-9 plots the RT tests, and Figure E-10 plots the 200°C tests. Although one test with MiniMight was completed in September 2023, the data has not yet been evaluated; the results will be added with the FY24 report.

E-2.3 Calculated Stress, Strain, 0.2% Offset Yield, Flexural Strength, and Flexural Rigidity

Using the simplified elastic beam approach discussed in Section E-2.1.4, stress and strain were calculated and are graphed in Figure E-10 at RT and Figure E-11 at 200°C. The flexural modulus, modulus of rigidity (EI), 0.2% offset yield strength, and flexural strength were also calculated. The supporting measured and calculated data are summarized in Table E-2, and they are plotted with specimen average burnup in Figure

E-13 for RT tests and in Figure E-14 for 200°C tests. The uncertainty associated with these results was evaluated in Appendix H. The elastic flexural rigidity measured using 4PB is in good agreement with the dynamic rigidity measurements using the cyclic integrated reversible-bending fatigue tester (CIRFT) (see Appendix F), as shown in Figure E-15.

Based on the visual inspection of Figure E-7 and Figure E-8, the heat-treated M5 and ZIRLO-clad specimens generally have higher ductility than the baseline specimens, but it is difficult to come to any firm conclusions with the limited data available.

Table E-2. Measured and calculated 4PB data.

Test specimen	Cladding alloy	Heat-treatment	Estimated burnup (GWd/MTU) [E-7]	Test temp. (°C)	Average specimen OD [E-7]	Crosshead extension, Δ_f, at failure (mm)	Maximum deflection, Δmax, at failure (mm)*	0.2% yield strength (MPa)*	Flexural strength (MPa)
30AD05-1299-1452	M5	---	60	25.7	9.423	8.33	9.57 ± 0.09	533 ± 11	641 ± 13
30AE14-0978-1131	M5	FHT	59	26.6	9.459	11.69	13.43 ± 0.13	481 ± 10	609 ± 12
3D8E14-1025-1178	ZIRLO	---	64	25.3	9.500	7.41	8.51 ± 0.08	617 ± 12	766 ± 15
3F9N05-2063-2216	ZIRLO	FHT	59	24.7	9.471	10.64	12.22 ± 0.12	526 ± 10	717 ± 14
3A1F05-1279-1432	LT Zirc-4	---	57	26.4	9.465	7.47	8.59 ± 0.08	616 ± 12	768 ± 15
F35P17-1319-1472	Zirc-4	FHT	52	24.9	9.503	5.36	6.16 ± 0.06	555 ± 11	640 ± 13
F35P17-1472-1625	Zirc-4	FHT	53	27.2	9.531	6.52	7.49 ± 0.07	565 ± 11	693 ± 14
30AD05-0850-1003	M5	---	60	200.0	9.429	5.77	6.63 ± 0.06	405 ± 8	461 ± 9
30AD05-1800-1953	M5	---	59	200.0	9.423	6.07	6.97 ± 0.07	443 ± 9	502 ± 10
30AE14-0825-0978	M5	FHT	58	200.0	9.457	11.60	13.33 ± 0.13	401 ± 8	503 ± 10
30AE14-2050-2203	M5	FHT	60	200.0	9.454	12.11	13.91 ± 0.13	385 ± 8	502 ± 10
3D8E14-0872-1025	ZIRLO	---	64	200.0	9.497	6.91	7.93 ± 0.08	518 ± 10	644 ± 13
3D8E14-1907-2060	ZIRLO	---	64	200.0	9.492	6.97	8.01 ± 0.08	460 ± 9	583 ± 12
3F9N05-0872-1025	ZIRLO	FHT	59	200.0	9.465	7.89	9.07 ± 0.09	461 ± 9	583 ± 12
3F9N05-1910-2063	ZIRLO	FHT	59	200.0	9.469	9.15	10.51 ± 0.10	448 ± 9	588 ± 12
3A1F05-1432-1585	LT Zirc-4	---	56	200.0	9.459	5.03	5.78 ± 0.06	519 ± 10	589 ± 12
3A1F05-2230-2383	LT Zirc-4	---	54	200.0	9.480	4.91	5.64 ± 0.05	481 ± 10	550 ± 11
F35P17-2230-2383	Zirc-4	FHT	51	200.0	9.514	7.50	8.61 ± 0.08	461 ± 9	588 ± 12
			Average at RT:			8.20	9.42 ± 0.09	556 ± 11	691 ± 14
			Average at 200°C:			7.63	8.76 ± 0.08	453 ± 9	554 ± 11

Table E-2. Measured and calculated 4PB data (continued).

Test specimen	Cladding alloy	Heat-treatment	Estimated burnup (GWd/ MTU) [E-7]	Test temp. (°C)	Average specimen OD [E-7]	Failure strain (%)*	Flexural modulus (GPa)	Elastic region flexural rigidity (N-m^2)	Plastic region flexural rigidity (N-m^2)*
30AD05-1299-1452	M5	---	60	25.7	9.423	2.6 ± 0.04	57.88 ± 1.45	22.4 ± 0.5	1.9 ± 0.04
30AE14-0978-1131	M5	FHT	59	26.6	9.459	3.8 ± 0.06	57.17 ± 1.43	22.5 ± 0.5	1.1 ± 0.03
3D8E14-1025-1178	ZIRLO	---	64	25.3	9.500	2.3 ± 0.04	58.04 ± 1.45	23.2 ± 0.5	5.1 ± 0.12
3F9N05-2063-2216	ZIRLO	FHT	59	24.7	9.471	3.3 ± 0.06	55.34 ± 1.38	21.9 ± 0.5	3.9 ± 0.09
3A1F05-1279-1432	LT Zirc-4	---	57	26.4	9.465	2.3 ± 0.04	59.25 ± 1.48	23.3 ± 0.5	6.7 ± 0.15
F35P17-1319-1472	Zirc-4	FHT	52	24.9	9.503	1.7 ± 0.03	54.24 ± 1.36	21.7 ± 0.5	8.5 ± 0.20
F35P17-1472-1625	Zirc-4	FHT	53	27.2	9.531	2.2 ± 0.04	54.72 ± 1.37	22.2 ± 0.5	6.2 ± 0.14
30AD05-0850-1003	M5	---	60	200.0	9.429	2.0 ± 0.03	51.44 ± 1.29	20.0 ± 0.5	2.0 ± 0.04
30AD05-1800-1953	M5	---	59	200.0	9.423	2.0 ± 0.03	53.60 ± 1.34	20.7 ± 0.5	2.2 ± 0.05
30AE14-0825-0978	M5	FHT	58	200.0	9.457	3.7 ± 0.06	55.97 ± 1.40	22.0 ± 0.5	0.8 ± 0.02
30AE14-2050-2203	M5	FHT	60	200.0	9.454	4.6 ± 0.08	53.66 ± 1.34	21.0 ± 0.5	1.2 ± 0.03
3D8E14-0872-1025	ZIRLO	---	64	200.0	9.497	2.2 ± 0.04	54.09 ± 1.35	21.6 ± 0.5	4.7 ± 0.11
3D8E14-1907-2060	ZIRLO	---	64	200.0	9.492	2.2 ± 0.04	50.97 ± 1.27	20.3 ± 0.5	4.7 ± 0.11
3F9N05-0872-1025	ZIRLO	FHT	59	200.0	9.465	2.5 ± 0.04	50.60 ± 1.27	19.9 ± 0.5	3.5 ± 0.08
3F9N05-1910-2063	ZIRLO	FHT	59	200.0	9.469	2.9 ± 0.05	50.64 ± 1.27	20.0 ± 0.5	3.3 ± 0.08
3A1F05-1432-1585	LT Zirc-4	---	56	200.0	9.459	1.6 ± 0.03	54.27 ± 1.36	21.3 ± 0.5	7.4 ± 0.17
3A1F05-2230-2383	LT Zirc-4	---	54	200.0	9.480	1.6 ± 0.03	51.25 ± 1.28	20.3 ± 0.5	6.9 ± 0.16
F35P17-2230-2383	Zirc-4	FHT	51	200.0	9.514	2.4 ± 0.04	48.77 ± 1.22	19.6 ± 0.5	4.3 ± 0.10
Average at RT:						2.6 ± 0.04	56.66 ± 1.42	22.5 ± 0.6	5.7 ± 0.11
Average at 200°C:						2.4 ± 0.04	52.30 ± 1.31	20.6 ± 0.5	4.4 ± 0.09

* These values are based on the calculated maximum specimen deflection using elastic beam theory as described in Section E-2.1.4.

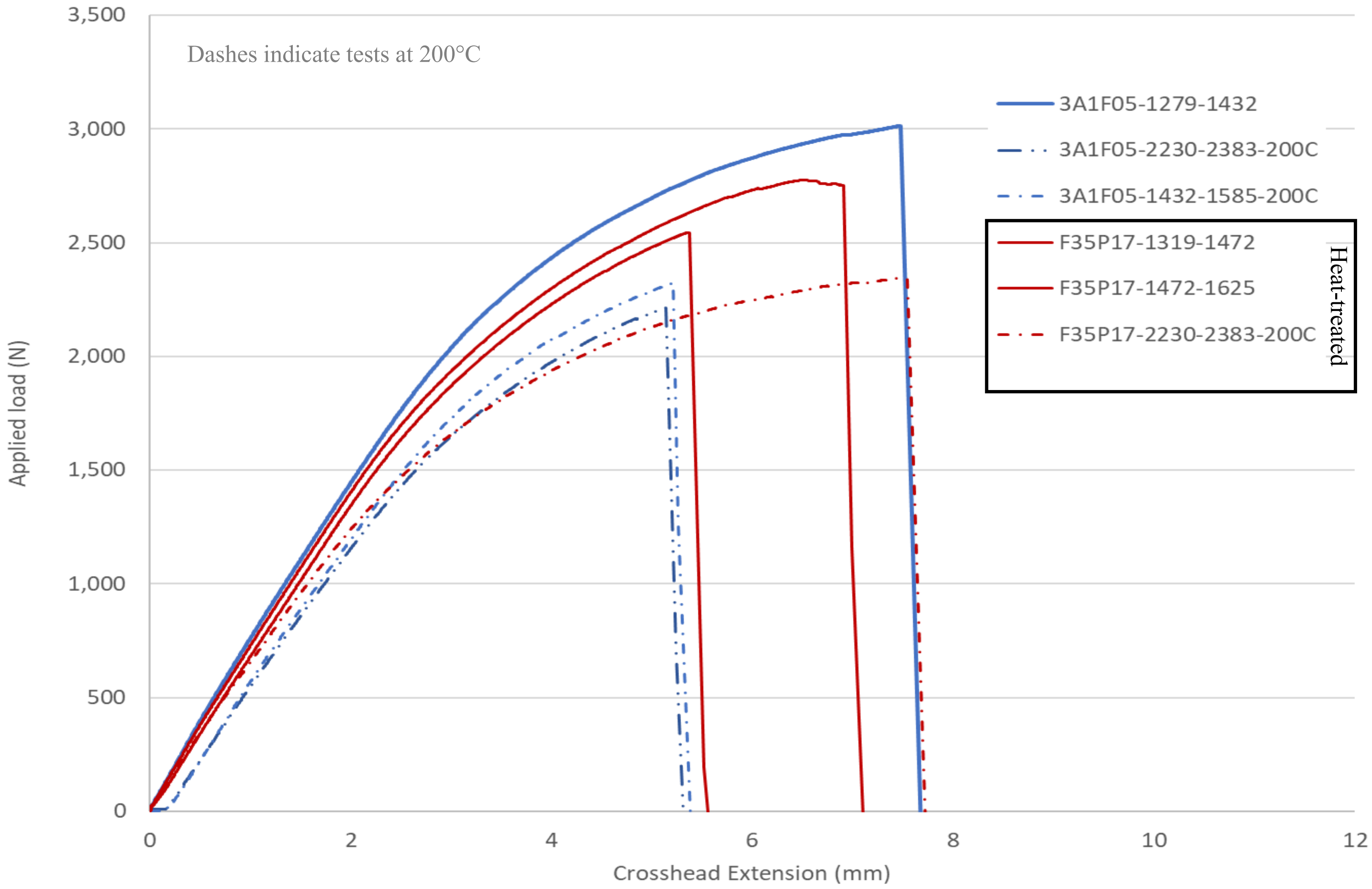

Figure E-6. Zirc-4 and LT Zirc-4 specimens, load vs. crosshead extension.

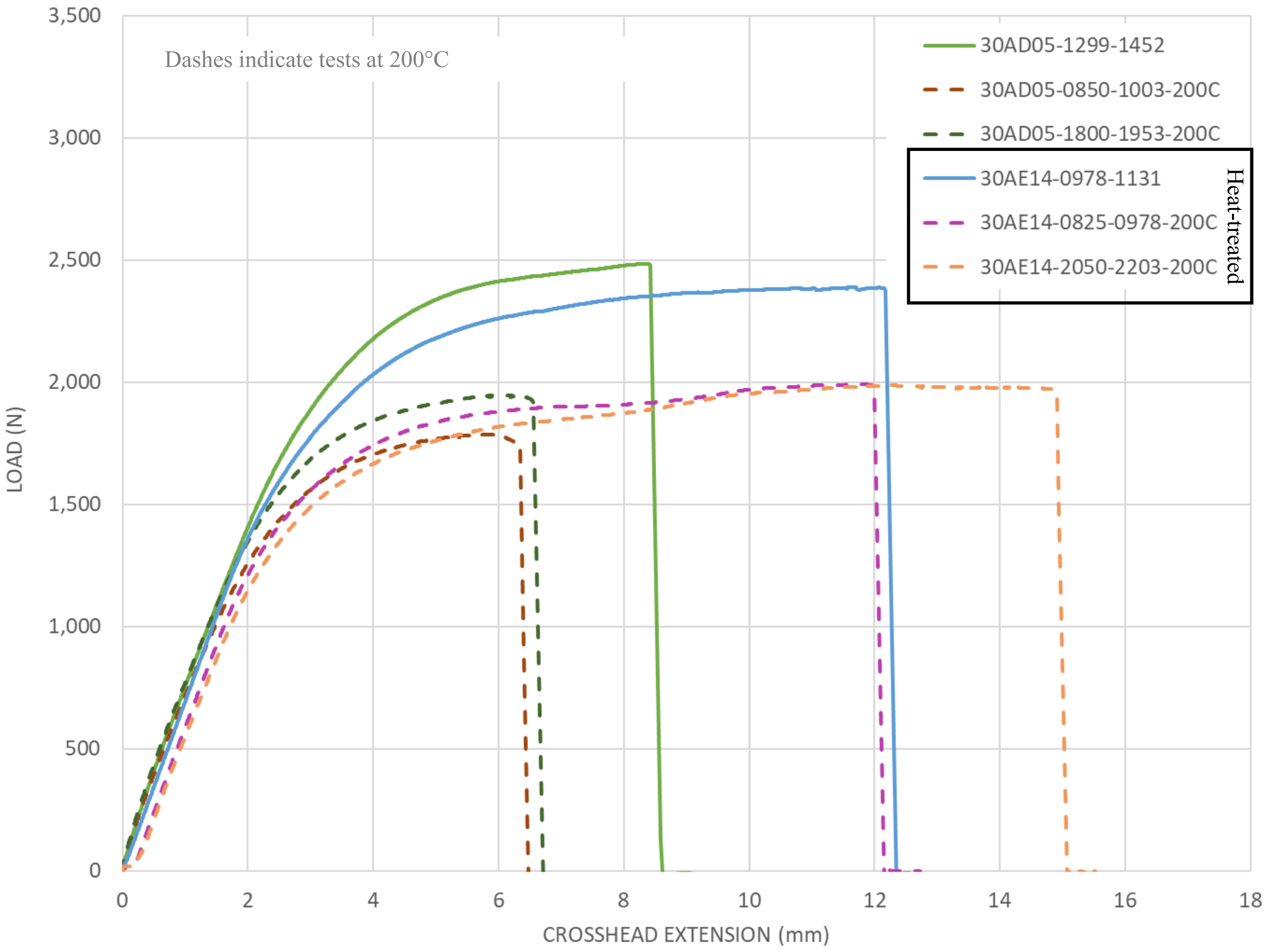

Figure E-7. M5 specimens, load vs. crosshead extension.

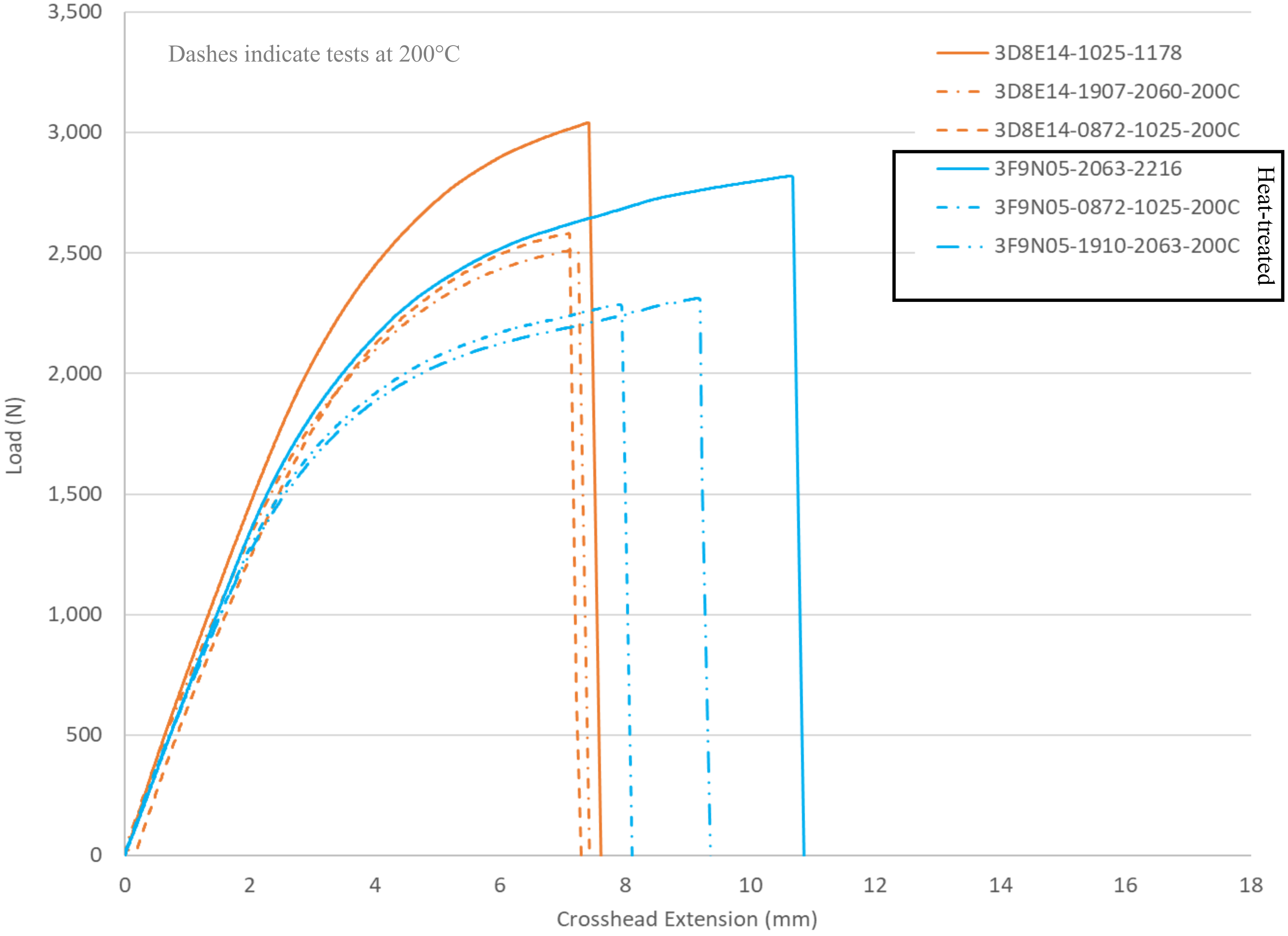

Figure E-8. ZIRLO specimens, load vs. crosshead extension.

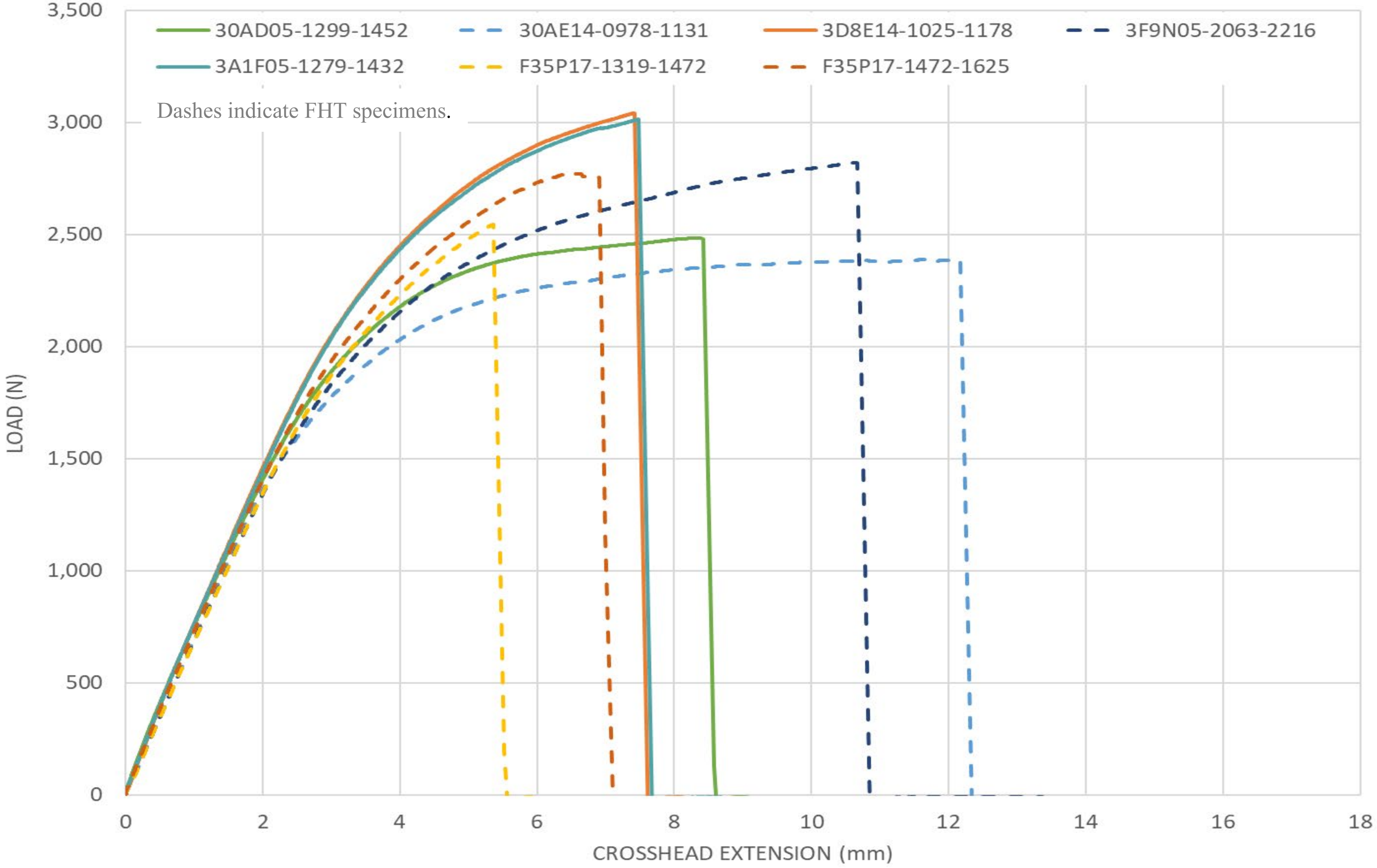

Figure E-9. Load vs. crosshead extension for all RT tests.

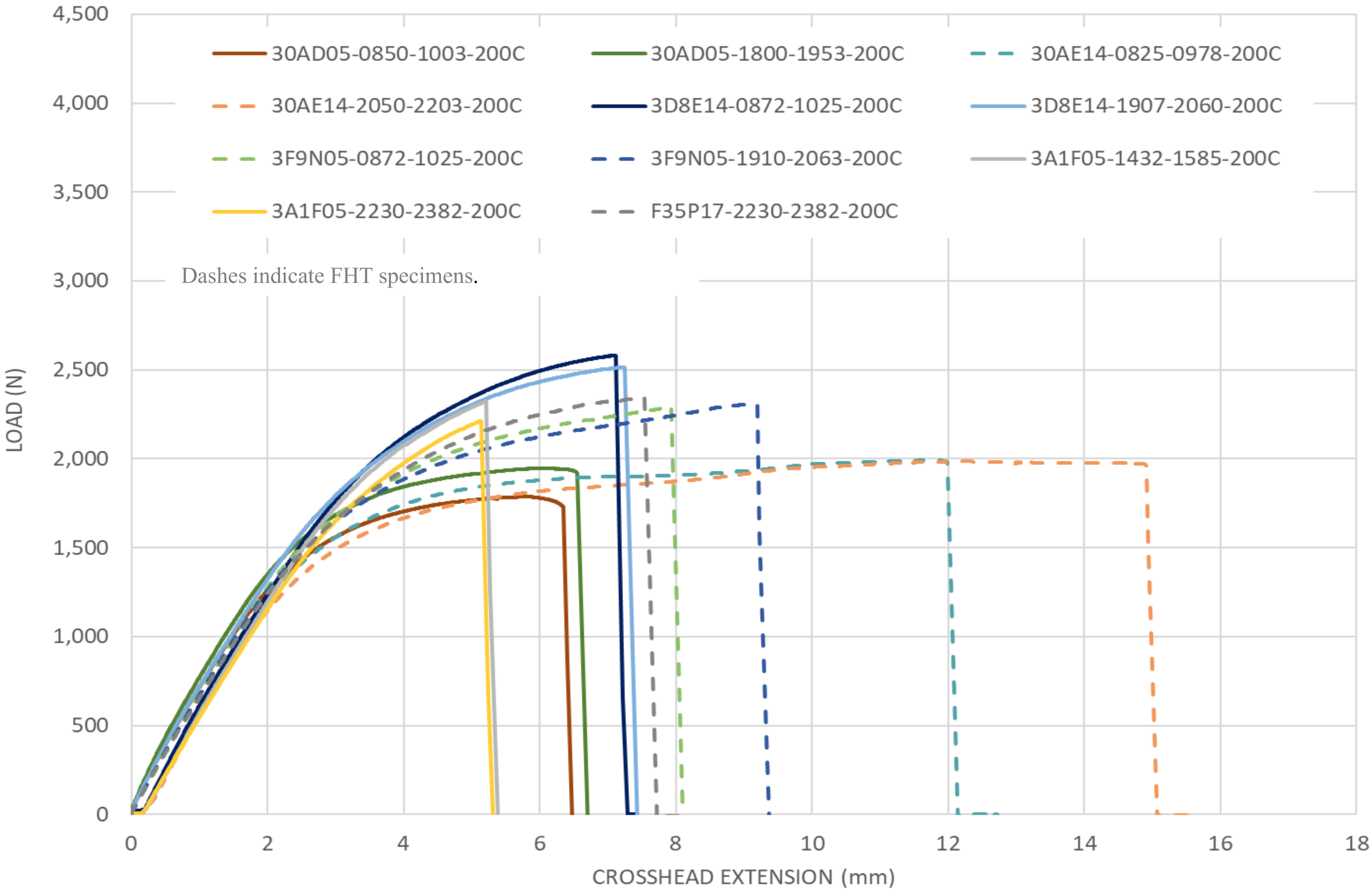

Figure E-10. Load vs. crosshead extension for all 200°C tests.

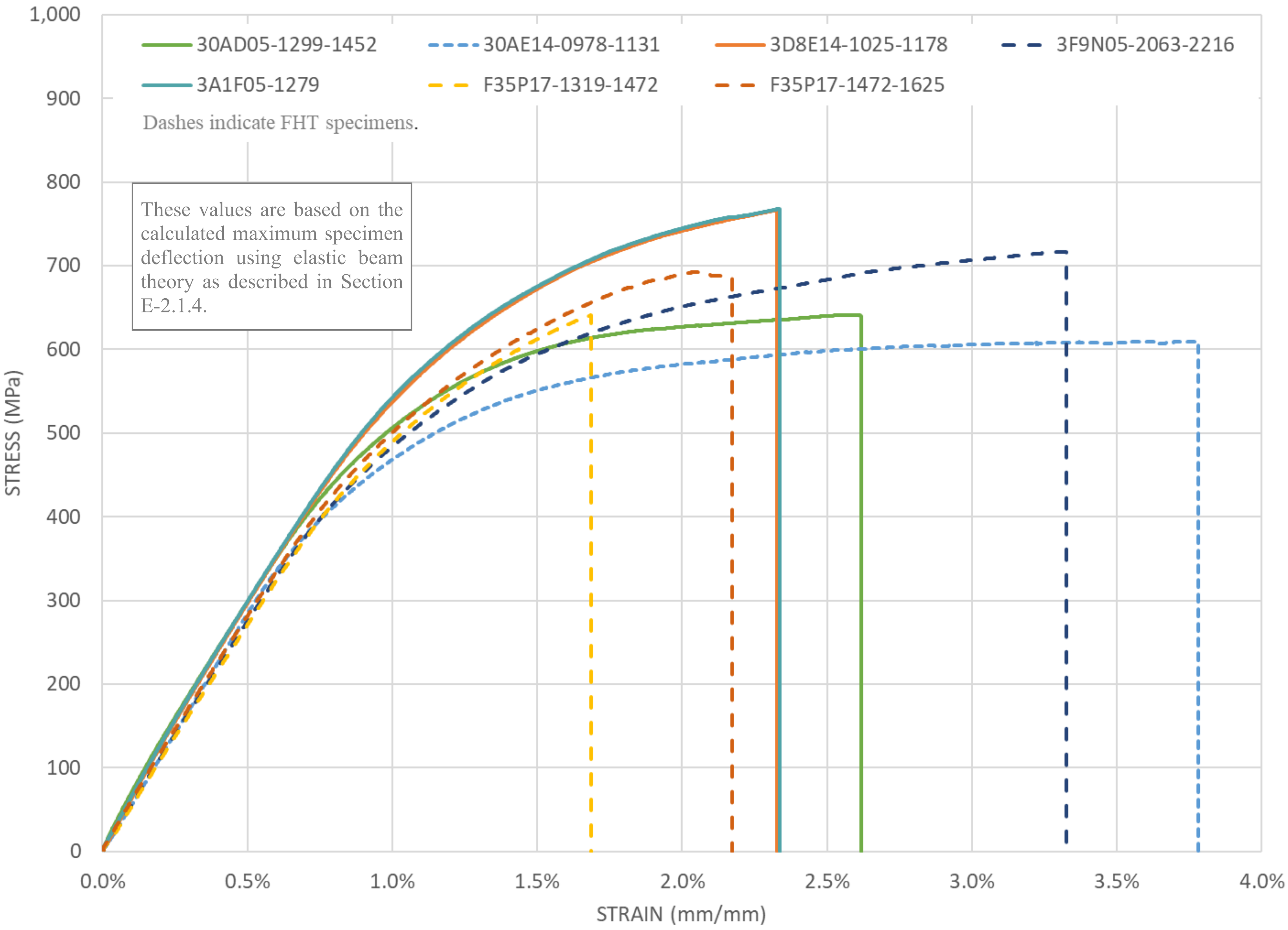

Figure E-11. Stress vs. strain plot for RT data.

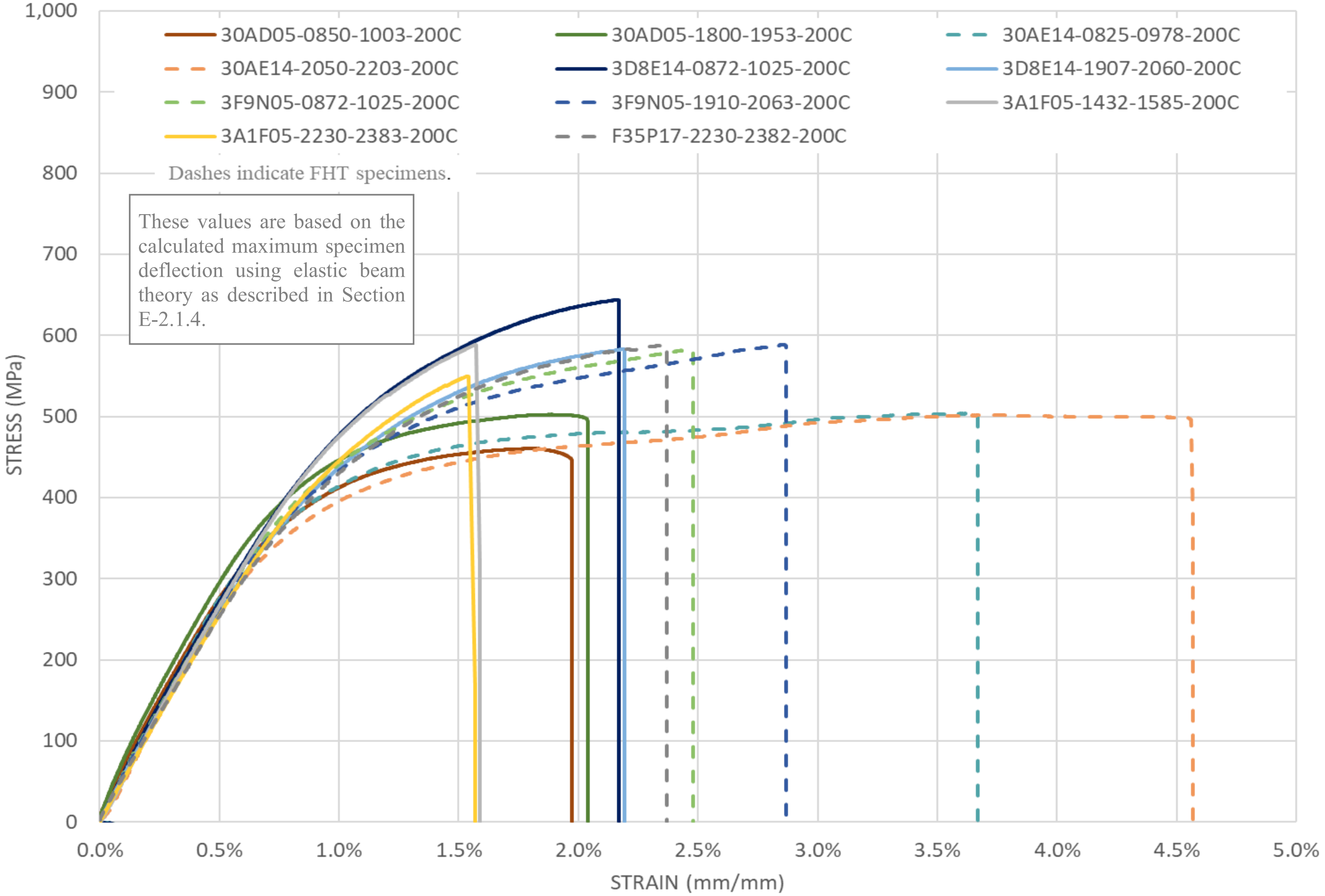

These values are based on the calculated maximum specimen deflection using elastic beam theory as described in Section E-2.1.4.

Figure E-12. Stress vs. strain plot for 200°C data.

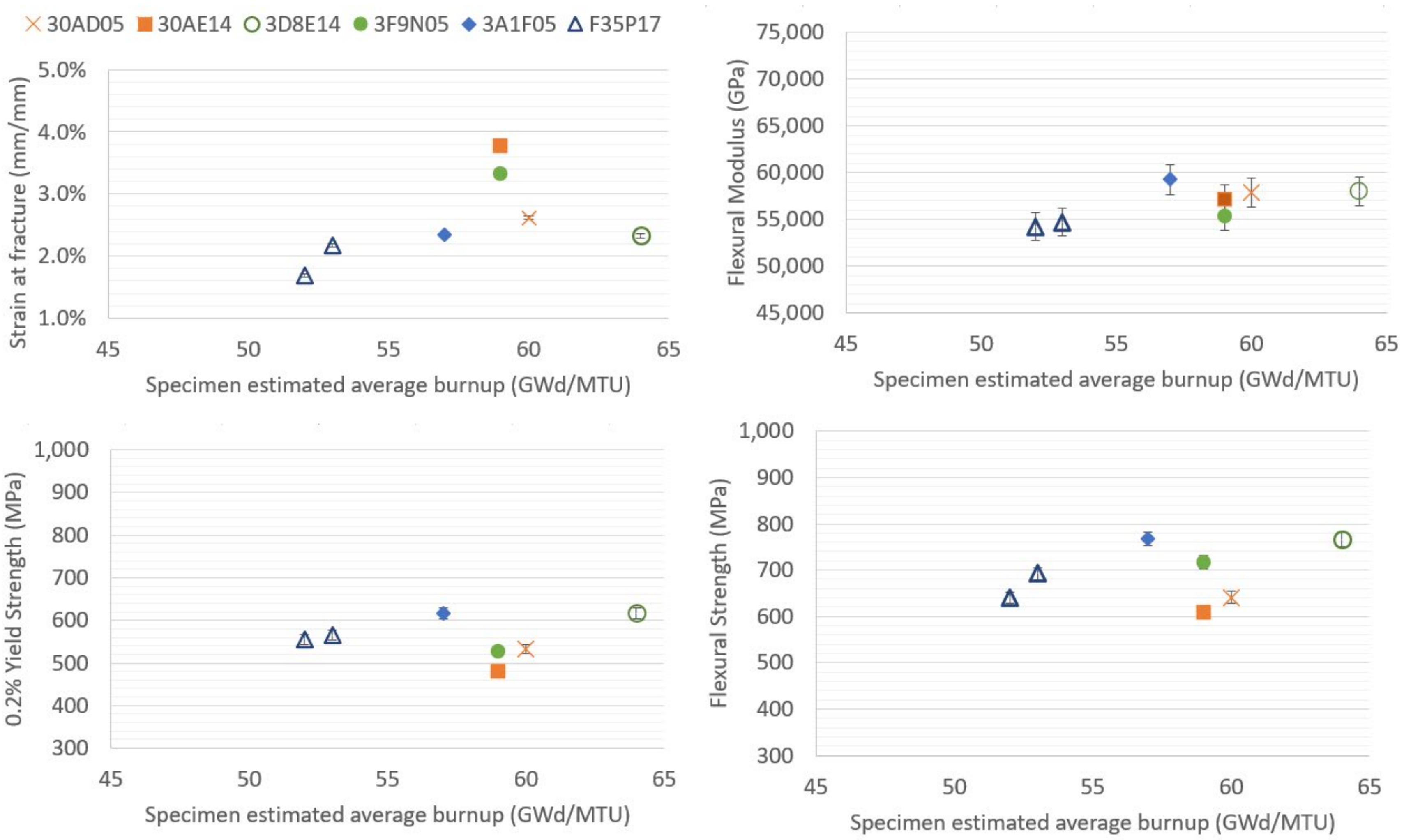

Figure E-13. Calculated RT data plotted as a function of specimen average burnup.

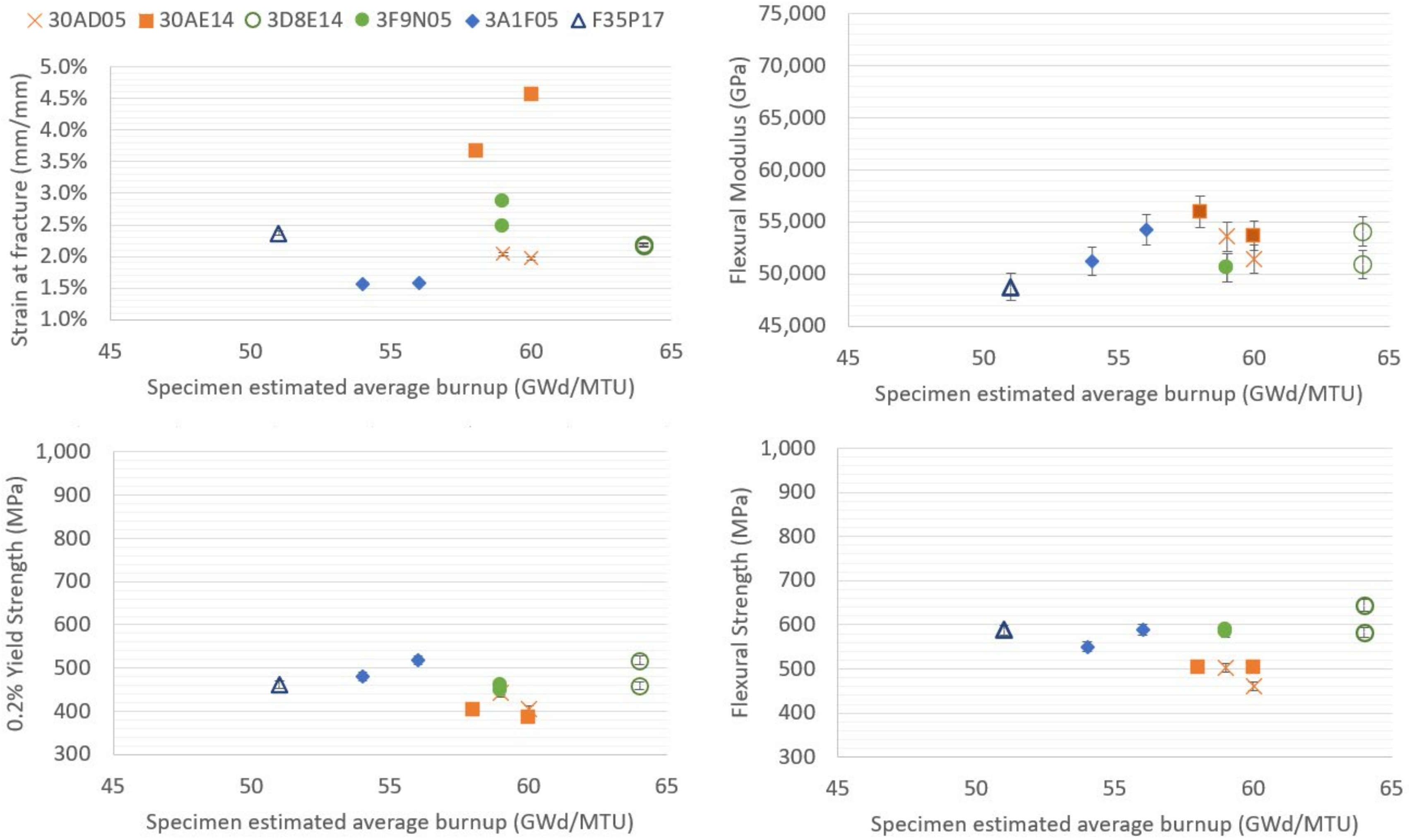

Figure E-14. Calculated 200°C data plotted as a function of specimen average burnup.

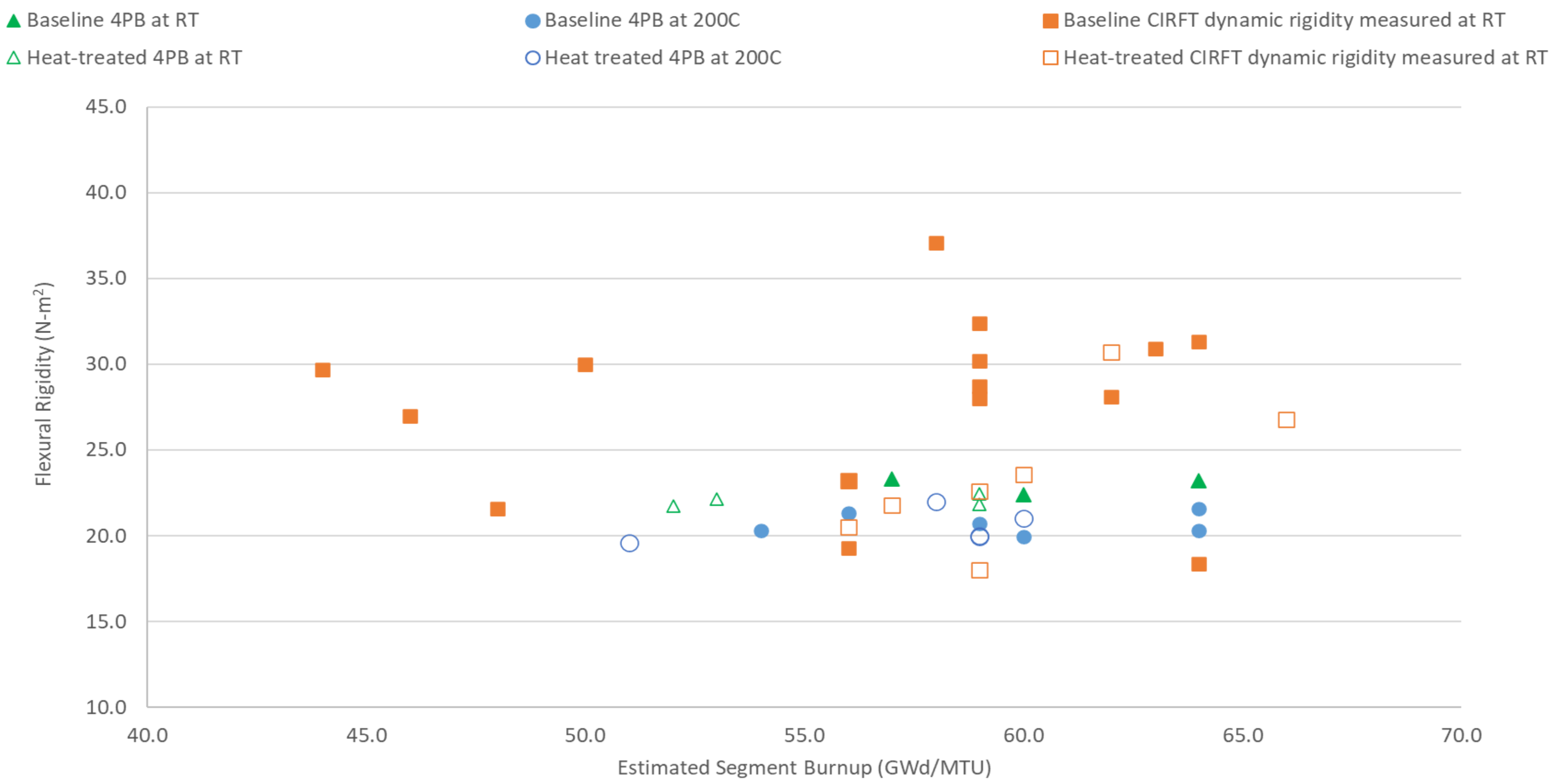

Figure E-15. Comparison of the CIRFT-measured elastic dynamically measured flexural rigidity (as discussed in Appendix F) and the 4PB-measured elastic rigidity.

E-2.4 Finite element modeling of 4PB test results

Finite element modeling of the 4PB test was performed using ANSYS Workbench 2022 R1 to allow for better understanding of the test results, the overall performance of the composite rod, and the functionality of the pellet-clad bonding, pellet-pellet interfaces, and pellet cracks in bending. The improved understanding allows for better informed modeling of normal and accident transport conditions and more accurate predictions from transportation models.

The 4PB rod segment model is 152.4 mm long, with 15 pellets in the stack and 9.5 mm OD cladding. To accurately represent the composite rod system, discrete pellets are modeled within the stack, including chamfers and dishes at the pellet-pellet interfaces. A cracked pellet geometry was included by discretizing the pellet into wedge and truncated wedge geometries (see Figure E-16). The "cracks" in the pellets results in 48 independent pellet pieces in the model of each pellet and a total of 720 pellet pieces. The finite element analysis (FEA) model comprises 75,180 elements and 103,197 nodes. The cladding, pellets, and supports were modeled using linear eight-node solid elements having an average mesh size ~1.5 mm.

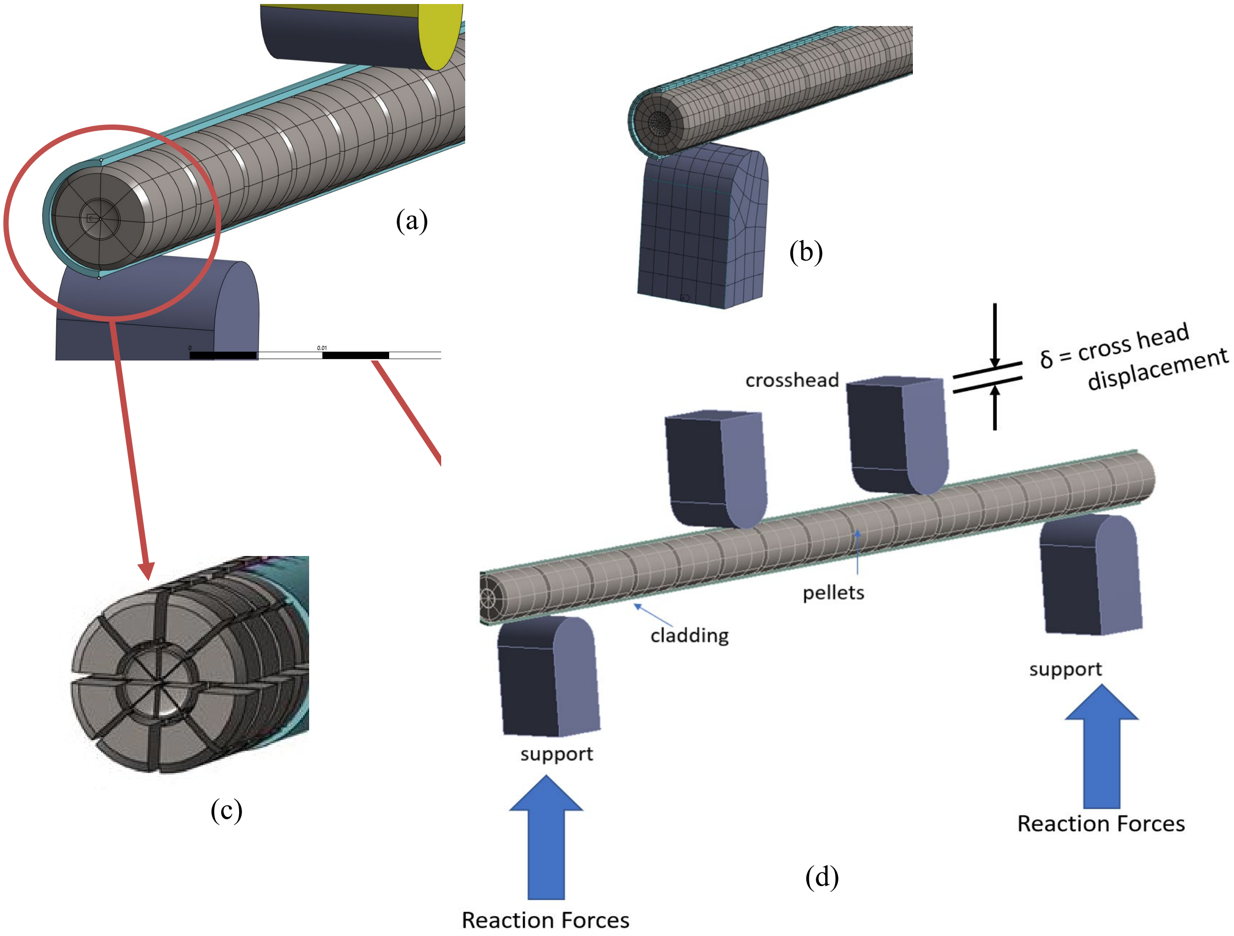

Figure E-16. Four-point bend test finite element model: (a) isometric view with the cladding cut away to show the pellets and the wedge geometry used to create "cracks" for the simulation, (b) mesh used in analysis, (c) exploded view of the pellet showing the pieces modeled, (d) view showing the relative locations of the supports, rod segment, and pellets.

The material properties of both the pellet and the cladding are assumed to be isotropic and at RT. Because the pellet functionality is the target of this study, the cladding properties were not varied and was modeled by using elastic-plastic Zirc-4 material properties (Ref. [E-16.]) The pellets were modeled as ceramic UO_2. The 4PB fixtures are modeled as steel structures having typical steel properties as listed in Table E-3, with the supports spaced at the same distances used in the physical testing (127 mm for the lower supports and 42.4 mm for the upper supports). The linear material properties used for the cladding are provided in Table E-3. The pellet material properties were varied in the simulation as described in the two cases.

Table E-3. Elastic properties used for cladding and supports in the four-point bend model.

	Elastic Modulus (GPa)	Poisson's Ratio
Cladding	91	0.37
Test fixture supports	200	0.30

The pellet-to-pellet and pellet-to-cladding connections used two contact options: (1) bonded/friction and (2) frictional. For the bonded/frictional case, the pellet-to-cladding contact was assigned a bonded connection, and the pellet-to-pellet contact was assigned a frictional contact. For all frictional contacts, a friction coefficient of 0.2 was set for the pellet-to-pellet and pellet-to-cladding contact. A no-separation contact was assigned for the cladding to lower and upper supports. The no-separation contact enabled the cladding to move in plane with respect to the supports and transfer compressive forces between the two components.

E-2.4.1 Case 1: UO_2 Material properties

For Case 1, the pellet was assigned an elastic modulus of 200 GPa and Poisson's Ratio of 0.32 [E-18.] . A displacement input consistent with the physical testing was applied to the upper supports, and they were free to move in the vertical direction but were fixed in the horizontal directions. Through the support and cladding contact specification, the upper supports contact the cladding and cause it to bend. The bottom supports are fixed in all three directions. To prevent rigid body motion of the cladding, a point at the top of the cladding was constrained in the tangential direction, preventing rotation, and the center point of the end pellet was constrained in the axial direction to prevent axial rigid body motion, as shown in Figure E-16. The force required to generate the displacement input was extracted from the output results and compared with the experimental data.

Reaction forces were extracted from the output and are plotted with the crosshead displacement (1 to 6 mm) for comparison with RT experimental data for sample 3A1F05-1279-1432 in Figure E-17. The response of the pellet with the bonded pellet-to-cladding surface contact resulted in a stiffer response than that of the experimental result. The reaction force is 61% greater than the experimental data in the linear range and about 38% greater in the nonlinear range, as shown in Figure E-17. The frictional displacement curve starts off with a 31% overprediction in the linear range and a 15% underprediction in the nonlinear range.

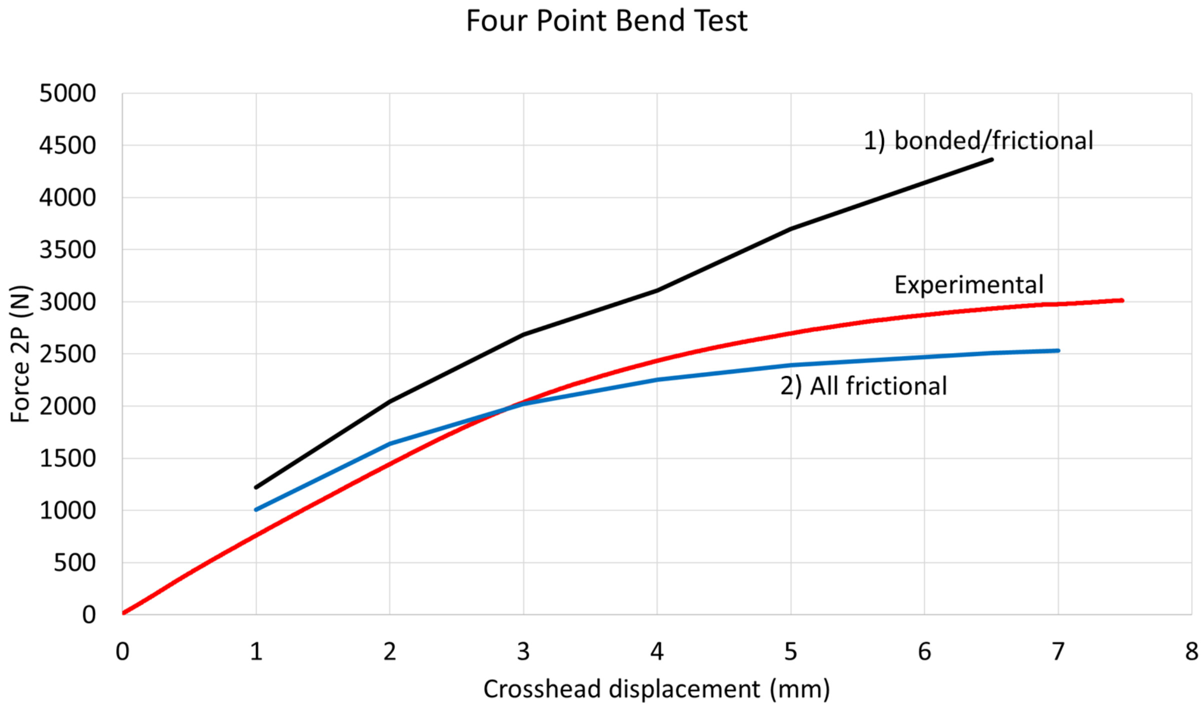

Figure E-17. Predicted force displacement using UO_2 material properties: (1) cladding bonded to the pellet OD with frictional cracks and (2) fully frictional (no clad to pellet bond) compared to RT test results for sample 3A1F05-1279-1432.

E-2.4.2 Case 2: Modified UO_2 Young's Modulus

In an attempt to better fit the model to the data, the Young's modulus of the pellet fragments was calibrated to match the displacement response of the experimental data in the linear range. The cladding material properties were not changed. While using the pellet modulus as a calibration factor is considered non-physical, it suggests potential future model changes needed to better predict the data. Calibration of the pellet's Young's modulus was completed by using one displacement point (e.g., 2 mm) and then modifying Young's Modulus until the force value matched that measured at that displacement in the test. Then all other displacement points were calculated using the model and the modified Young's modulus.

For the bonded pellet-to-cladding/frictional contact surface condition, Young's modulus was reduced from 200 to 70 GPa. With the calibrated Young's modulus for the pellet, the force-displacement response was very near the experimental results at all displacements, as shown in Figure E-18. The calibrated force-displacement curve is within 1% of the experimental in the linear range, and the FEA displacement is within 2% up to 6 mm in the nonlinear range. For the 7.0 and 7.5 mm crosshead displacements, the difference was between 5 and 9%. At these very large displacements (>7.0 mm) it is likely that additional pellet fragmentation and/or debonding at the pellet-cladding interface has occurred resulting a transition to a frictional condition. If the pellet Young's modulus is further calibrated within that range, then an overall Young's modulus of 55 GPa fits the physical test data. It should be noted that, while Young's modulus is used in this study as a means to "soften" the rod, we aren't suggesting that the material properties are lower than expected; rather, it is likely that the softening is related to the ability of the pellet fragments to relocate within the cladding.

Also, in this particular model, when the pellets are bonded to the cladding, a lower modulus is likely needed for the pellet because the model contains pellet-to-pellet surfaces that were artificially created with cracks that are only normal and parallel to the axial direction. In a real cracked pellet, the modulus in tension (as it is on half of the rod in bending) is much lower than fully dense UO_2. However, the modulus in compression depends on the orientation of the pellet cracks. If normal to the axial direction, the modulus in compression would be similar to the fully dense UO_2. As the crack angle deviates from normal, there will be more frictional motion between the pellet pieces, thus decreasing the effective modulus in compression. There are also gaps between the pellets because of dishing that likely contribute to the lower effective modulus in compression.

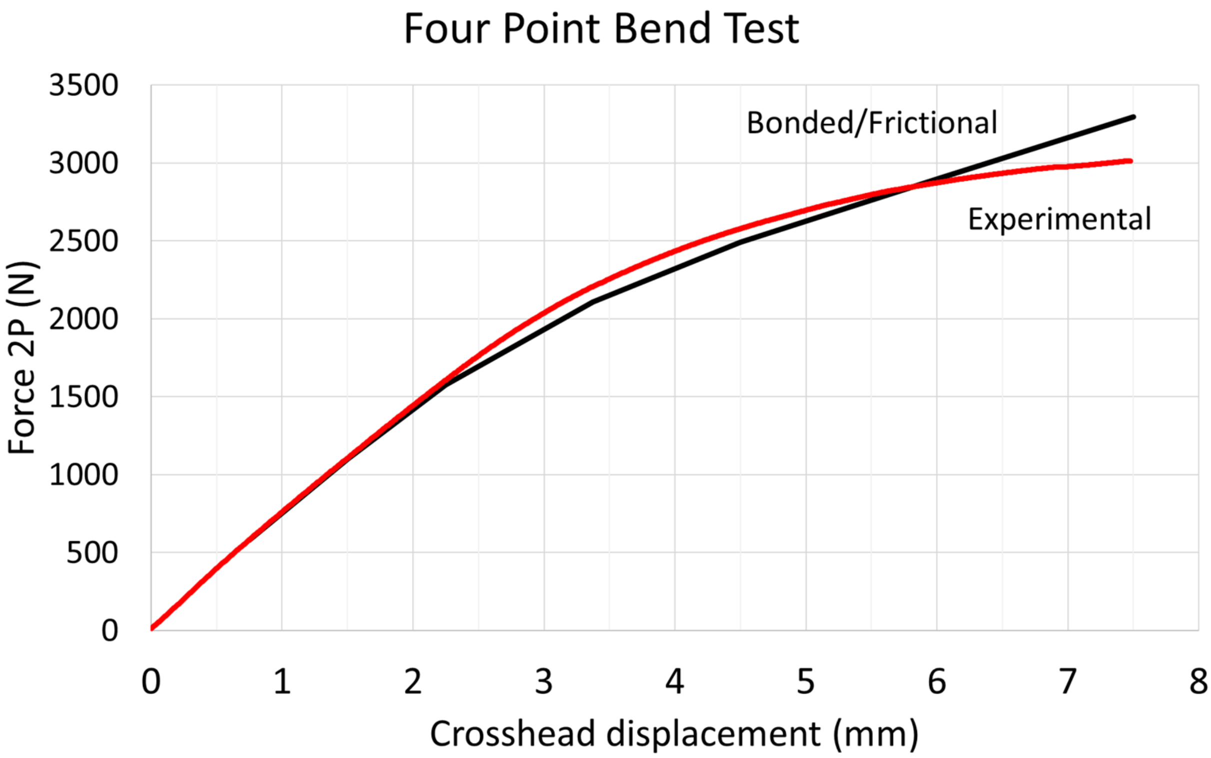

Figure E-18. Predicted force displacement with calibrated pellet Young's modulus and bond contact compared to RT test results for sample 3A1F05-1279-1432.

For the case in which the pellet is not bonded to the cladding inner diameter (ID) and only frictional forces are applied, the calibrated Young's modulus of the pellets was reduced from 200 to 130 GPa to match the test-reported force at 2 mm of displacement. The use of the calibrated Young's modulus to calculate force and displacement resulted in a difference of less than 5% in the linear range, but in the nonlinear range, the calibrated Young's modulus underpredicted the experimental reaction force by an average of 15–20% (Figure E-19). In a real cracked pellet, as the fragments move across each other, they not only have to overcome frictional forces, but they also have to shear overlapping peaks and valleys to move.

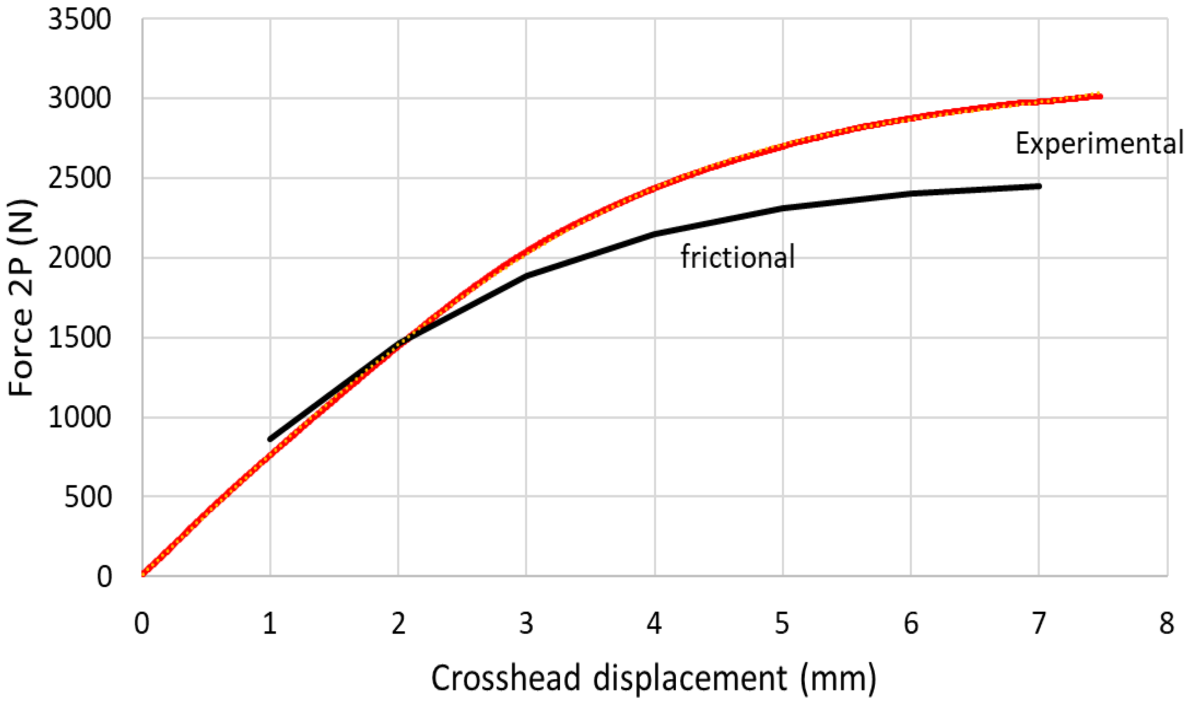

Figure E-19. Predicted force displacement with calibrated pellet Young's modulus and friction contact compared to RT test results for sample 3A1F05-1279-1432.

For this study, the bonded pellet-to-cladding contact surface with a frictional pellet-to-pellet contact surface condition results in a better fit to the experimental force-displacement curve with a calibrated pellet Young's modulus of 70 GPa. One item of note taken from this study is that there are too many pellet fragments modeled. Further simulations are recommended using a pellet crack system taken from a real rod to help to capture more of the sliding / frictional processes in bending. While using the pellet modulus as a calibration factor is considered non-physical, it suggests potential future model changes needed to better predict the data.

E-2.5 Typical Fracture Observed

All segments were fractured near the center of the segment and in the gauge section. Many segments did not fracture completely through the rod section, as shown in Figure E-20(a). Although detailed imaging has not yet been completed, many segments appeared to fracture at pellet-pellet interfaces, as shown in Figure E-20(b). Other specimens fractured through the complete section with tearing of the cladding, as shown in Figure E-21(a) and Figure E-21(b), and the fracture also occurred in the body of the pellet. Images of the fractured specimens are provided in Appendix E2.

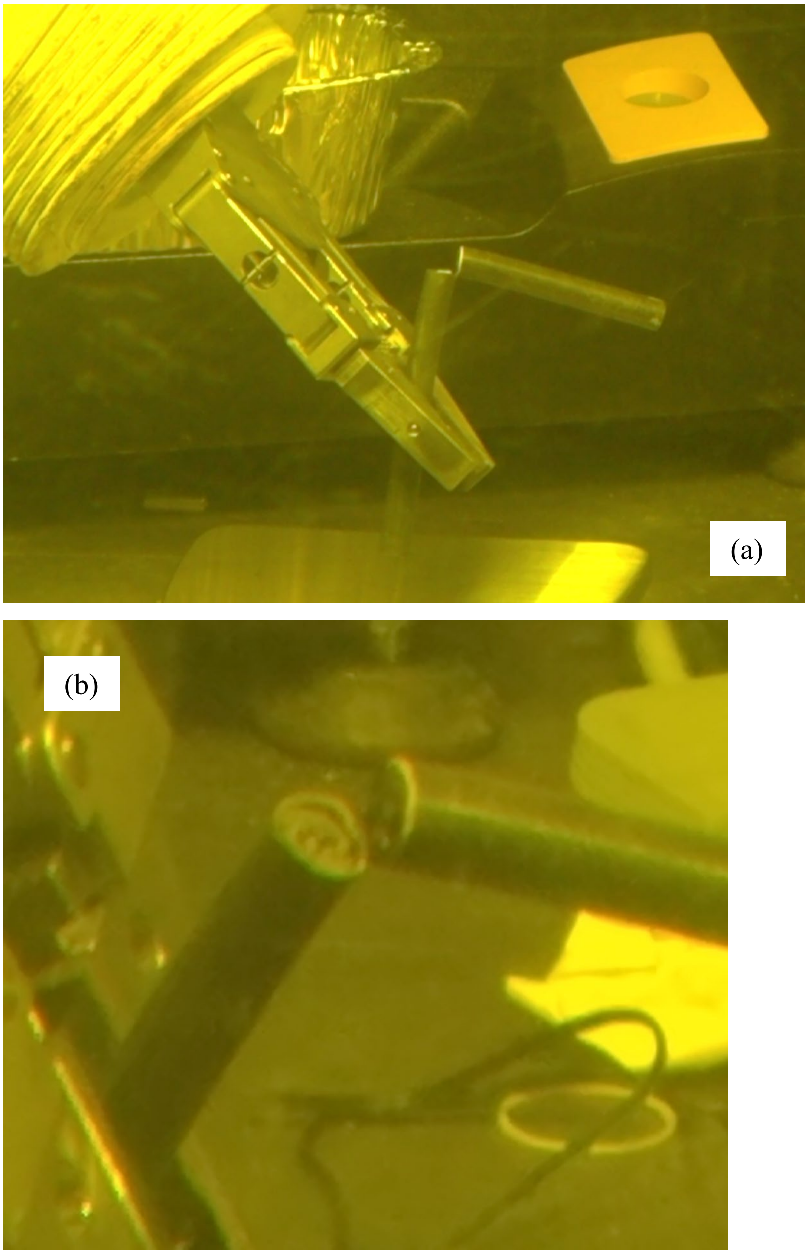

Figure E-20. (a) Many specimens did not completely fracture and (b) fractured at pellet-pellet interfaces.

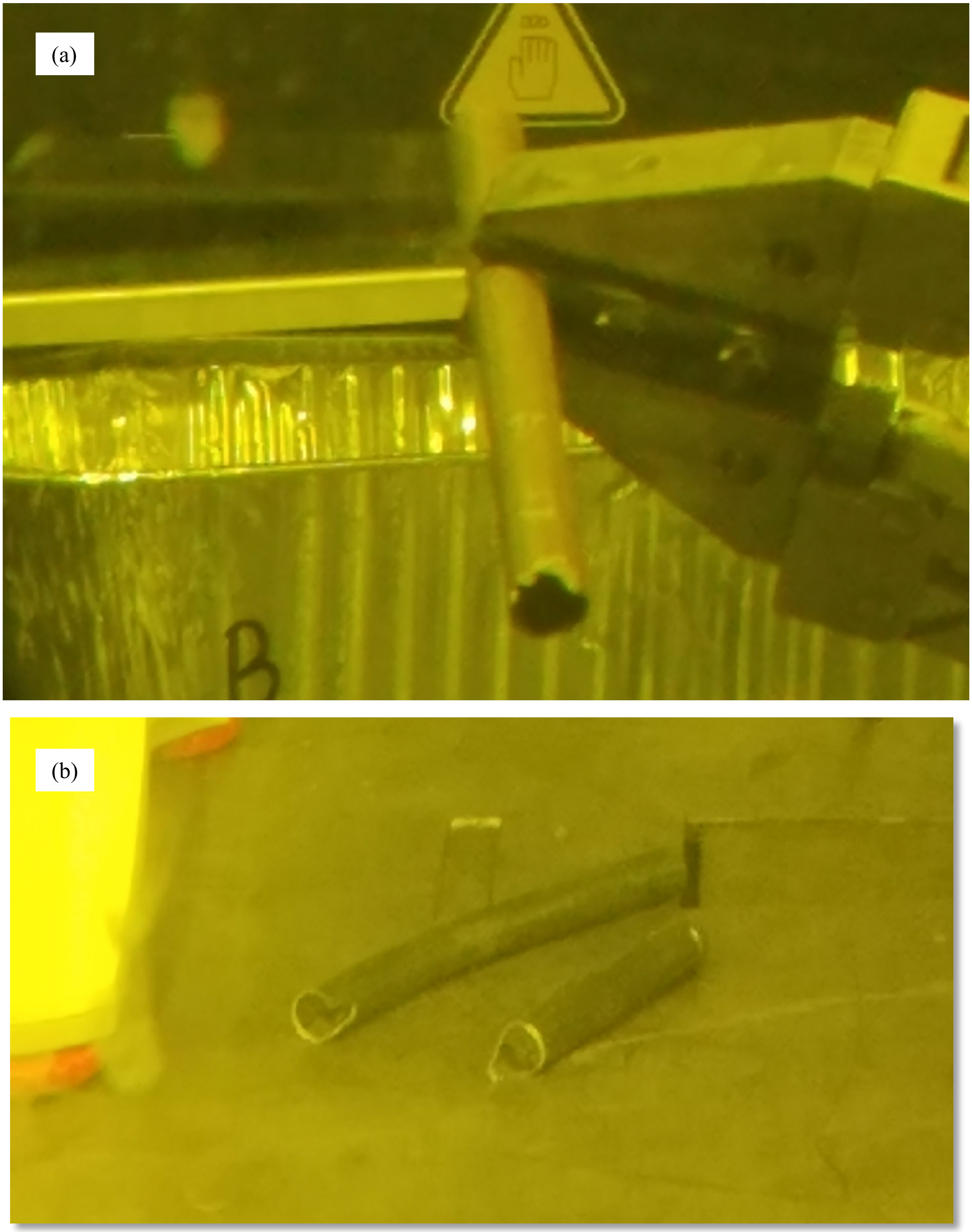

Figure E-21. (a) An example of through-section fracture with secondary tearing, and (b) fracture that occurred in the body of the pellet.

E-2.6 Fuel Release During Fracture

The amount of fuel released during fracture was determined by weighing each specimen before and after the test and weighing the debris collected. Figure E-22 provides a histogram of the mass loss for all specimens tested in 4PB. The largest difference from pre-test to post-test weight was 1.7 ± 0.1 g for F35P17-1472-1625 (RT test). Based on Figure E-23, there is no trend of mass loss with burnup, but there is a tendency for the RT tests to have more mass loss, likely because the cladding fracture is more energetic than the 200°C fracture. From the nondestructive examination (NDE) [E-7] results, each pellet is 9.9–13.7 mm long on average[a] for the sister rods, and each pellet weighs approximately 5.1–7.0 g, assuming a density of 10.1 g/cc. Therefore, the maximum mass lost represents about ¼ of a pellet, whereas the more typical 0.4 g mass loss is less than ⅒ of a full pellet.

The catch tray placed below each specimen during testing collected most of the debris. As shown in Figure E-24(a) and (b), when fracture occurred at pellet-pellet ends, the debris consisted of small particles. A more rigorous method of capturing and quantifying dust-type debris has been implemented and is described in Appendix I.

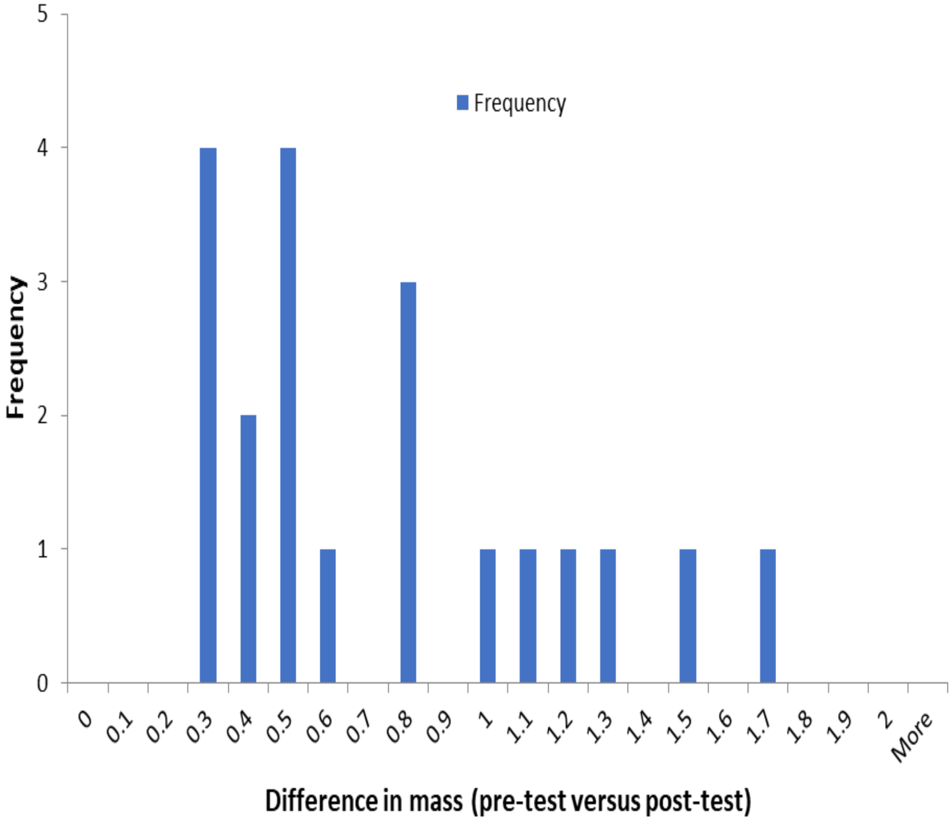

Figure E-22. Histogram of mass loss resulting from 4PB test.

---

[a] ZIRLO-, M5-, and LT Zirc-4-clad rods have measured pellet lengths from 9.8 to 10.3 mm, and the Zirc-4 clad rods have measured pellet length from 13.6 to 13.7 mm.

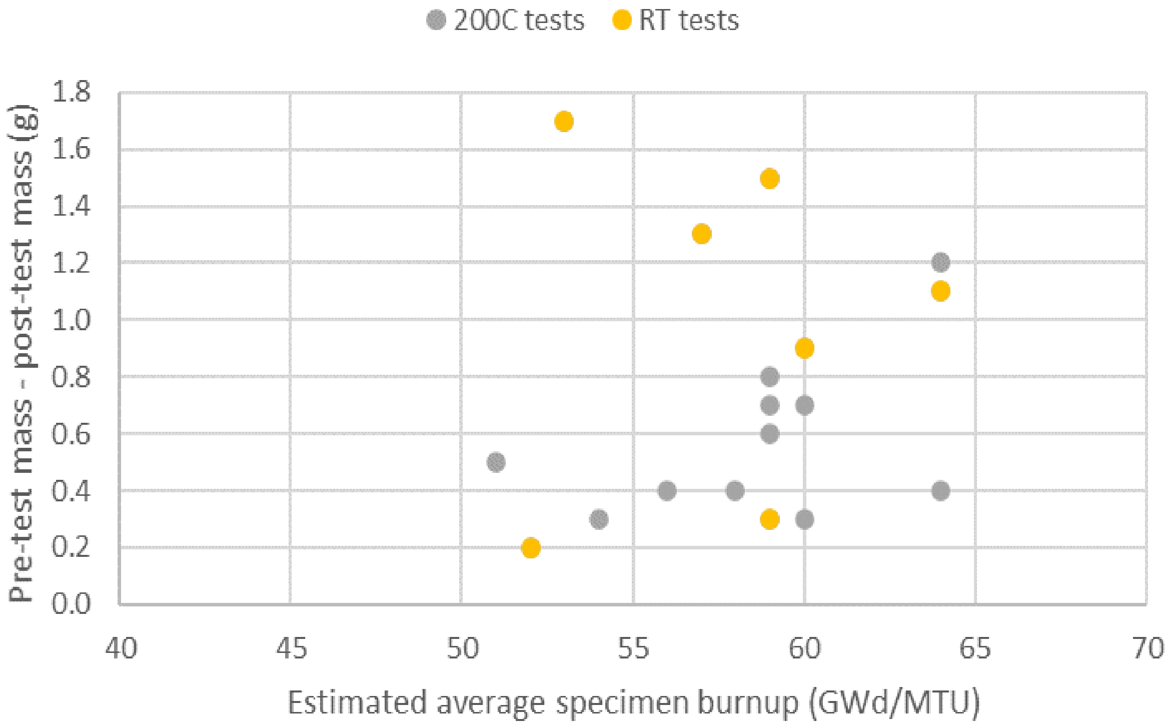

Figure E-23. Measured specimen mass differential (pre-test and post-test) as a function of estimated average specimen burnup.

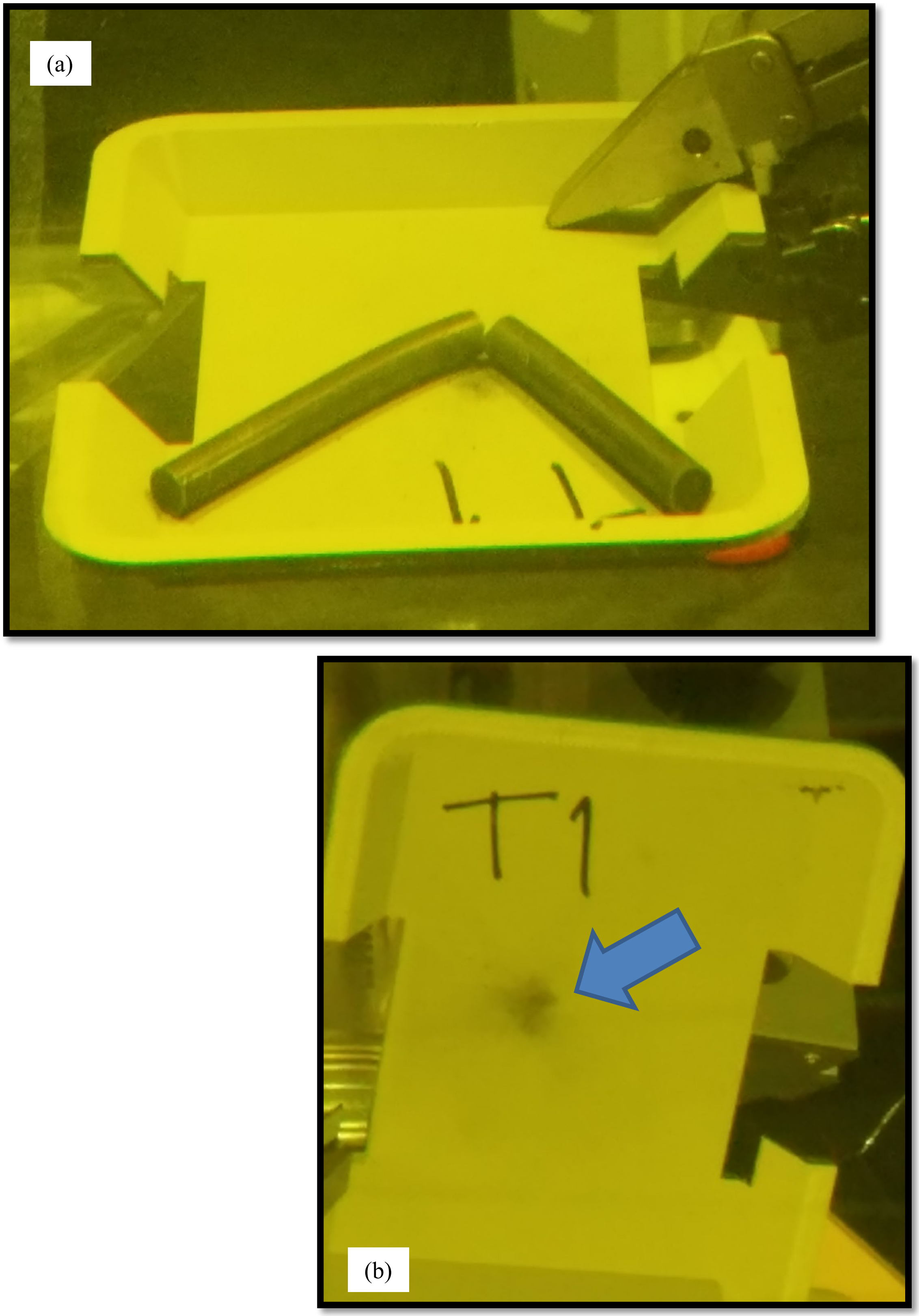

Figure E-24. (a) Post-test debris was captured by a catch tray located below the specimen with (b) the typical RT debris field composed of small particles.

E-3. Axial Tension Testing

To perform axial tension testing (DE.08), a small amount of fuel must be dissolved from each end of the specimen so that a grip can be inserted. The grip is used to prevent the specimen from being crushed at the load point. Therefore, although the rough-cut segments are available, they must be further processed to prepare them for the test. Table E-4 lists the specimens to be tested.

Table E-4. List of specimens for axial tension testing.

Specimen ID#			Test temperature	Specimen heat treatment before test	Operation zone	Estimated local average burnup, GWd/MTU	Specimen average oxide thickness (µm)	Specimen alloy
30AE14	1574	1677	RT	FHT	zone1	60	6	M5
30AD05	1452	1555	RT	None	zone1	60	4	M5
30AE14	2300	2403	RT	FHT	zone1	60	12	M5
30AD05	2802	2905	RT	None	zone1	57	10	M5
F35P17	808	911	RT	FHT	zone1	53	17	Zirc-4
3A1F05	1604	1707	RT	None	zone1	57	42	LT Zirc-4
F35P17	2754	2857	RT	FHT	grid5	49	133	Zirc-4
3A1F05	2754	2857	RT	None	grid5	53	133	LT Zirc-4
3F9N05	1444	1547	RT	FHT	zone1	59	12	ZIRLO
3D8E14	1553	1656	RT	None	zone1	64	18	ZIRLO
3D8E14	2674	2777	RT	None	zone1	63	44	ZIRLO
3F9N05	3138	3241	RT	FHT	zone1	56	48	ZIRLO
30AE14	1471	1574	200°C	FHT	zone1	59	5	M5
30AD05	1555	1658	200°C	None	zone1	59	6	M5
30AE14	2403	2506	200°C	FHT	zone1	60	13	M5
30AD05	3349	3452	200°C	None	zone1	49	17	M5
F35P17	930	1033	200°C	FHT	zone1	53	20	Zirc-4
3A1F05	1750	1853	200°C	None	zone1	56	42	LT Zirc-4
F35P17	2857	2960	200°C	FHT	zone1	51	138	Zirc-4
3A1F05	2857	2960	200°C	None	zone1	54	138	LT Zirc-4
3D8E14	1450	1553	200°C	None	zone1	64	16	ZIRLO
3F9N05	1547	1650	200°C	FHT	zone1	59	13	ZIRLO
3D8E14	1804	1907	200°C	None	zone1	64	19	ZIRLO
3F9N05	3035	3138	200°C	FHT	zone1	57	48	ZIRLO

In FY21, Pacific Northwest National Laboratory (PNNL) reported a sensitivity of the cladding-only axial tension specimens associated with clamping the specimen into the load frame, as well as the clamp-on extensometer. PNNL also reported slipping of the specimen within the axial tension grips related to the specimen's OD oxide layer. ORNL has essentially an identical setup for axial tension tests. To determine if the sensitivity was also associated with fueled specimens, ORNL tested a specimen available from a previous program (M5 clad pressurized water reactor [PWR] rod). Four trials were performed, and the specimen broke each time at the clamp on the upper axial tension jaws. Based on these results, an alternative method to clamp the specimens in the load frame is being investigated.

In FY23, ORNL developed an alternative grip assembly as shown in Figure E-25. The clamp assembly consists of a mounting fixture fabricated out of low carbon steel, a collet, and a chuck nut. Two assemblies— upper and lower—mount in the load frame. The ends of the fuel rod are inserted into the collet and secured by tightening the chuck nut. The grips will be tested with unpressurized SNF rod segments when the new load frame is installed, because the MiniMight is not expected to be capable of handling the loads required to fracture a rod in axial tension.

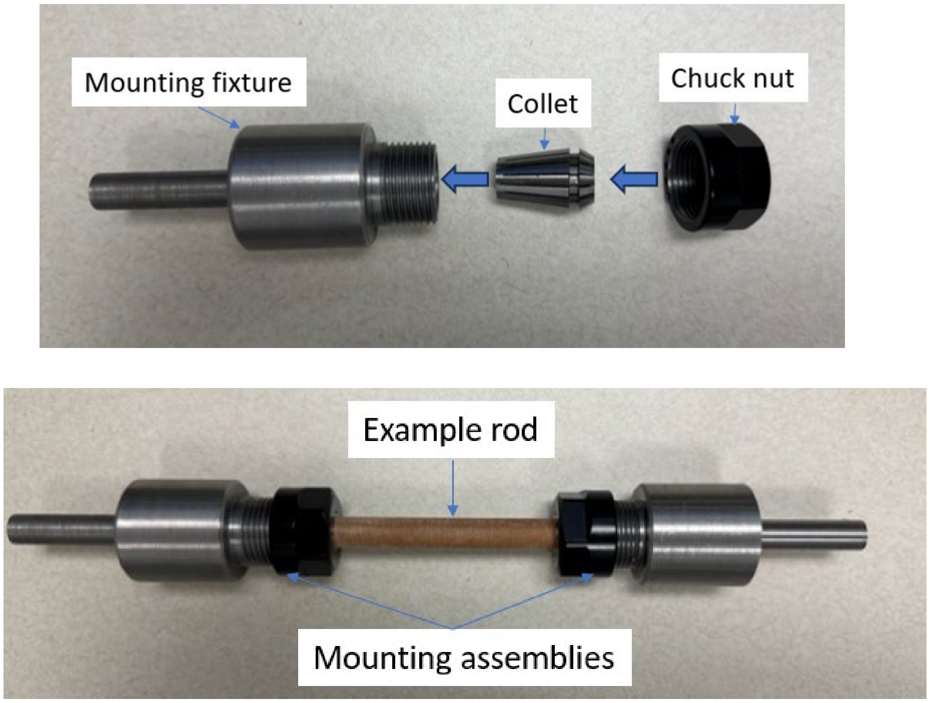

Figure E-25. Developed axial tension grip.

E-4. Microhardness Tests

Microhardness test (DE.09) equipment is available at both the Low Activation Materials Development and Analysis (LAMDA) laboratory and the Irradiated Fuels Examination Laboratory (IFEL) at ORNL. The equipment at IFEL will be used for both RT and 200°C testing when it is available. The equipment at LAMDA has been used to perform tests at RT only. Table E-5 lists the specimens to be tested and status.

Table E-5. Specimens Selected for Microhardness Tests.

Rod	Originating segment elevation range (mm)		Cladding type	Estimated local average burnup, GWd/MTU	Selection criteria	Status
30AD05	3240	3259	M5	55	Highest oxide	Completed on defueled cladding at RT
30AD05	2410	2429	M5	59	HBU region with higher oxide	Work in progress
30AD05	1280	1299	M5	59	Oxide thickness and hydride distribution	Sample cut completed
30AE14	2675	2694	M5 (FHT)	61	HBU at oxide peak	Completed on defueled cladding at RT
30AE14	3399	3418	M5 (FHT)	50	Highest oxide thickness	Completed on defueled cladding at RT
3A1F05	2735	2754	LT Zirc-4	54	High oxide thickness at HBU	Completed on defueled cladding at RT
3A1F05	3105	3124	LT Zirc-4	53	Peak oxide thickness	Sample cut completed
3A1F05	2383	2402	LT Zirc-4	55	HBU with higher oxide thickness, spalling oxide, pellet banding	Work in progress
3A1F05	1260	1279	LT Zirc-4	56	Oxide thickness and hydride distribution	Work in progress
3A1F05	2006	2025	LT Zirc-4	56	Oxide thickness and hydride distribution	Sample cut completed
3D8E14	2655	2674	ZIRLO	63	HBU with oxide spike	Completed on defueled cladding at RT
3D8E14	3206	3225	ZIRLO	59	Highest oxide thickness	Completed on defueled cladding at RT
3D8E14	2303	2322	ZIRLO	62	Oxide thickness and hydride distribution	Work in progress
3D8E14	700	719	ZIRLO	62	Oxide thickness and hydride distribution	Sample cut completed
3F9N05	2863	2882	ZIRLO (FHT)	58	HBU with higher oxide	Completed on defueled cladding at RT
3F9N05	3331	3350	ZIRLO (FHT)	51	Peak oxide thickness, spalling oxide, pellet banding	Completed on defueled cladding at RT
3F9N05	700	719	ZIRLO (FHT)	56	Oxide thickness and hydride distribution	Sample cut completed
3F9N05	1425	1444	ZIRLO (FHT)	59	Oxide thickness and hydride distribution	Sample cut completed
3F9N05	2300	2329	ZIRLO (FHT)	57	Oxide thickness and hydride distribution	Work in progress
6U3K09	3506	3525	ZIRLO	42	CIRFT correlating data	Sample cut completed
F35P17	2735	2754	Zirc-4 (FHT)	66	Oxide thickness, spalling oxide, pellet banding	Completed on defueled cladding at RT
F35P17	3050	3069	Zirc-4 (FHT)	65	Peak oxide thickness, spalling oxide, pellet banding	Sample cut completed
F35P17	2383	2402	Zirc-4 (FHT)	66	Oxide thickness, spalling oxide, pellet banding	Sample cut completed

E-4.1 Test Protocol, Equipment Verification, Data Processing Approach, and Measurement Uncertainty

Tests at LAMDA were performed at RT using the Buehler Wilson VH3100 Microhardness (Figure E-26) tester. The tester has both Vickers and Knoop indentation capability with a maximum load capacity of 10 kg. All tests in this report were completed using a Vickers indenter.

Figure E-26. LAMDA laboratory's Buehler Wilson VH3100 Microhardness Tester.

Prior to microhardness examination of the sample, the equipment was tested using a Sun-Tec certified[b] calibrated sample having a known Vickers hardness (HV) value. The surface of the calibrated sample was cleaned using isopropanol alcohol to remove any residue on the surface. Then, six indents were applied using forces of 0.1, 0.3 and 0.5 kg*f* (six indents in total), and were held for ~10 and 15 s, respectively. Figure E-27 shows a series of Vickers indent shapes on the sample surface that were produced by the indenter tip as captured using a ×40 lens. As seen in Figure E-27, a valid indent shape is uniform such that the indent edges are straight and the diagonal lengths (shown as d_1 and d_2 in the figure) are almost identical, indicating a uniform pressure distribution under the indenter.

The Vickers hardness indent has a form of a pyramid shape with a square base that has an angle of α=136 degrees. The HV number is calculated as

$$HV = \frac{F}{A} = \frac{2Fsin\left(\frac{136^o}{2}\right)}{d^2} \sim \frac{1.8544F}{d^2}, \tag{E-9}$$

---

[b] The calibration standard was manufactured in accordance with ASTM E92-17 and ISO/IEC 17025 on 05/10/21.

Where *F* is in kilogram-force (kg*f*), *A* is the area of the indention, and *d* is the average length of the diagonals (i.e., $d=(d_1+d_2)/2$) left by the indenter in millimeters.

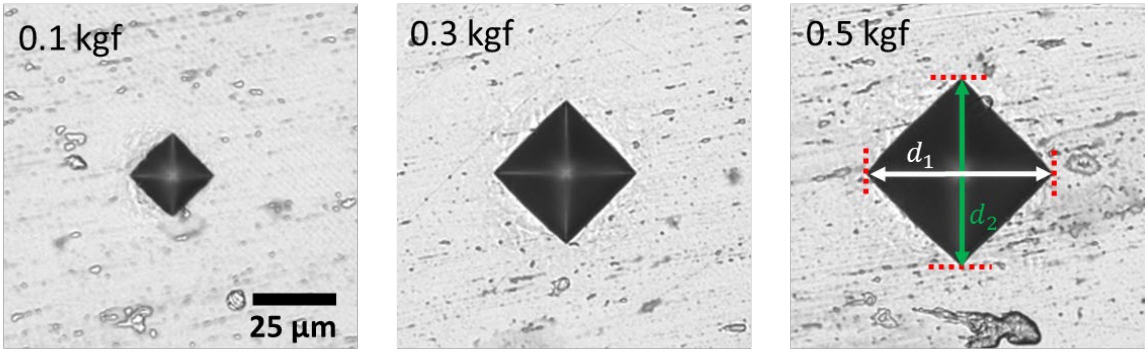

Figure E-27. The shape of indents left on the calibrated sample surface after applying 0.1, 0.3 and 0.5 kg force using ×40 lens. The scratches on the sample surface likely resulted from surface polishing. The lengths of the diagonals left by the indenter were measured as d_1 and d_2 and were averaged.

The main source of error in the HV number (ΔHV) in Eq. (E-9) is the error associated with measuring the diagonal lengths (Δ*d*). For a given load force, the relationship between Δ*d* and ΔHV can be determined through the error propagation, where $\frac{\Delta HV}{HV}$ can be expressed using the partial derivative of Eq. (E-9):

$$\frac{\Delta(HV)}{HV}=\frac{\partial HV}{\partial d}\frac{\Delta d}{HV}=\frac{-2C}{d^3}\frac{\Delta d}{Cd^{-2}} \quad \text{, and} \tag{E-10}$$

$$\frac{\Delta(HV)}{HV}=-2\frac{\Delta d}{d} \tag{E-11}$$

Therefore, Eq. E-11 indicates a 1% error in diagonal length measurement results in a 2% error in HV. Several factors can contribute to Δd, such as:

1) variations in measurements among different operators who perform the test,
2) variations in objective lenses used for diagonal length measurements, and
3) error attributed to the method itself when creating an indentation.

In the case of the sister rod data, the same person performed all tests to date. When data from the IFEL equipment are available, comparisons between the results obtained with the LAMDA and IFEL equipment will be examined for biases.

A 60× objective lens is used for measurements at LAMDA, and for this lens, the error for each diagonal was taken to be ±4 pixels (i.e., 2 pixels at each corner). Image resolution at this magnification is 576 × 480 pixels, and 1 pixel was calculated to be ~ 0.24 µm.

Prior to conducting microhardness tests, indents were made on a calibration standard and were measured for verification of the LAMDA equipment. Table E-6. summarizes the microhardness test parameters and the corresponding HV numbers (HV_m) determined from Eq. (E-9) for the calibration standard. The measured HV of the calibration standard was consistent with the HV provided by the manufacturer (HV_{ref}) and were within the expected measurement error.

Table E-6. Standard sample hardness measurement results using VH3100 Microhardness tester compared with the reference hardness measurements.

Indent #	Load (kgf)	Hold time (s)	Measured hardness (HV_m)	Certified hardness (HV_{ref})*	% Relative error $\left\|\frac{HV_m - HV_{ref}}{HV_{ref}}\right\|$
1	0.1	10	303 ± 10	301 ± 4.8	2.3
2	0.3	10	301 ± 24		2.0
3	0.5	10	299 ± 14		0.3
4	0.1	15	295 ± 10		2.0
5	0.3	15	294 ± 10		2.3
6	0.5	15	298 ± 13		1.0

* HV_{ref} is given as an average hardness of five different measurements (varying from 295 to 307 HV) conducted at RT using 0.5 kg-force. The estimated uncertainty in the certified hardness was calculated by the provider within 95% confidence level.

For the cladding measurements, microhardness indents will be made in each quadrant using a standardized force and spacing, starting from the cladding's ID and moving radially toward the OD, with each indention held for 10 s. According to the ASTM E92-17, the minimum spacing between each individual indent and between an indentation and the edge of the sample should be 2.5× the indent's diagonal length, as illustrated in Figure E-28, to avoid an inaccurate measurement.

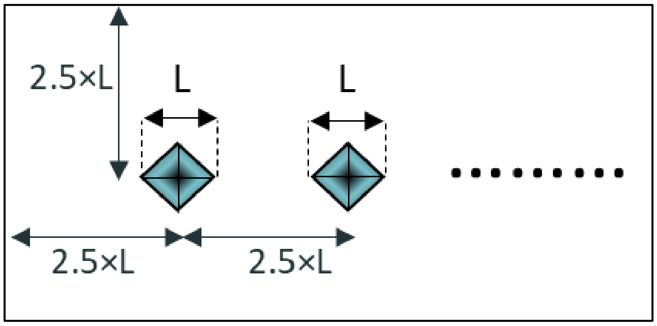

Figure E-28. Illustration of minimum recommended spacing for Vickers indentations and the measured diagonal length, L.

Considering this guideline, the maximum number (N) of indents that can fit within each quadrant of the fuel cladding can be estimated using Eq. (E-12):

$$N = \frac{t_{clad}}{2.5L} - 1, \quad \text{(E-12)}$$

where t_{clad} is the cladding thickness and L is the average diagonal length.

Given the cladding thickness of the sister rod specimens, Eq. (E-12) was used to estimate the number of indents (N) possible. A few individual indents were arbitrarily created on a sister rod sample using different test forces ranging from 0.1 to 1 kgf. The diagonal lengths (L) of the resultant indents were measured; some of these indents are shown in Figure E-29, with the corresponding test forces indicated. The average diagonal length of each indent and the corresponding HV value were calculated and plotted as shown in Figure E-30 with respect to the applied test force. Figure E-30 shows an almost linear relationship between the test force and the average indent size. The corresponding HV initially shows a modest increase from HV 257 ± 9 at 0.1 kgf to HV 263 ± 6 at 0.3 kgf. However, when a test force of 1 kgf was applied, a pronounced reduction in HV was seen. It is possible that the plastic zone created by the indent tip at this test force extended beyond the specimen and started to sample the epoxy mounting media, causing the reduction. Therefore, to reduce the uncertainty in the microhardness measurements and to increase the number of indents that could be applied, a test force of 0.1 kgf was selected for application in these tests.

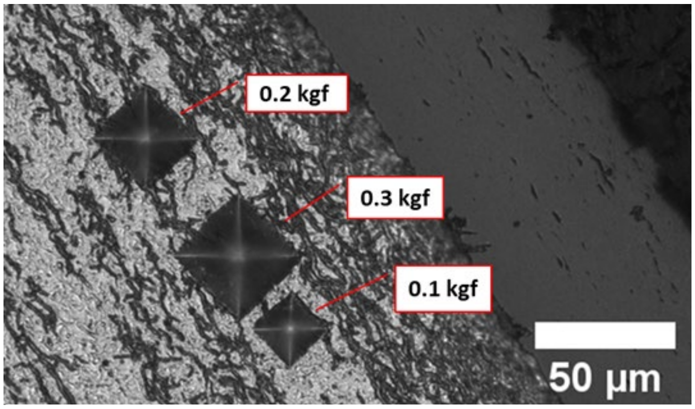

Figure E-29. Micrograph comparing microhardness indents formed using different loads.

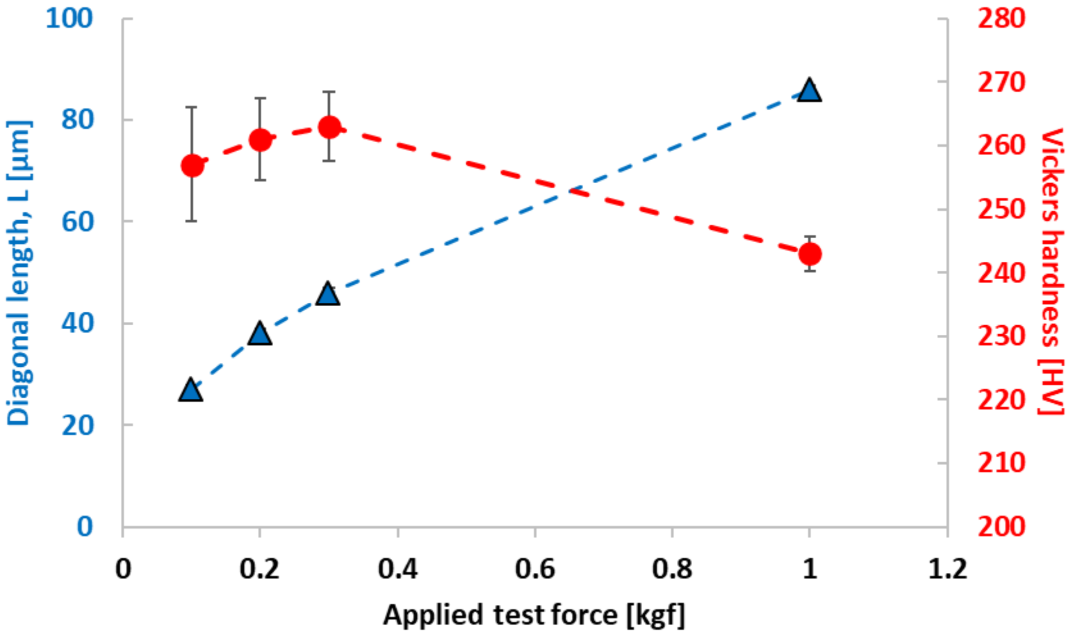

Figure E-30. Measured indent's diagonal length (*L*) and Vickers hardness (*HV*) as a function of applied test force in kilogram-force.

Considering the cladding thickness and the indent size at this test force, 7 indents can be made across the cladding thickness, starting from the cladding ID and moving radially toward OD, with each indention held for 10 s. At the selected test force of 0.1 kgf, the average indent size on the cladding specimens typically ranged between ~25–30 µm, which also satisfies the minimum indent size recommended by ASTM E384-17 for accurate measurement (>20 µm). As a final test, an additional series of microhardness indents was created on *30AE14-2675-2694* using both 0.1 kgf and 0.3 kgf test forces as shown in Figure E-31. The application of 0.3 kgf test force resulted in an average indent size of ~45 µm, which is almost twice the size of the average indent resulting from the 0.1 kgf test force. Despite the pronounced difference in the indent size, Figure E-31 shows that the measured HV values obtained are consistent.

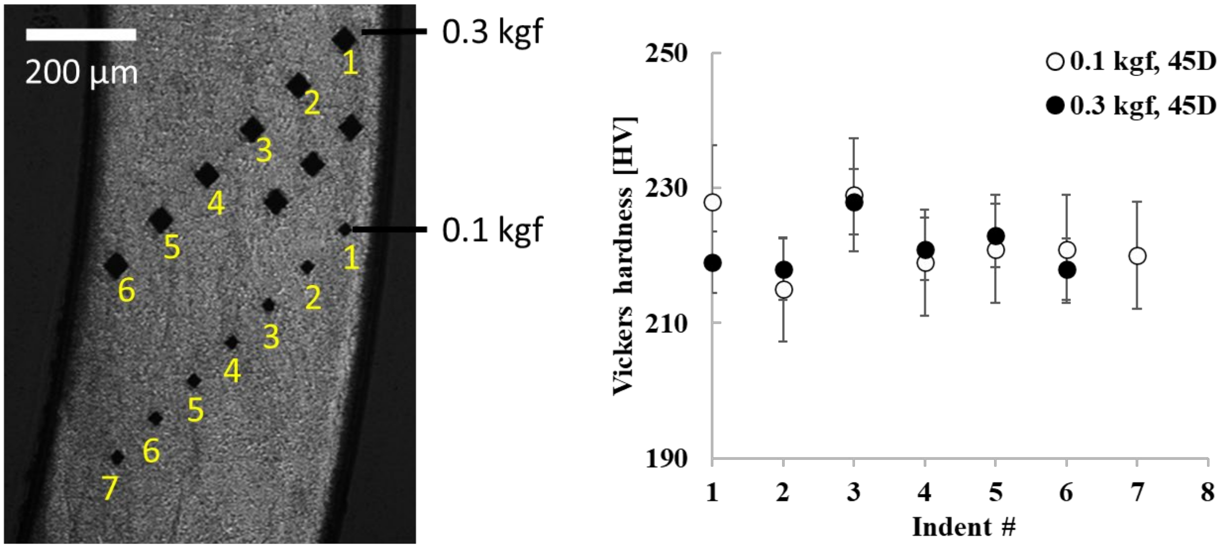

Figure E-31 Optical microscope image showing the microhardness indentation prints applied with 45 degrees (45D) on the right quarter of the sample 30AE14-2675-2694 using 0.1 kgf and 0.3 kgf test forces (left); plot comparing corresponding Vickers hardness (right).

Per applicable ASTM standards, if the indents produced in the test are less than 20 µm, then the testing is classified as light force testing. However, the considerations for light force testing are mainly applied for Knoop-type hardness testing, because of the pyramidal diagonal inherent in the geometry of the Knoop indenter tip. ASTM strongly recommends avoiding light load forces for Knoop indention. For Vickers hardness testing, the indent geometry is constant with load, and increasing/decreasing the indention load only changes the size of the indent—not its geometry. Visibility of the smaller indention is generally the only concern related to load selection for Vickers hardness testing. For these tests, both the indent size and the selected load are higher than the ASTM-recommended thresholds for Vickers hardness testing and are considered acceptable.

E-4.2 Vickers Hardness Data

Microhardness tests were performed at the LAMDA facility [E-7] on nine defueled cladding samples: three M5 (1 baseline and 2 heat-treated), four ZIRLO (2 baseline and 2 heat-treated), one LT Zirc4 and one heat-treated Zirc4. Although these samples were lightly etched to reveal the hydrides, their surfaces were found to be smooth enough under optical microscope to allow for microhardness testing. Visual inspection of the microhardness indents shows crisp uniform indent edges, the diagonal lengths are equal, and the diagonal corners can be easily distinguished from the background. Also, the hydrided areas were not so dark as to prevent indent size measurements. Therefore, it was concluded that surfaces of the lightly etched specimens were adequate for microhardness tests. A comparison of the HV data for the lightly etched sample with data reported for this Sister Rods by PNNL using mechanically polished samples [E-17] are also consistent.

Considering the cladding wall thickness and the indent size at 0.1 kgf, 7 indents were typically made in each quadrant, for a total of 28 indents per specimen. The indents were made starting from the cladding ID and moving radially toward OD, and each indention was held for 10 seconds. One exception was for 3F9N05-3331-3350 (FHT ZIRLO cladding sample). The cladding specimen was set in its mount at an angle, and the grinding and polishing process completely removed a portion of the specimen (see Figure E-36). For this specimen, indentations were only made in the regions where the sample would be sufficient for measurement. Another exception was F35P17-2735-2754, in which an additional 7 indents were made (i.e. 35 indents in total) in a region where spalled oxide was observed. Table E-7 summarizes the microhardness examination data.

Table E-7 Summary of microhardness

Fuel Rod ID	Axial Span [mm]	Cladding Alloy	Estimated local burnup* [GWd/MTU]	Radial position [µm]	Vickers hardness** [HV ± ΔHV]	$\overline{HV}$ $\pm std.\ dev$
30AD05	3,240–3,259	M5	55	51	230 ± 8	235 ± 3
				126	234 ± 8	
				201	233 ± 8	
				276	237 ± 8	
				351	237 ± 8	
				426	239 ± 8	
				501	238 ± 8	
30AE14	3,399–3,418	FHT M5	50	55	223 ± 7	224 ± 5
				130	215 ± 7	
				205	228 ± 8	
				280	226 ± 7	
				355	224 ± 7	
				430	227 ± 8	
				505	223 ± 7	
30AE14	2,675–2,694	FHT M5	61	88	221 ± 8	224 ± 3
				152	220 ± 8	
				221	226 ± 8	
				286	221 ± 8	
				352	227 ± 8	
				420	227 ± 8	
				490	224 ± 8	
3D8E14	3,206–3,225	ZIRLO	59	49	249 ± 9	262 ± 9
				124	256 ± 9	
				199	262 ± 9	
				274	259 ± 9	
				349	264 ± 10	
				424	268 ± 10	
				499	277 ± 9	

Table E-7. Summary of Microhardness (continued)

Fuel Rod ID	Axial Span [mm]	Cladding Alloy	Estimated local burnup [GWd/tU]	Radial position * [μm]	Vickers hardness** [HV ± ΔHV]	$\overline{HV}$ $\pm std.\ dev$
3D8E14	2,655–2,674	ZIRLO	64	43	261 ± 9	268 ± 9
				118	262 ± 9	
				193	263 ± 9	
				268	264 ± 9	
				343	275 ± 10	
				418	273 ± 10	
				43	261 ± 9	
3F9N05	3,331–3,350	FHT ZIRLO	51	56	245 ± 8	253 ± 5
				131	255 ± 9	
				206	248 ± 9	
				281	251 ± 9	
				356	257 ± 9	
				431	257 ± 9	
				506	257 ± 9	
3F9N05	2,863-2,882	FHT ZIRLO	58	53	260 ± 9	264 ± 4
				128	262 ± 9	
				203	261 ± 9	
				278	262 ± 9	
				353	266 ± 9	
				428	265 ± 9	
				503	270 ± 10	
3A1F05	2,735–2,754	LT Zirc4	54	67	257 ± 9	264 ± 16
				137	258 ± 9	
				206	257 ± 9	
				276	252 ± 9	
				349	256 ± 9	
				413	264 ± 9	
				477	300 ± 11	
F35P17	2,735–2,754	FHT Zirc4	66	32	265 ± 11	270 ± 11
				107	259 ± 10	
				182	263 ± 10	
				257	270 ± 10	
				332	267 ± 9	
				407	276 ± 9	
				482	290 ± 9	

* The first indent is selected by the user and the following indents are indexed by the machine. The radial position is the average of the four quadrants, measured to the center of the indent.

**The average of the measured hardness and measurement uncertainty from each of the four quadrants.

An overview of cladding optical microscopy images and the locations of the microhardness indents are presented in Figure E-32 through Figure E-39**,** along with a plot of each datapoint and the average hardness as a function of radial location. The cladding wall and oxide thicknesses measured from these micrographs are also provided in these figures, and they are consistent with previous nondestructive examinations (NDEs) reported by Montgomery et al. [E-7] and metallography (MET) measurements reported in Appendix B. For better visibility, Figure E-41 shows a series of higher magnification images of selected cladding samples with the microhardness indentation prints on a single quadrant as reference.

The corresponding average HV values are tabulated in Table E-7 and plotted in Figure E-42 to allow for comparison of the hardness as a function of cladding alloy type. The small variations in the quadrant dataset are within the measurement uncertainty; the scattering is likely caused by the variations in local hydride morphologies.

Figure E-42 shows some noticeable variations in the Vickers hardness data according to the alloy type. The M5 samples had the lowest hardness among all the cladding alloys tested, whereas the average hardness of the ZIRLO and the Zirc-4 samples were similar and higher than that measured for M5. The alloy-to-alloy differences in hardness can be attributed to variations in the initial metallurgical states of the claddings. The M5 claddings are recrystallized-annealed (RXA) whereas ZIRLO/Zirc-4 claddings are cold-worked and stress-relief annealed (CWSRA) [E-9].

To investigate whether the observed alloy-to-alloy hardness difference is caused by the difference of the corresponding local burnup, the hardness data were plotted with respect to the estimated local burnup as shown in Figure E-43. Figure E-43a indicates that the M5, which only has 3 datapoints, is not well correlated with burnup; however, Figure E-43b shows an increasing trend for the measured hardness for ZIRLO and Zirc-4 samples with respect to local burnup. The data shows an increase of ~7 % in cladding hardness for the CWSRA Zircaloy claddings with the increase in burnup from ~51 to 66 GWd/MTU.

Figure E-42 shows that the data sets indicate some variations in the hardness profiles across the cladding wall thickness according to alloy type. For example, the M5 specimen hardness profiles were uniform across the cladding wall, whereas the ZIRLO specimens had an increasing trend toward the waterside hydride rim. In the case of the FHT ZIRLO cladding, there was a modest increase in the hardness of ~10 HV. The radial increase in hardness was the most pronounced in the baseline LT Zirc-4 cladding near the cladding OD and in the FHT Zirc-4 at the outer ~200 µm from the cladding OD. An OD hydride rim is visible on the microhardness specimens (~65–90 µm for Zirc-4 and ~35–50 µm for ZIRLO). It seems likely that, for these examples, that the high density of hydride precipitates increased the hardness locally as compared with measurements of the base alloy.

However, PNNL reported an increased OD hardness, even where an OD cladding hydride rim was not present (typically lower rod elevations) [E-17]. Differences in the operation of the fuel rod in reactor are also expected to influence measured hardness. The increase in the number and the length of the operational cycles in-reactor increases the total neutron fluence on cladding and consequently the as-discharged cladding hardness [E-13, E-14]. Note that within this document, local burnup is used as a surrogate for burnup, since the fluence is not available. The assembly core location affects both neutron fluence and temperature. The assemblies irradiated near the core center experience higher neutron flux and higher irradiation temperature, whereas assemblies at the core periphery are irradiated at lower neutron flux and lower irradiation temperature. Another important parameter that can contribute to differences in the local cladding hardness is the axial cladding temperature variation in the reactor. During reactor operation, the cladding temperature varies with axial elevation. Increased temperatures are expected to result in lower hardness values related to irradiation defect annealing. The presence of spacer grids results in local power depressions and cold spots that are expected to produce a higher hardness. However, the degree of change in cladding hardness caused by operational and axial temperature variations may be a smaller effect than local burnup, based on ORNL's dataset. For example, Figure E-44 compares of several measurements at various elevations. Because the local burnup is higher at higher axial elevations, the expected reduction in hardness resulting from the temperature increment might be suppressed by the increase in local burnup.

The effect of heat-treatment on the cladding hardness was investigated by comparing the hardness of the baseline and the heat-treated cladding samples individually, as shown in Figure E-44. Besides the local burnup and axial temperature differences, one possible cause for the reduction in hardness in the heat-treated samples could be the recovery of radiation damage during heat treatment. Previous post-annealing studies performed on the neutron-irradiated Zr-%1Nb-O alloys in a PWR at 320–350°C have shown that preexisting radiation-induced small dislocation loops can grow into large dislocation loops at the expense of small loops during annealing, resulting in a consequent reduction in hardness. Therefore, the initial alloy hardness decreased by ~10% after 50 hours of annealing and by ~91% after 500 hours of annealing at 400°C [E-10]. Consistently, in-situ ion irradiation experiments conducted on Zr-0.1Fe samples showed the initiation of defect movement at ~200–300°C, above which defect movement in the zirconium alloy increased with temperature [E-11]. Also, ~60% of recovery of irradiation hardening was reported after the annealing of several neutron irradiated Zircaloy clad rods at 400°C for ~10 h [E-12]. The FHT rods were held at 400°C for 8 hours to reduce the possibility of irradiation defect annealing. A comparison of the microhardness testing results indicates that the ~4–5% reduction in hardness may have been caused by the FHT. Additional tests will be completed in FY23 that may further elucidate any differences.

Further examinations of microhardness will be conducted at different axial elevations that have similar burnups to understand the effect of axial temperature variations on cladding hardness. The oxide and oxide/metal (O/M) interface may also influence the results of the hardness testing, but for these tests, the indents were formed relatively far away from the O/M interface and the contribution of the O/M interface on hardness results is expected to be negligible. Indents were made on the waterside oxide, resulting in an average hardness of 947 ± 64 HV, but at the 0.1 kgf indention load, the resulting indention size was below the ASTM minimum recommended size and therefore may be inaccurate.

All of the microhardness tests to date have been performed on specimens from the upper elevations of the rod; in FY23 data will be obtained for specimens taken from lower rod elevations.

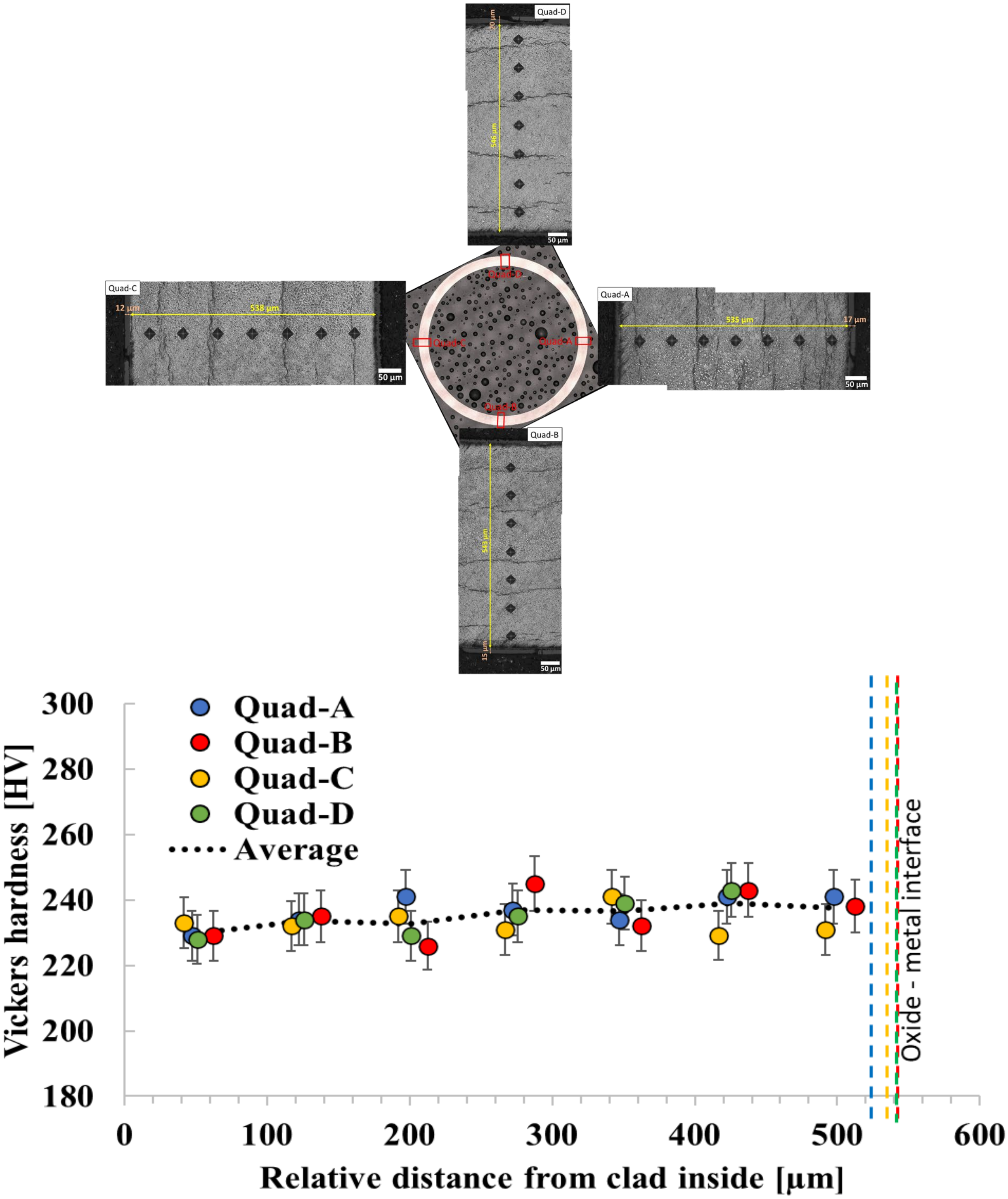

Figure E-32 Micrographs and Vickers Hardness plots for the highlighted region on 30AD05-3240-3259 cladding (×20 lens). Cladding wall and oxide thicknesses are shown on the micrographs.

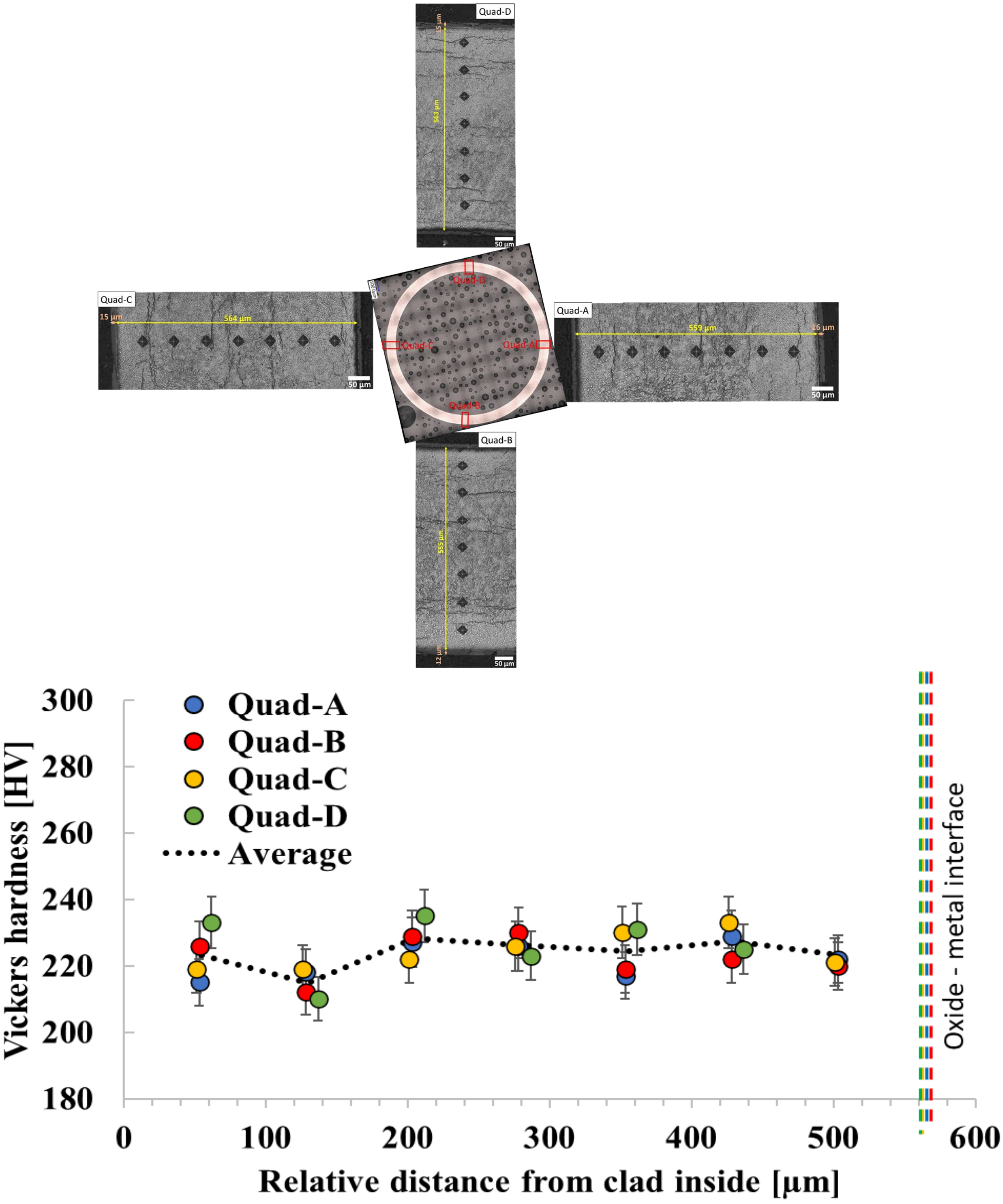

Figure E-33 Micrographs and Vickers Hardness plots for the highlighted region on 30AE14-3399-3418 cladding (×20 lens). Cladding wall and oxide thicknesses are shown on the micrographs.

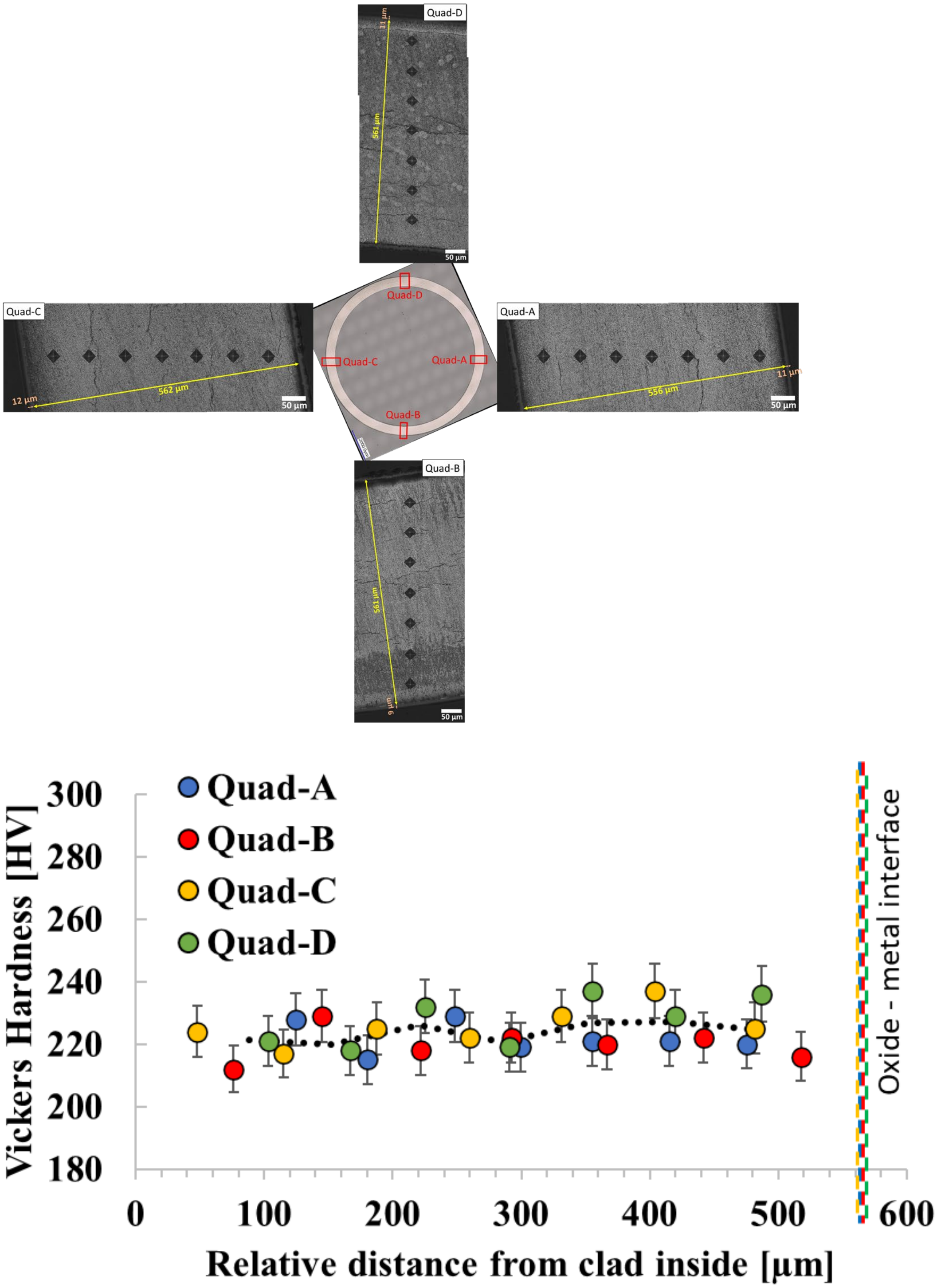

Figure E-34 Micrographs and Vickers Hardness plots for the highlighted region on 30AE14-2675-2694 cladding (×20 lens). Cladding wall and oxide thicknesses are shown on the micrographs.

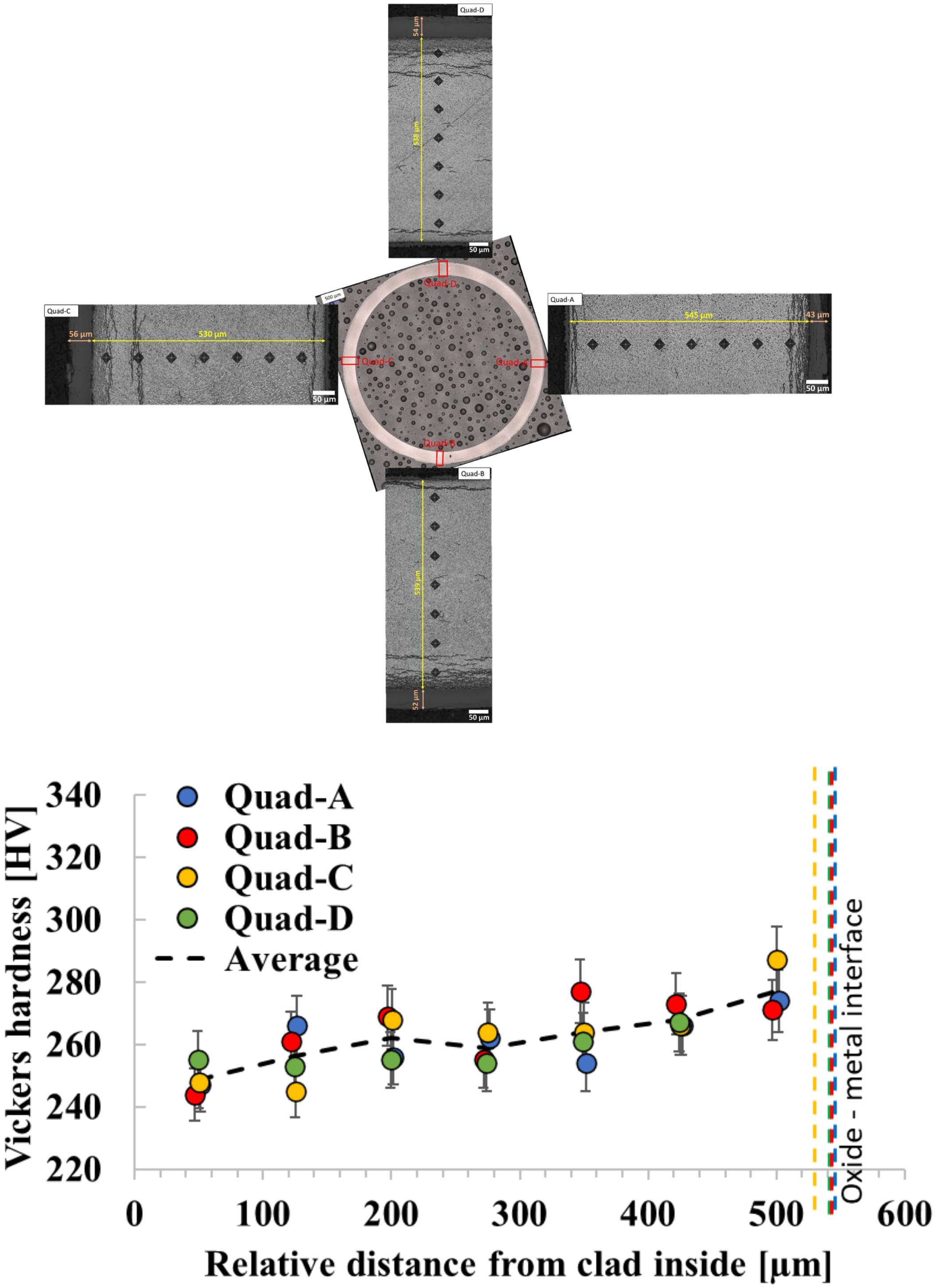

Figure E-35 Micrographs and Vickers Hardness plots for the highlighted region on 3D8E14-3206-3235 ZIRLO cladding (×20 lens). Cladding wall and oxide thicknesses are shown on the micrographs.

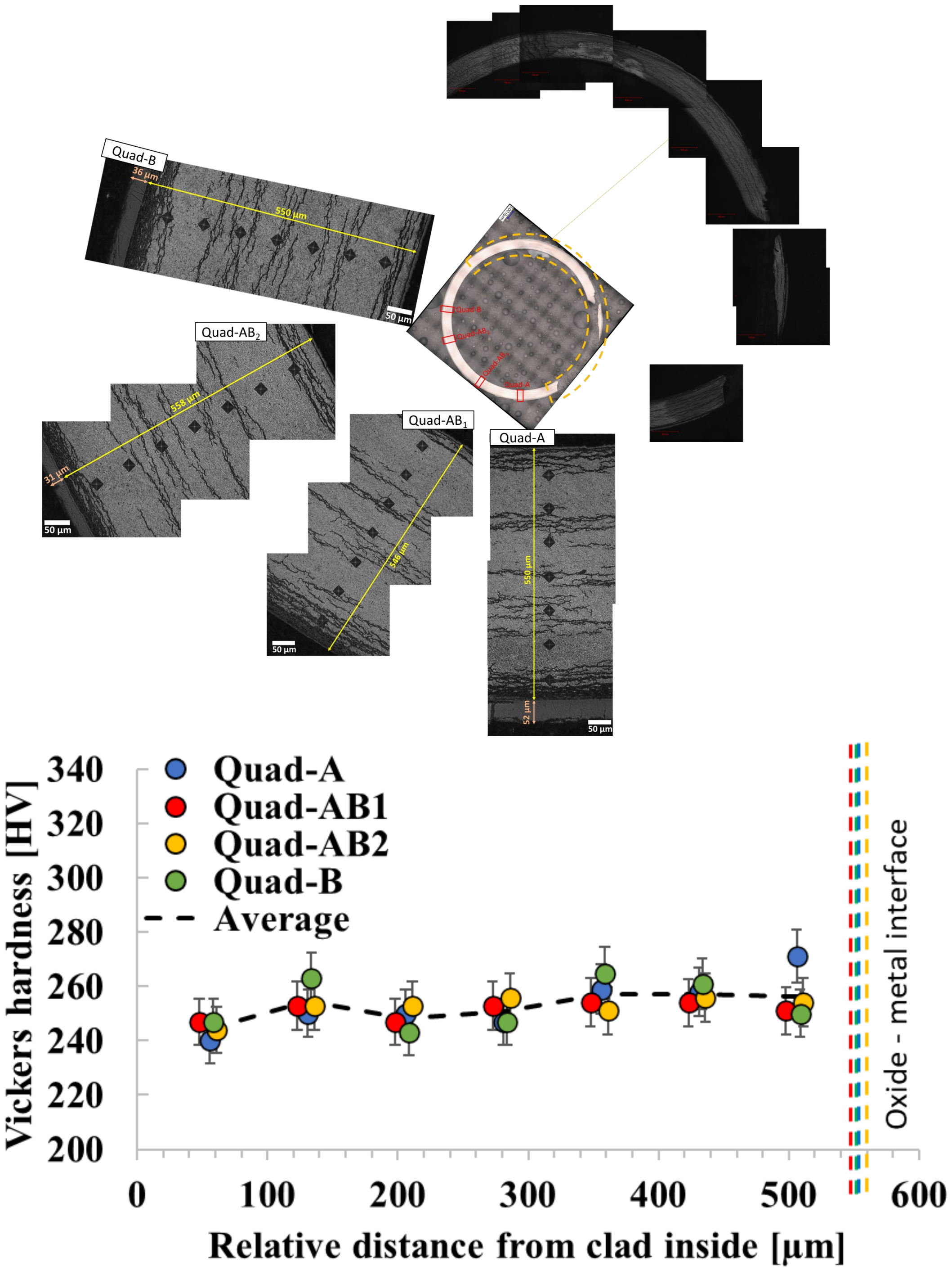

Figure E-36 Micrographs and Vickers Hardness plots for the highlighted region on 3F9N05-3331-3350 cladding (×20 lens). Cladding wall and oxide thicknesses are shown on the micrographs. The dashed line shows the regions where the cladding surface was not suitable for testing.

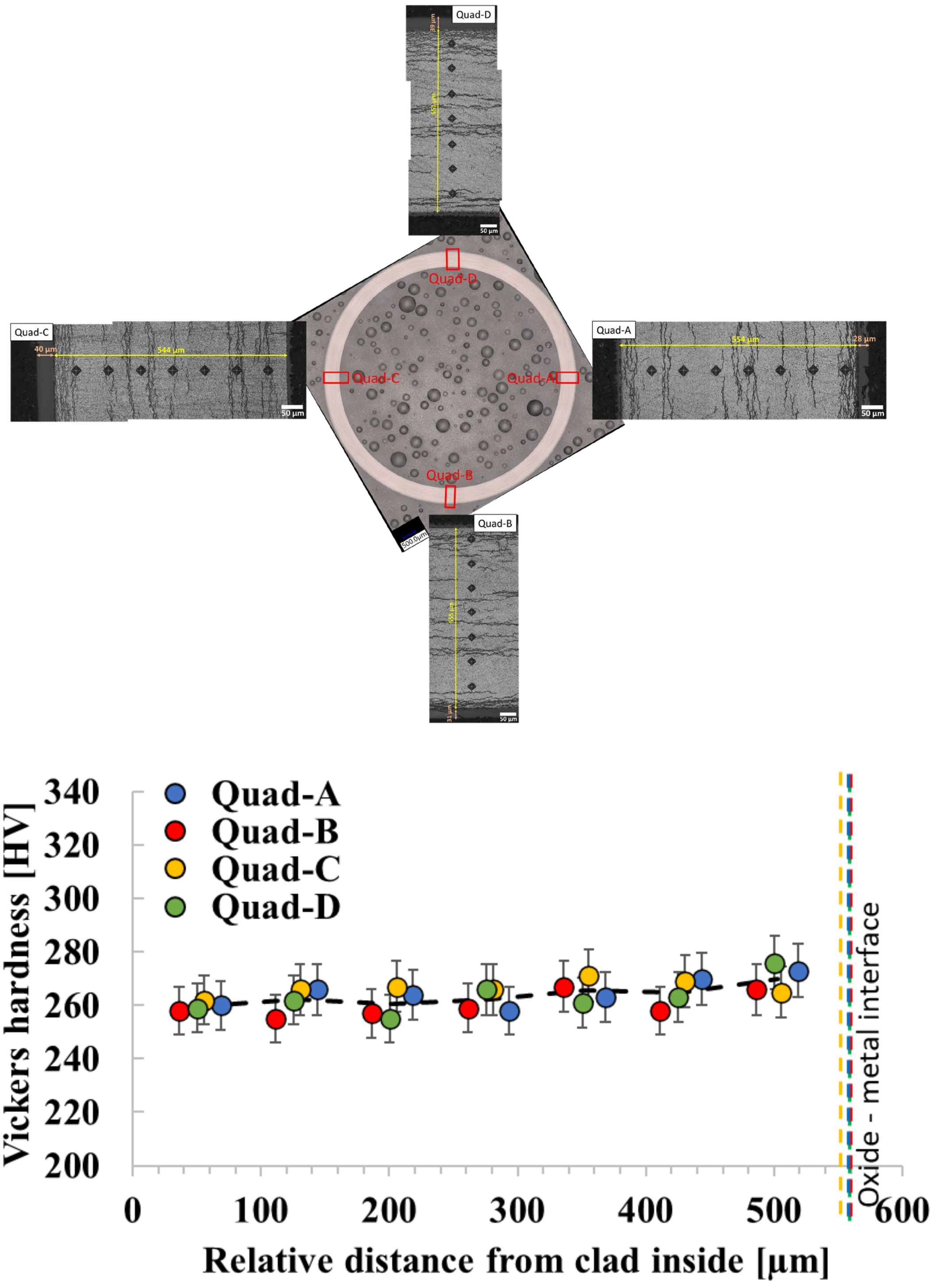

Figure E-37 Micrographs and Vickers Hardness plots for the highlighted region on 3F9N05-2863-2882 cladding (×20 lens). Cladding wall and oxide thicknesses are shown on the micrographs.

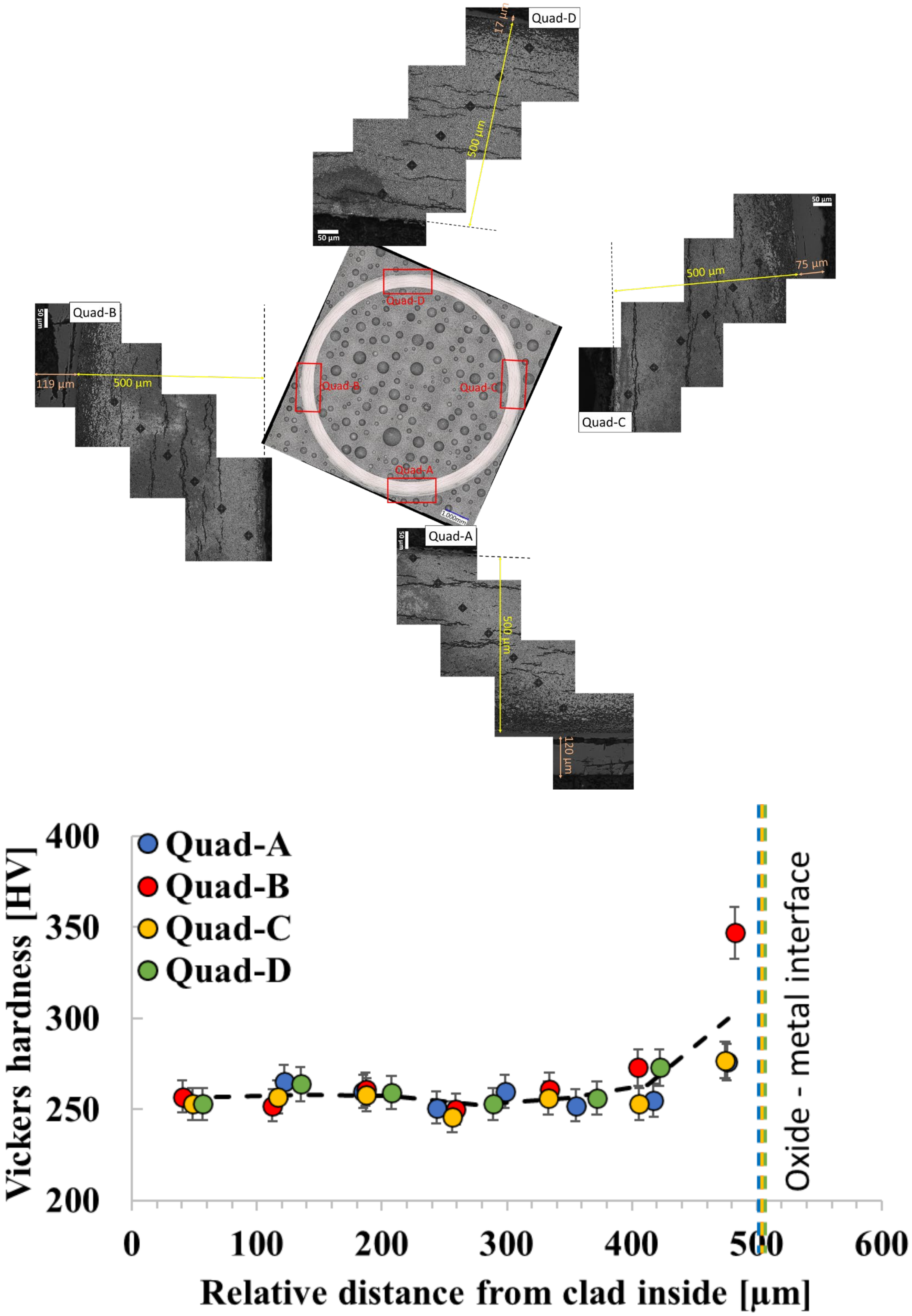

Figure E-38 Micrographs and Vickers Hardness plots for each highlighted regions on 3A1F05-2735-2754 cladding (×20 lens). Cladding wall and oxide thicknesses are shown on the micrographs.

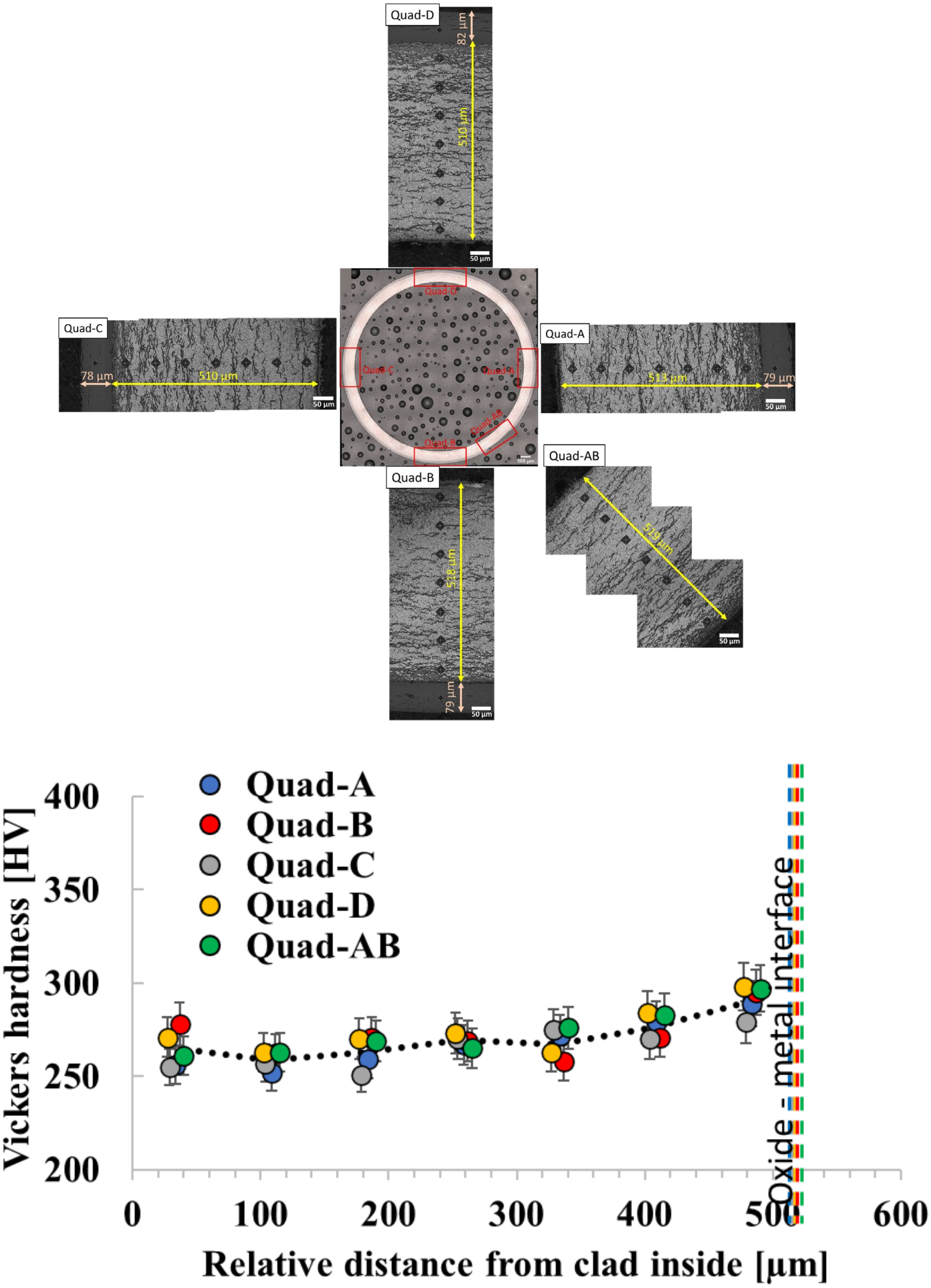

Figure E-39 Micrographs and Vickers Hardness plots for the highlighted region on F35P15-2735-2754 cladding (×20 lens). Cladding wall and oxide thicknesses are shown on the micrographs.

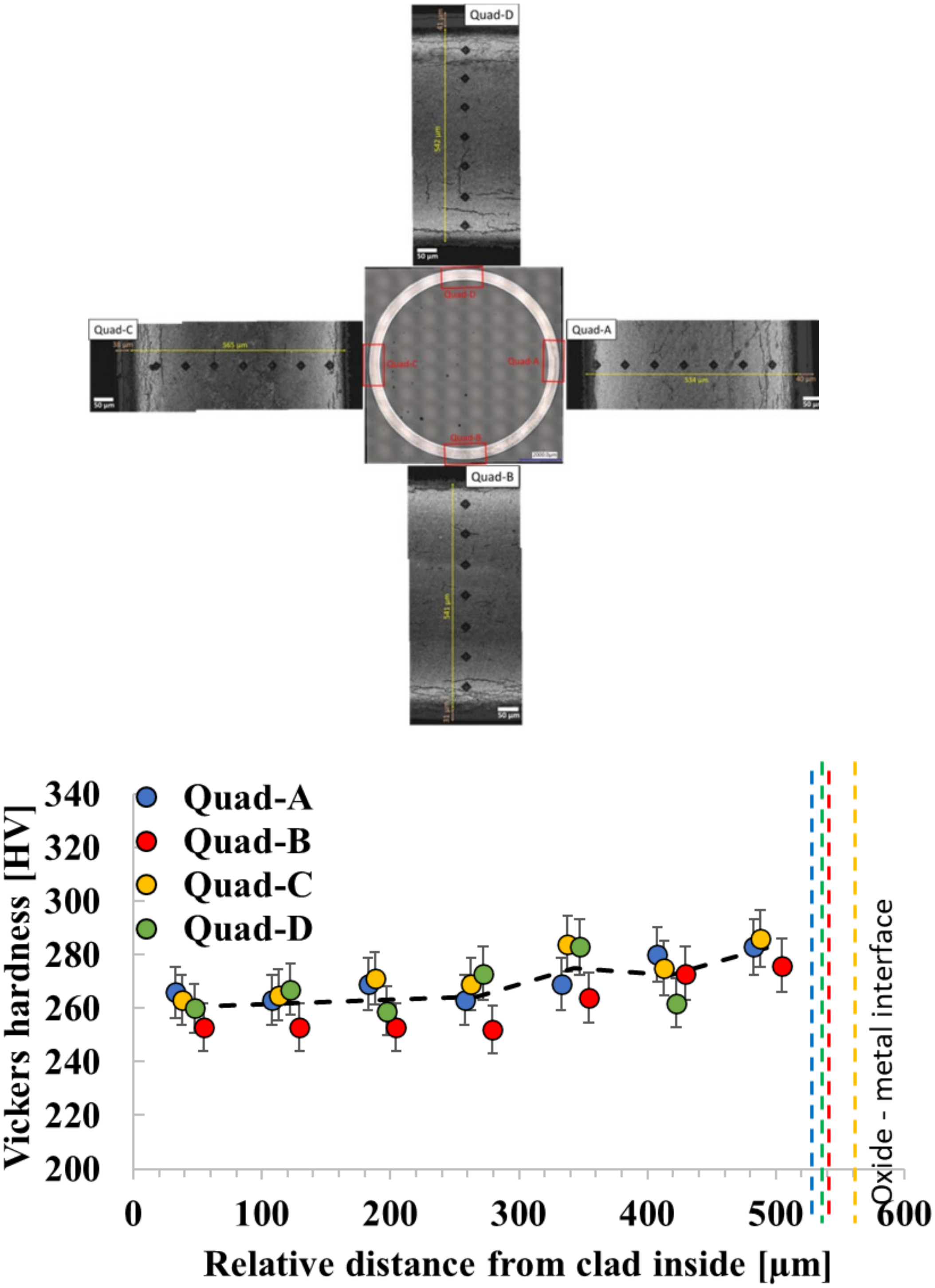

Figure E-40 Vickers hardness values determined for each quadrant from inner to outer cladding of specimen 3D8E14-2655-2674 using an indent of 0.1 kgf. The black dotted line represents the average HV value, and the O/M interface for each quadrant is shown with dashed lines.

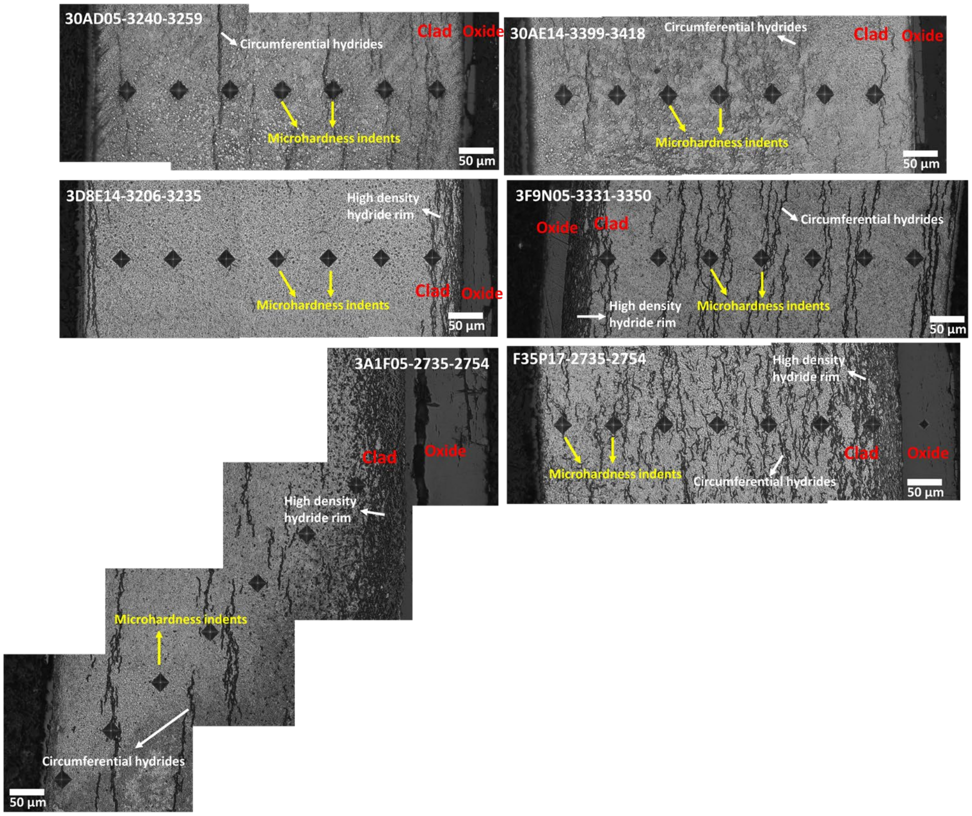

Figure E-41. Microhardness indents formed on selected cladding specimens (highlighted with yellow arrows) using 0.1 kgf (×40 lens).

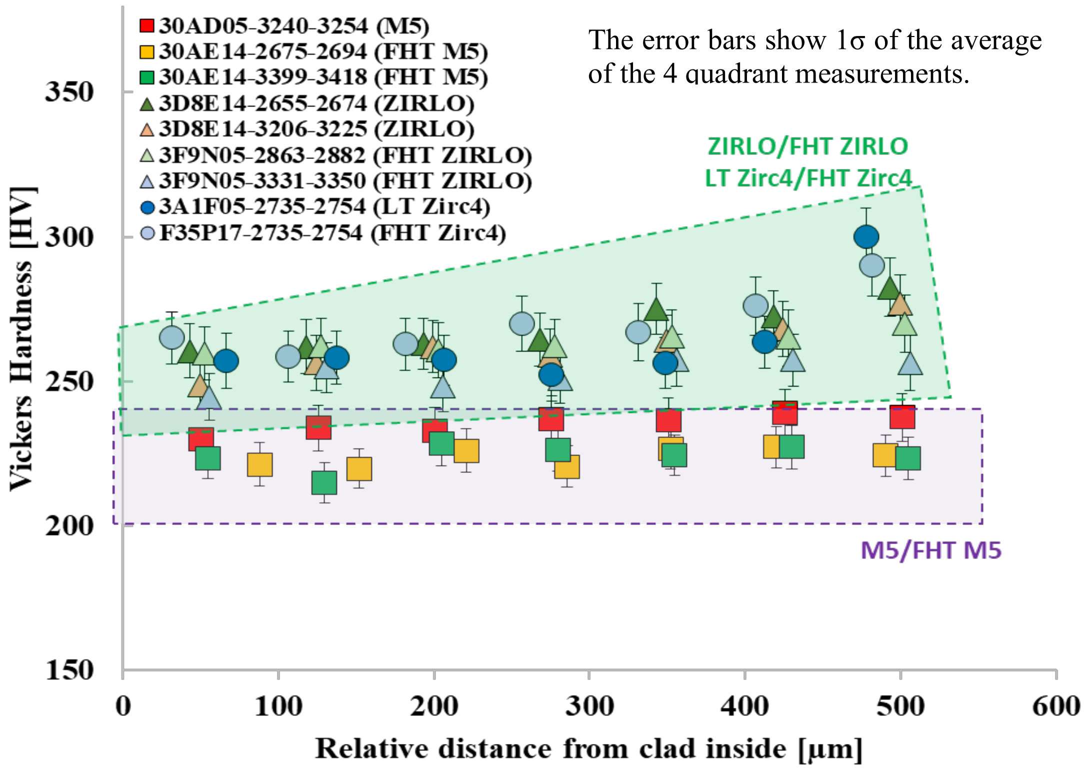

The error bars show 1σ of the average of the 4 quadrant measurements.

Figure E-42. Overall comparison of average Vickers hardness values as a function of cladding alloy type.

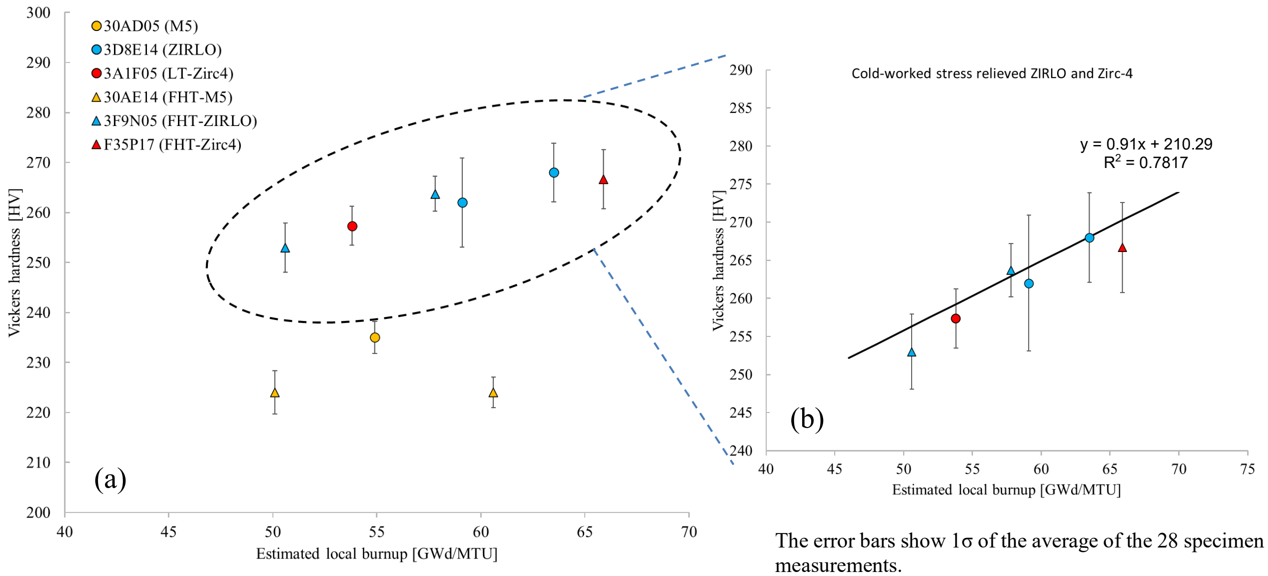

The error bars show 1σ of the average of the 28 specimen measurements.

Figure E-43. Comparison of sister rod cladding Vickers hardness vs. estimated local burnup (cold-worked stress-relieved cladding samples circled with a dashed line (a); corresponding data shown as the inset (b).

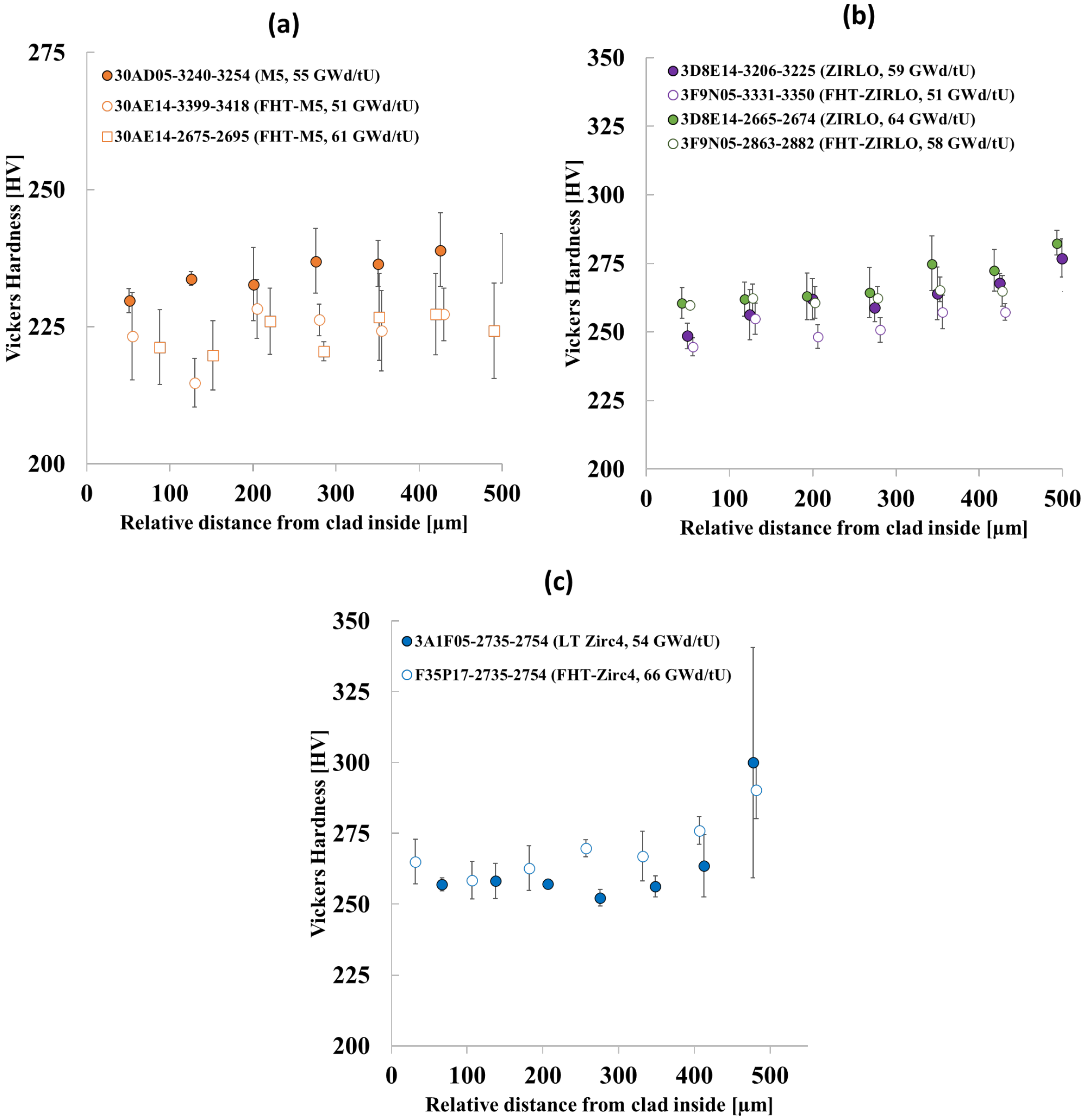

Figure E-44 Comparison of Vickers hardness in baseline and heat-treated cladding samples for (a) M5, (b) ZIRLO, and (c) LT Zirc4 and FHT Zirc4.

E-5. Ring Compression Tests

A significant body of data on cladding hydride reorientation and associated effects on cladding ductility was developed by Argonne National Laboratory (Argonne) over the last decade, with the most recent summary of results documented by Billone et al. in 2019 [E-9]. Several baseline and heat-treated sister rod specimens were shipped to Argonne for cladding ring compression tests (RCTs), and several specimens have been tested [E-9, E-10].

ORNL's data provide supplementary information on the load-bearing capability of intact fuel rods (cladding and pellets). Similar to the RCT of cladding specimens, the fueled rod segment is loaded across its diameter, and the load to specimen failure is measured.

E-5.1 Test Procedure and Data Processing

E-5.1.1 Test Protocol

Instrument and software testing equipment description:

Load frame	Instron 5967
Bend fixture capacity:	30 kN
Voltage:	110/220 V
Software:	Bluehill-3
Furnace:	CP122117 Environmental Chamber and Control Unit
Furnace max temperature:	≤400°C
Scale:	Ohaus Scout NV1201

The RCTs use a pair of 2 in. diameter flat steel compression platens rated to 30 kN. Each specimen is stored separately, and only one specimen is removed from its labeled storage container at a time.

The test specimen is centered on the lower platen using an elastomeric O-ring (RT tests) or a carriage washer (200°C tests). The upper platen is lowered to a position approximately 3 mm above the specimen.

If the test is at temperature, then the furnace door is closed, and heating is initiated. During heating, the upper RCT platen is raised as needed to avoid specimen preload due to thermal expansion of the system.

Once the system is at the specified temperature, the upper RCT platen is lowered to contact the test specimen, as indicated by an increase in load. Care is taken to keep the amount of initial loading small.

The test system is then zeroed, and the test is initiated. All tests are run using a fixed displacement speed of 0.0125 mm/s. The test proceeds until the specimen is fractured.

Following fracture, the specimen, as defined by the fueled pieces within the cladding, is weighed. Any loose particles are weighed. The post-test specimen is placed in a labeled capsule and returned to storage.

E-5.1.2 Test Specimen

The RCT specimens were rough cut to 90 mm. The 90 mm specimens were sub-cut to test specimens that were ~25 mm long for RCT. Each specimen should contain two full pellets. The specimen was sized to avoid pellet loss from the unsupported ends that could invalidate the results, and the 25 mm length was successful for that purpose.

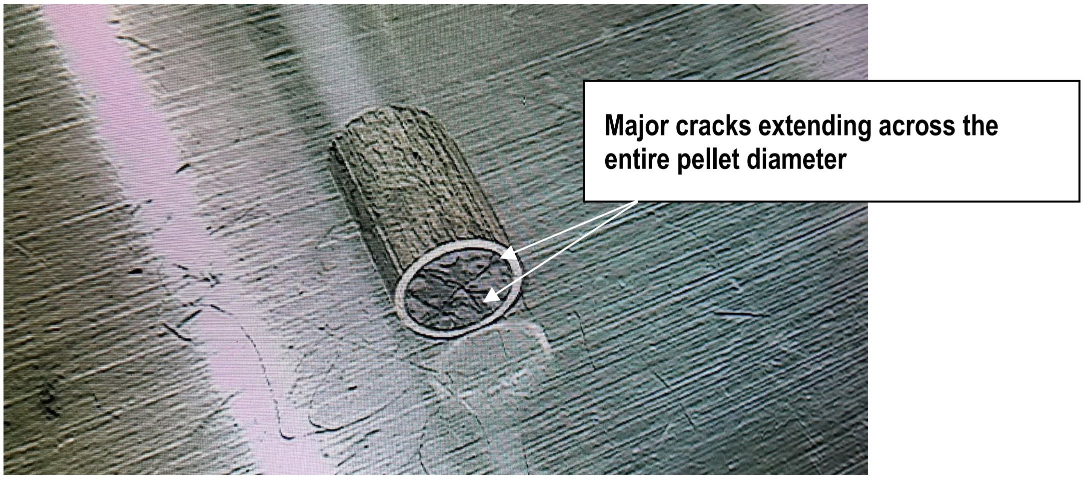

Figure E-45. Typical test specimen.

E-5.1.3 Data Reduction

A typical load vs. a displacement curve, as corrected for machine compliance, is shown in Figure E-46. The specimen takes on load, sometimes with a small drop as the operationally cracked pellets rearrange slightly, until the cladding fractures and the specimen splits open. If the test continues, then the section is crushed and eventually begins to take on load again as the pellet fragments are engaged in the load path. For the purposes of this study, only the peak load achieved is reported.

As discussed in Section E-2.1.2, the load vs. crosshead extension data necessarily includes the machine's compliance. For RCT, the machine compliance is measured by testing an empty pressing die (more than ten times the load frame capacity) using the RCT setup. The corrected displacement is calculated by subtracting the displacement reported in the machine compliance test from the displacement reported in the test of each sister rod specimen.

Unlike the 4PB specimens, the RCT specimens fracture at more than half of the load frame's limit, and the correction made to the RCT displacement is significant. Figure E-47 plots the RCT compliance used in correcting the RCT specimen data.

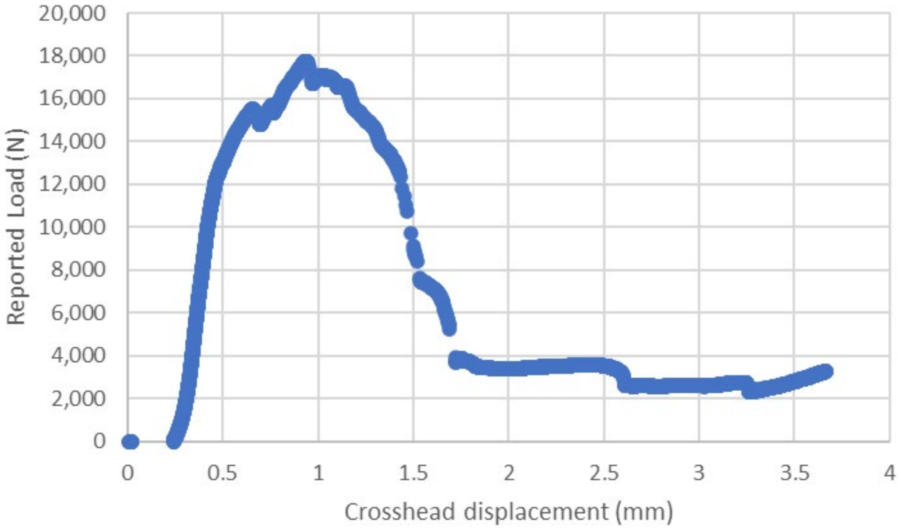

Figure E-46. Typical load vs. crosshead displacement for fueled RCT.

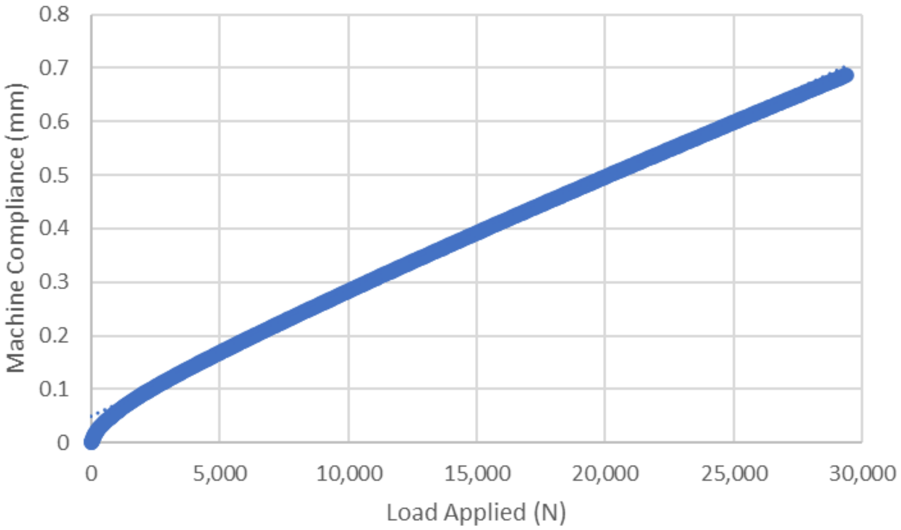

Figure E-47. Measured load frame compliance used to correct RCT data.

E-5.2 Peak Load Data

Table E-8 lists the peak loads recorded for the specimens tested in RCT. The average load-bearing capability of the segments in transverse compression is 16,415 N (3,690 lb_f). As shown in Figure E-48, there is no trend with specimen average burnup, and there is no appreciable difference in the maximum load from RT to 200°C. Cladding type also does not greatly influence the load-bearing capability, and there is no difference related to the heat-treatment applied to some of the rods, as shown in Figure E-49.

Table E-8. RCT peak load data.

Sample ID#	Test temperature (°C)	Cell temperature (°C)	Cladding alloy	Heat-treatment	Estimated specimen burnup (GWd/MTU)	Peak load (N)	Peak load (lb_f)
30AD05-2320-2345	25.2	25.2	M5	---	59	17,985	4,043
30AD05-3150-3175	25.3	25.3	M5	---	56	17,000[a]	3,822[a]
30AE14-2585-2610	25.9	25.9	M5	FHT	60	17,632	3,964
30AE14-3418-3443	25.9	25.9	M5	FHT	47	19,510	4,386
3D8E14-2322-2347	25.1	25.1	ZIRLO	---	64	15,788	3,549
3D8E14-3116-3141	25.1	25.1	ZIRLO	---	60	17,210	3,869
3D8E14-2347-2372	200	26.2	ZIRLO	---	64	17,752	3,991
3F9N05 -2482-2507	25.6	25.6	ZIRLO	FHT	59	17,444	3,921
3F9N05-3350-3375	25.6	25.6	ZIRLO	FHT	50	17,049	3,833
3F9N05-3375-3400	200	25.8	ZIRLO	FHT	50	18,683	4,200
3A1F05 -3124-3149	24.8	24.8	LT Zirc-4	---	52	12,303	2,766
3A1F05-2645-2670	24.9	24.9	LT Zirc-4	---	55	16,232	3,649
3A1F05-2670-2695	200	25.8	LT Zirc-4	---	55	12,384	2,784
F35P17-2645-2670	25.7	25.7	Zirc-4	FHT	51	12,476	2,805
F35P17-2960-2985	25.7	25.7	Zirc-4	FHT	50	12,961	2,914
F35P17-2670-2695[b]	200	25	Zirc-4	FHT	51	15,915	3,578
F35P17-2985-3010[c]	200	25.3	Zirc-4	FHT	50	12,500[a]	2,810[a]
					Maximum	20,732	4,661
					Minimum	12,303	2,766
					Average	16,415	3,690

a. The data file was not saved for this test. The value is from the estimate recorded in the laboratory notebook.
b. A major pellet crack as aligned with the loading direction.
c. A major pellet crack as aligned perpendicular to the loading direction.

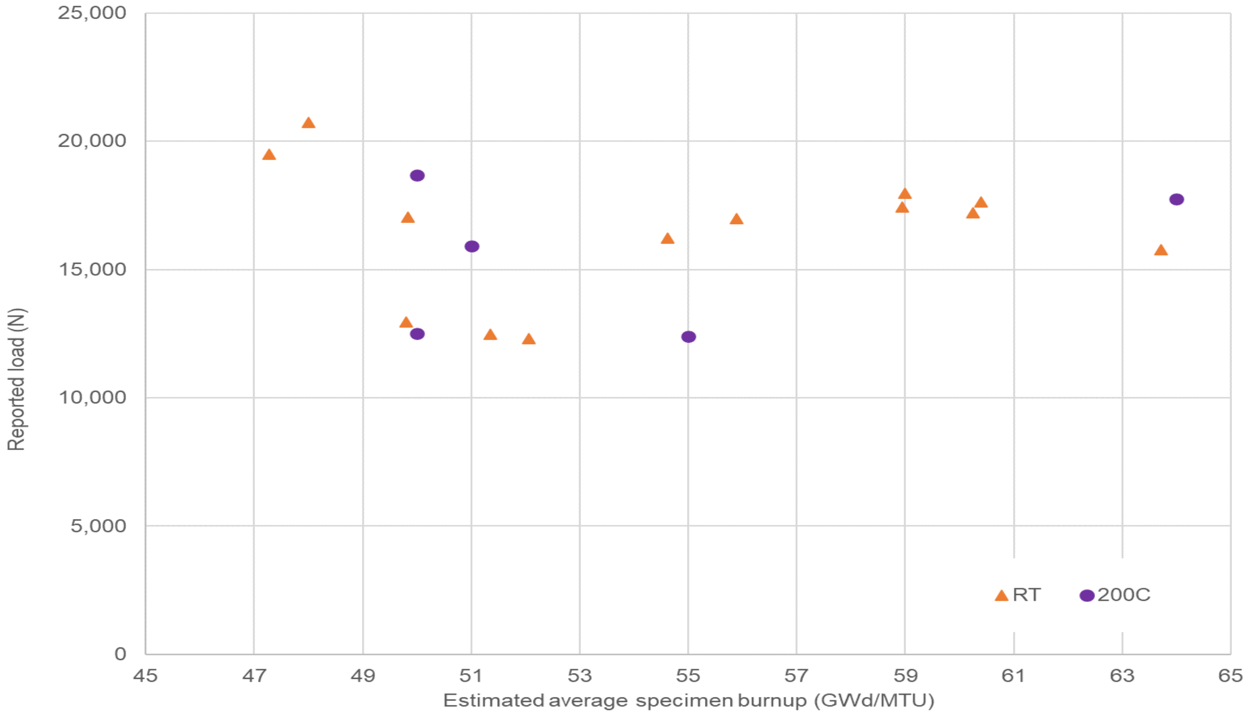

Figure E-48. Maximum RCT load vs. estimated average specimen burnup at RT and 200°C RCT.

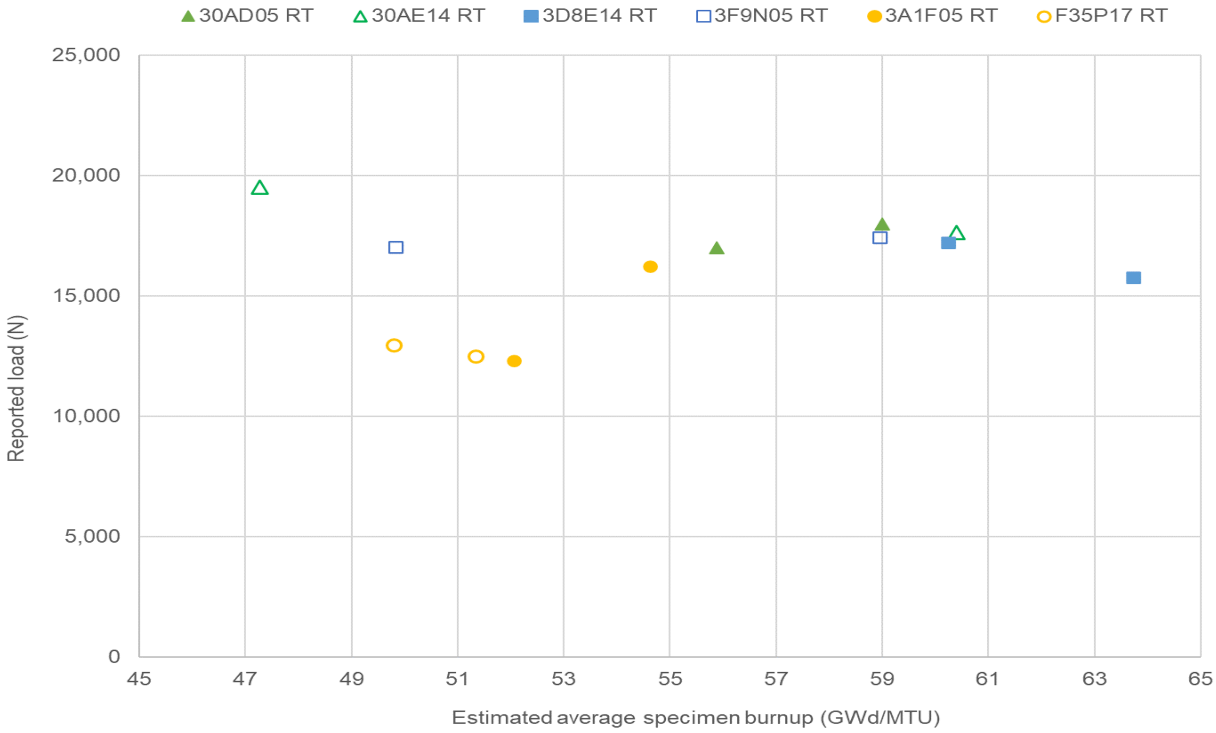

Figure E-49. Maximum RCT load vs. average specimen burnup at RT for baseline and FHT specimens.

The results for a ZIRLO-clad fueled RCT are compared with results from a defueled ZIRLO RCT [E-9] in Figure E-50. The fueled cladding carries about eight times the load of the defueled cladding, but it fractures at a much lower displacement because it is constrained by the pellet. The defueled RCT's predictably fracture at the 3 and 9 o'clock cladding positions [E-9, E-15], whereas the fueled RCTs fracture at a major pellet crack.

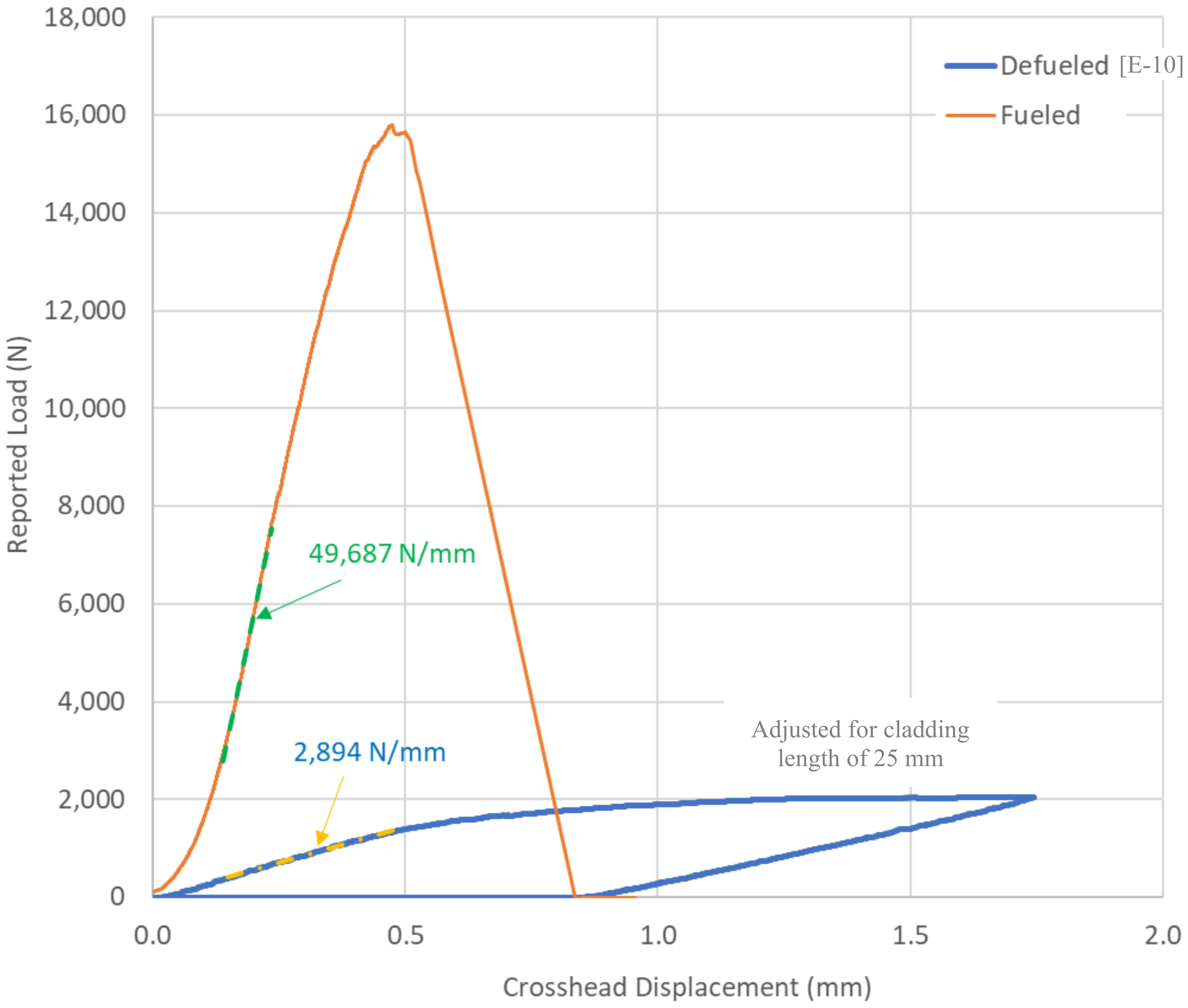

Figure E-50. Comparison of load vs. crosshead displacement for a ZIRLO sister rod specimen, fueled and defueled.

E-5.3 Typical Fracture Observed

The specimens typically carried load until at least one cladding fracture developed. As shown in Figure E-51, specimens frequently broke into two equal halves. As the tests progressed, it became clear that fracture typically occurred at the location of one of the major diametrical pellet cracks, as illustrated in Figure E-52. Usually, there were two major cracks (defined as *full-diameter cracks*) visible at the end of the specimen. Two specimens from F35P17 were tested with the major crack aligned along the loading path and perpendicular to the loading path. There was a difference in the results for those two samples, but unfortunately, the data were not recorded within the software for one of the tests, and only the notation on peak load in the laboratory notebook is available, which is not exact.

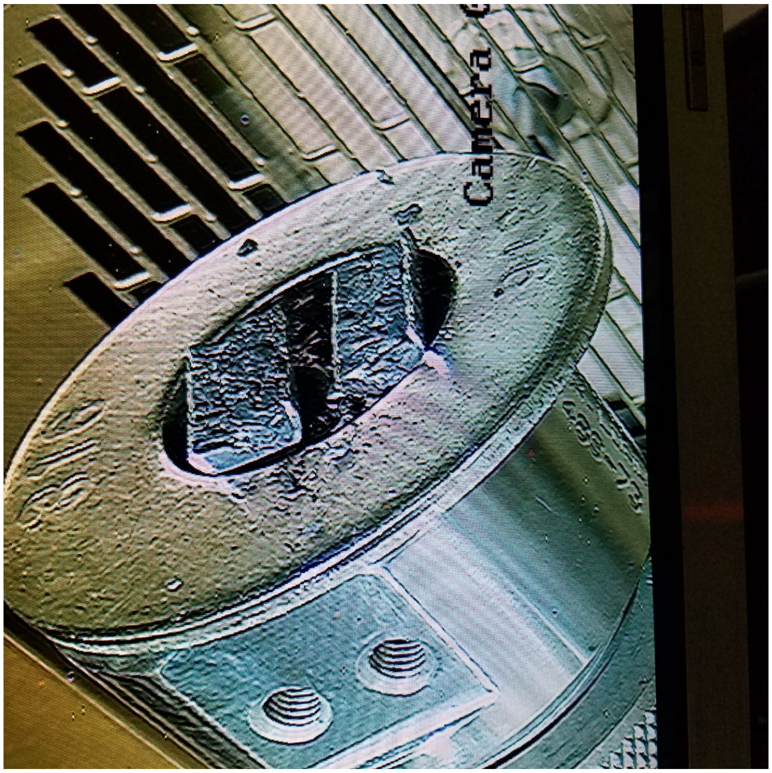

Figure E-51. Typical post-RCT appearance.

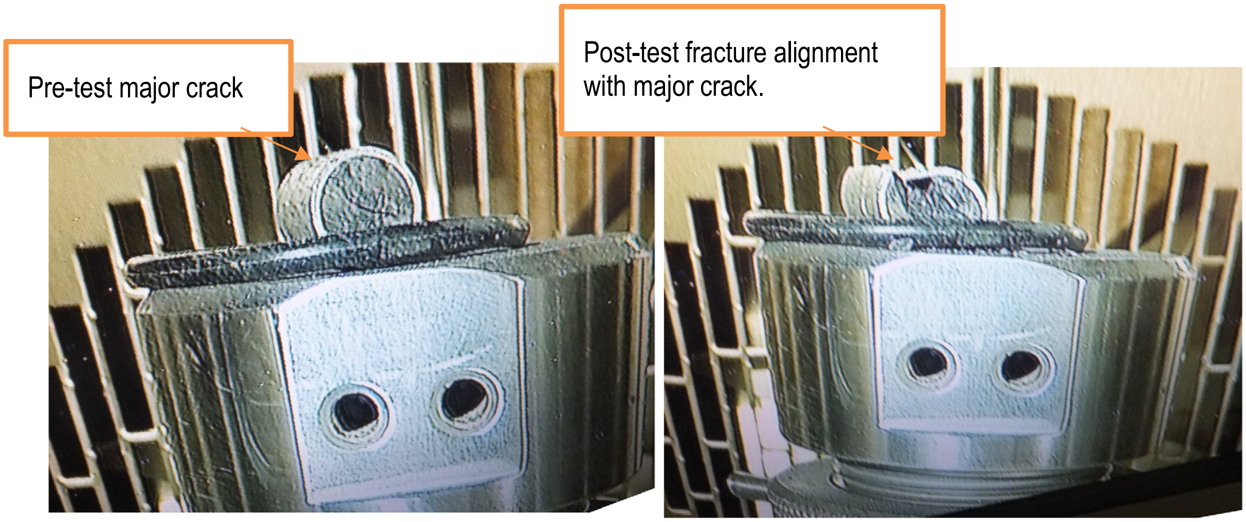

Figure E-52. RCT fracture path along major pellet crack.

E-5.4 Finite Element Modelling of Ring Compression Testing

To better understand the effects of cladding properties and pellet deformation characteristics, finite element modeling of the RCT was performed using ANSYS Workbench 2022 R1. The pellet is modelled as a collection of pellet pieces that deform in shear by the relative motion of those pieces. The approach is to use M5 data to calibrate the inputs for the pellet deformation and cladding performance model. The expectation then is that the pellet deformation model will be applicable to the Zircaloy-4 data and the failure strains in the Zircaloy-4 cladding with its larger oxide thickness and hydrogen content will be lower than the M5 cladding. The finite element model can then be used to estimate the decrease in failure strain of the Zircaloy-4 cladding, which gives rise to the lower peak values.

The RCT pellet and cladding model consisted of isotropic material properties for the cladding and the pellets. The RCT finite element model comprised of a 10 mm sister rod segment with a 9.5 mm diameter cladding. The pellets were assembled inside the cladding with a surface-to-surface contact (to transfer frictional and compressive loads) between the OD of the pellet and the inner diameter of the cladding. Additionally, a surface-to-surface contact of the pellet with another pellet was established to capture relative motion of the pellets inside of the cladding.

To better understand the response of the cladding and pellet when subjected to a ring compression test, the pellets were modified with various cracks through the thickness of the pellets. Three versions of pellet cracking were examined: (1) a wedge model, (2) a half-pellet model, and (3) an actual crack pattern model, as shown in Figure E-53. The wedge pellet design contained eight pellet wedges at 45° increments and included two cross-sectional cuts at 1/3 of the pellet axial length (48 independent pellets wedges), as discussed in Section E-2.4. This model will be referred to as the wedge model. Secondly, the pellet was cut into two halves. Finally, the cracks in an actual sister rod specimen (3F9N05-0700-0719 as shown in Appendix B, Figure B-23) were digitized, as shown in Figure E-53. and Figure E-54. This model will be referred to as the actual crack model. It should be noted that the actual crack model uses the same crack pattern through the entire depth of the test piece, while a real pellet would have varying degrees of cracking throughout.

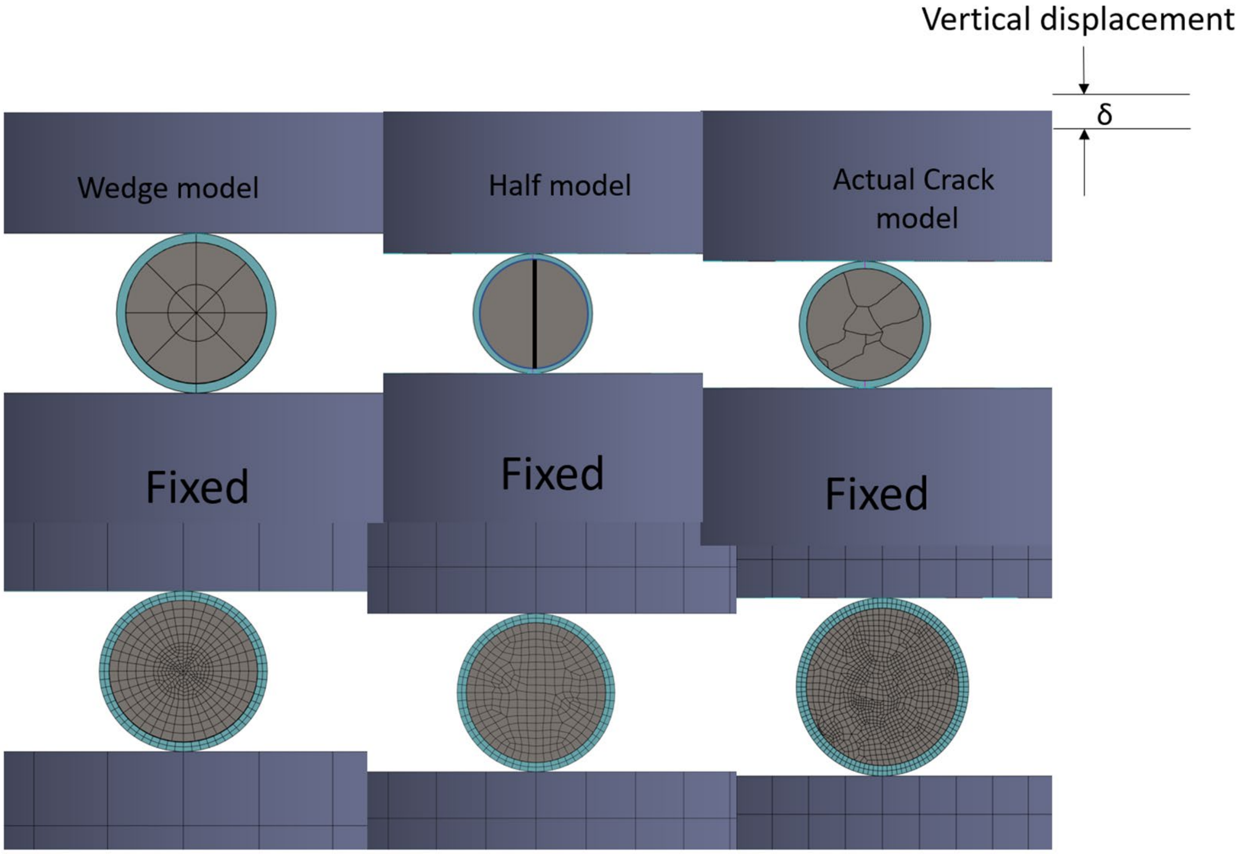

Figure E-53. Finite element model of ring compression test. The top images show the different pellet fragment shapes; the bottom image shows the mesh used for the finite element analysis.

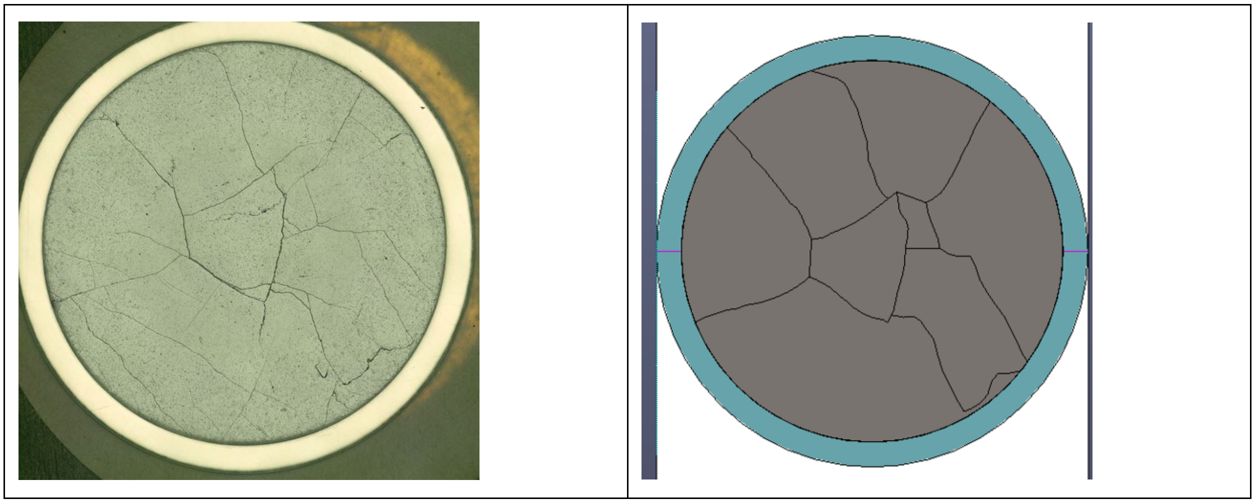

Figure E-54. RCT FE model with actual cracks.

The finite element model comprised +65K solid elements and +77K nodes for the pellet wedges and the cladding. The elements were linear and had an average mesh size of 5mm. The pellet-to-pellet and pellet-to-cladding connections consisted of a frictional contact with a friction coefficient of 0.2 as a lower bound; higher friction coefficients result in larger reaction loads. No surfaces were constrained to simulate pellet-to-cladding bonding. A no-separation contact was assigned for the cladding to lower and upper fixture supports. The no-separation contact enabled the cladding to move in plane with respect to the supports and transfer compressive forces between the two components.

All components in the FEA model were modeled as isotropic materials with RT material properties. The cladding was modeled by using elastic-plastic Zirc-4 material properties (Ref. [E-16.]), and the pellets were modeled as ceramic UO_2 [E-18.] . The linear material properties used are provided in Table E-9.

Table E-9. Elastic properties of the four-point bend model.

	Elastic Modulus (GPa)	Poisson’s Ratio
Cladding	91	0.37
Test fixture supports	200	0.30
UO_2 pellet wedges	200	0.32

A displacement input was set on the upper fixture. The upper fixture was fixed in the in-plane direction and was free to move in the vertical direction. Through the no-separation contact between the fixture and the cladding outer surface, the upper support contacts the cladding, causing it to compress. Through the cladding-to-pellet contact, the compressive load travels down through the pellet and cladding onto the lower fixture. The bottom support is fixed in all three directions of freedom. Rigid body motion of the cladding was realized through the friction coefficient between the cladding and the fixture. As the fixture displaces, a compressive load is applied to the cladding outer surface. The compressive load generates a frictional force. Since the model is not subjected to any in-plane loads, the cladding is essentially constrained in the in-plane direction. The force required to generate the displacement input was extracted from the output results and compared with the experimental data.

The initial baseline simulation used the UO_2 pellet material property from the material properties table. A displacement boundary condition of 0.5 mm was applied to the upper fixture, and the reaction forces were extracted from the output after the analysis. The results were compared with the experimental reaction force-displacement graph in Figure E-46.

The response the wedge model (see Figure E-53), resulted in a stiffer reaction load when compared to the results from a typical RCT test (Figure E-46). As the fixture compresses the cladding and pellets, the top two wedges slide down and push the left side wedges and right side wedges outward in the radial direction, as shown in Figure E-55 and Figure E-56. When the displacement is set to 1 mm, the reaction is 10% greater than the experimental result. Displacement simulations greater than 1 mm resulted in model instabilities.

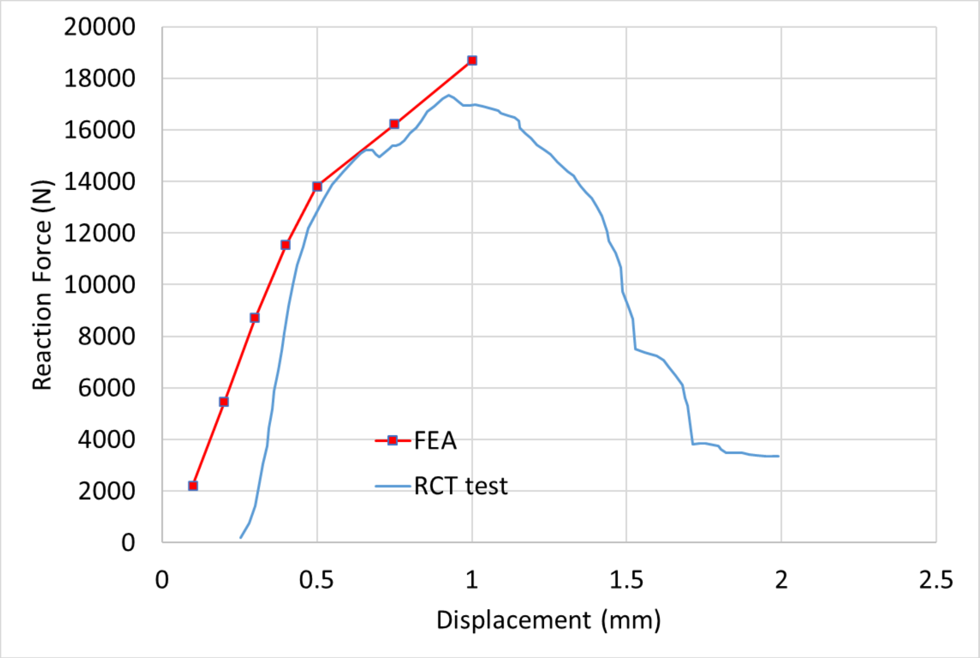

Figure E-55. Force-displacement comparison of the RCT test with FEA simulation.

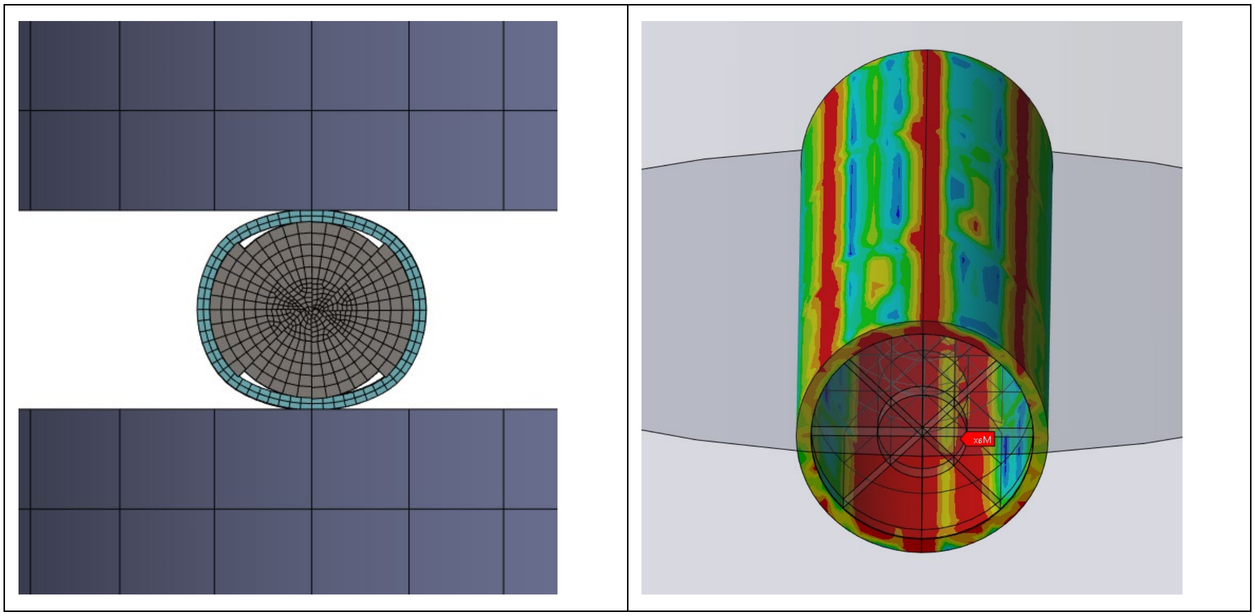

Figure E-56. RCT simulation result of pie wedge pellets.

The half pellet model (see Figure E-53. B) provided similar results. The simulation was run with the parting plane oriented vertically (shown as 90° in Figure E-57), 45°, and 180°. The results, shown in Figure E-57. , are very stiff and produce much larger reaction loads than those measured during an actual test. The reaction load 90° is 806% greater than the measured data, at 45° it is 171% greater, and at the 180°

orientation it is 814% greater than the measured data. When the parting plane of the half pellet model is aligned in the vertical direction, the halves bow outward along the parting plane, creating a central gap. Because the cladding is not constrained (bonded) with the pellet OD, it is allowed to lift off and deform independently. The response is very similar when oriented at 180°, except that the central parting plane gap is not formed. When aligned at 45°, the top half slides down, resulting a more localized load on the cladding, and this response is more consistent with test observations, although the reaction loads from the model are much too high.

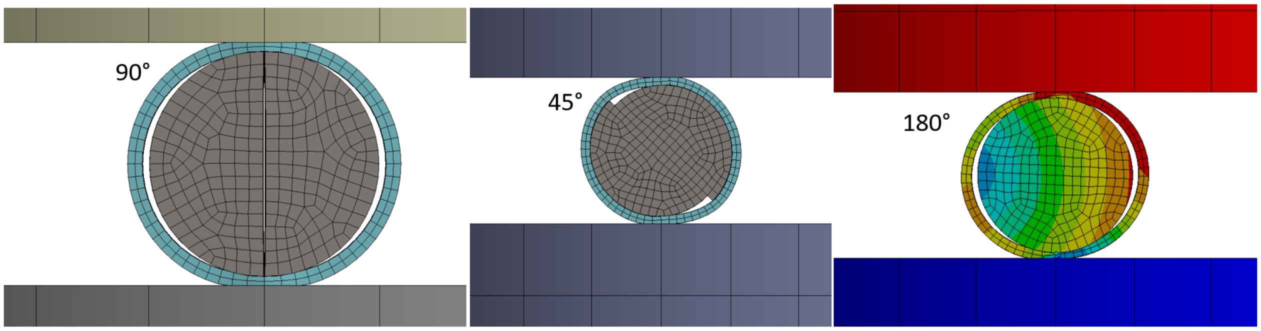

Figure E-57. RCT simulation result of two halves pellet.

The actual crack model was also evaluated at three different rotations, as shown in Figure E-58. The reaction load for the actual crack 0° model was 49.6 kN (or ~290% greater than the measured data), 54.4 kN for the at 45° of rotation (or ~320% greater than the measured data), and 80.2 kN at 90° of rotation (or 477% greater than the measured data). The 0° rotation resulted in the least reaction load when compared to the variations examined. The results are shown in Figure E-58.

From RCT modeling results shown, it appears that the original pellet crack configuration is not as important as initially expected. It appears that what is physically happening is that as the pellet is compressed new fractures are occurring and the pellet fragments are sliding on the newly formed shear lines.

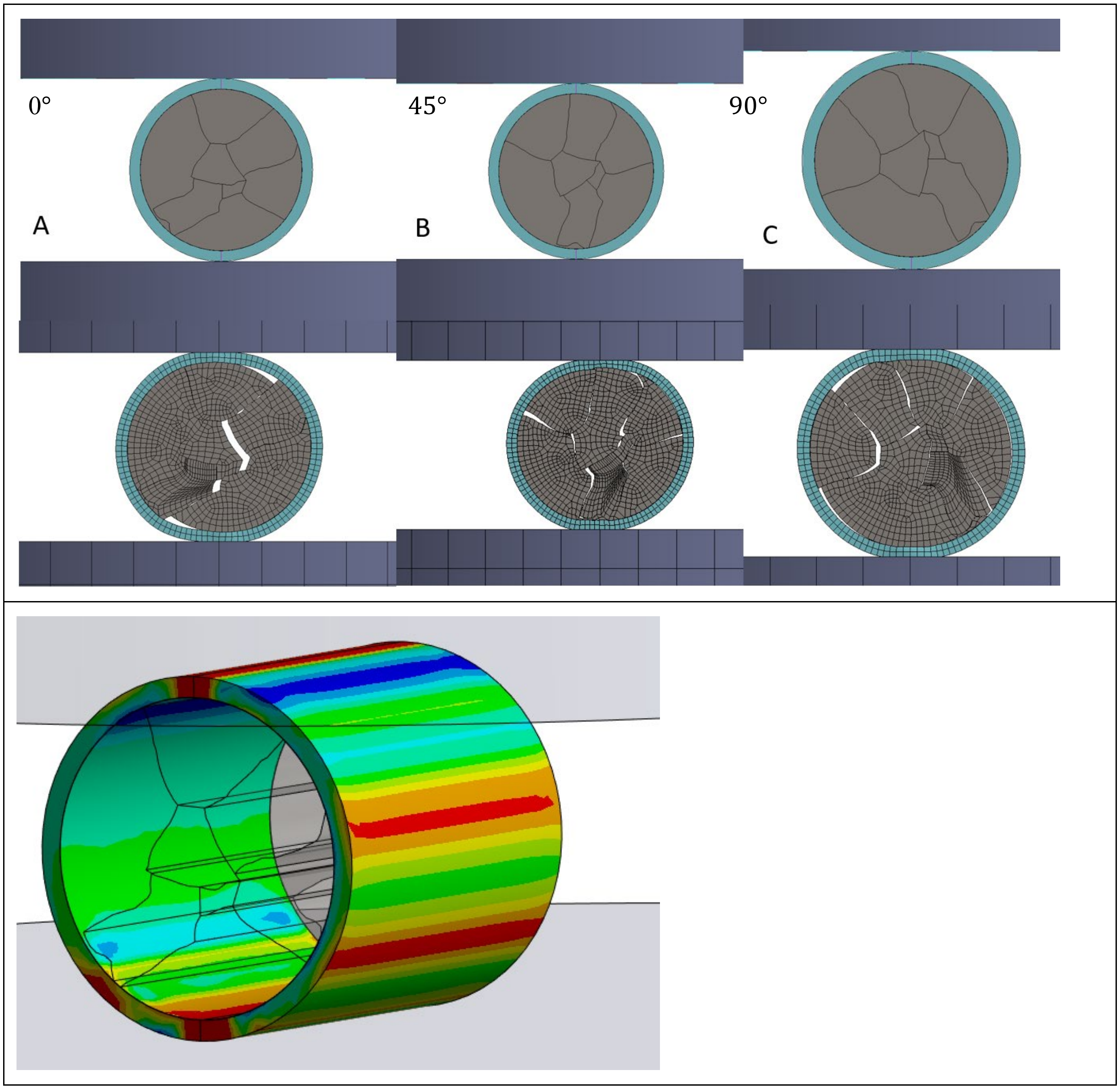

Figure E-58 Pellet response of the actual crack model.

To investigate the impact of friction on the reaction load in RCT testing, a parametric study was conducted. This study involved varying the frictional interaction between pellets and between the cladding and the pellet, ranging from low friction (0.2) to high friction (1.0). Initially, the friction coefficients between the cladding and pellet were set to be equal and then were systematically adjusted within the range of 0.2 to 0.8. The analysis yielded the reaction load of the RCT test for a displacement of 0.5 mm.

Under conditions of low friction (μ = 0.2), the resulting reaction load was determined to be 21.9 kN, which corresponds to 75% of the experimental data. Conversely, when the friction coefficient was raised to its maximum value of 0.8, the reaction load escalated to 78.6 kN, approximately five times greater than the experimental data. The relationship between the friction coefficient, which ranges from 0.2 to 0.8, and the reaction load, exhibited a fourth-order polynomial trend (Figure E-59).

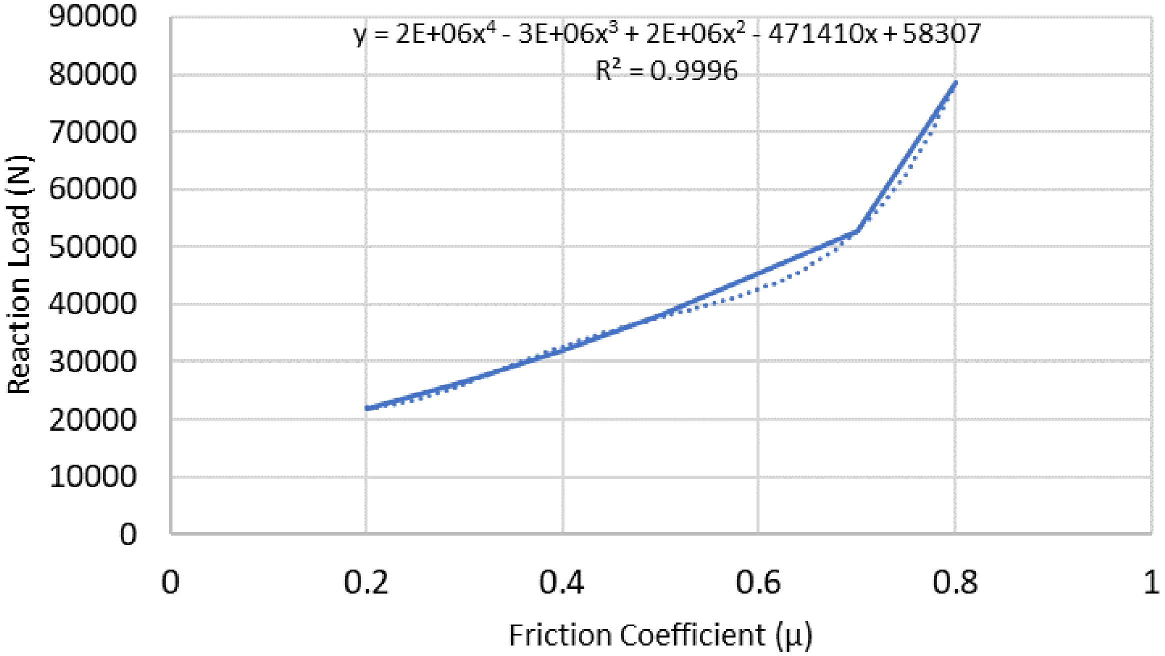

Figure E-59. Reaction load as a function of friction coefficient.

The finite element model involved two input parameters for frictional coefficients: (1) cladding-to-pellet, and (2) pellet-to-pellet. To gain a better understanding of the individual influence of each frictional coefficient on the RCT reaction load, one of the frictional coefficients was altered while the other was kept constant. Initially, the cladding-to-pellet friction coefficient was adjusted, ranging from a low value of 0.2 to a high value of 1.0. The pellet-to-pellet friction coefficient was held steady at 0.3, and the RCT displacement remained fixed at 0.3 mm.

For the low frictional value (μ = 0.2), the resulting reaction load was 9,885 N, whereas for the high frictional value (μ = 1.0), the reaction load was 10,366 N. The chart below illustrates how the reaction load responds to the increasing pellet-to-cladding friction coefficient. Interestingly, a 500% increase in the friction coefficient from the low friction condition led to an increase of only 4.5% in the reaction load compared to the low friction scenario. This suggests that the frictional contact between the pellet and cladding has a minimal impact on the reaction force when a rod undergoes a ring compression test (Figure E-60).

Subsequently, the pellet-to-pellet frictional coefficient was subjected to variation, while the pellet-to-cladding friction coefficient constant was kept at μ = 0.2. Additionally, the displacement was altered within the range of 0.2 mm to 0.7 mm (Figure E-61). The graph depicted below demonstrates a notable trend: as the pellet-to-pellet friction coefficient increases, the linear slope of the force displacement curve also increases. Notably, a frictional coefficient of μ = 0.4 exhibits good agreement with experimental data; however, the maximum reaction force it produces is approximately 47% greater than that given in the test data.

The RCT test was performed on a fuel rod pellet that featured initial cracks, as illustrated in Figure E-58 and Figure E-52. As the compression displacement increases, the pellets undergo shifts, slides, and movements relative to each other. This behavior results in a lower reaction load and a force-displacement curve that deviates from linearity at displacement values greater than 0.2 mm. It is important to note that the finite element analysis employed in this study is a static analysis with nonlinear material properties and does not capture the pellet-to-pellet nonlinear interaction behavior, including shifting, sliding, and rigid body motion.

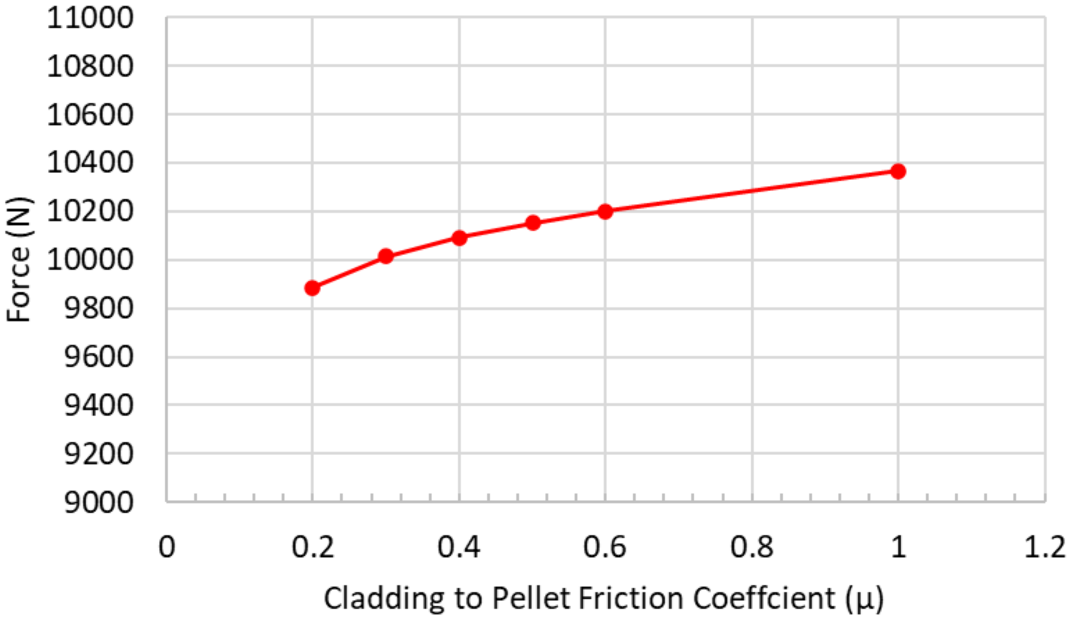

Figure E-60. Reaction load as a function of cladding to pellet friction coefficient.

To potentially predict such complex pellet-to-pellet behavior involving nonlinear interactions, shifting, sliding, and rigid body motion, an explicit dynamic analysis such as that obtained using ANSYS LS-DYNA may be considered. ANSYS LS-DYNA is a widely utilized finite element analysis software package designed specifically for simulating intricate, nonlinear, dynamic phenomena in materials, structures, and systems. It is part of the comprehensive ANSYS suite of simulation tools and is especially well-suited for modeling high-speed impact events, crash simulations, and manufacturing processes characterized by extreme deformation and large strains.

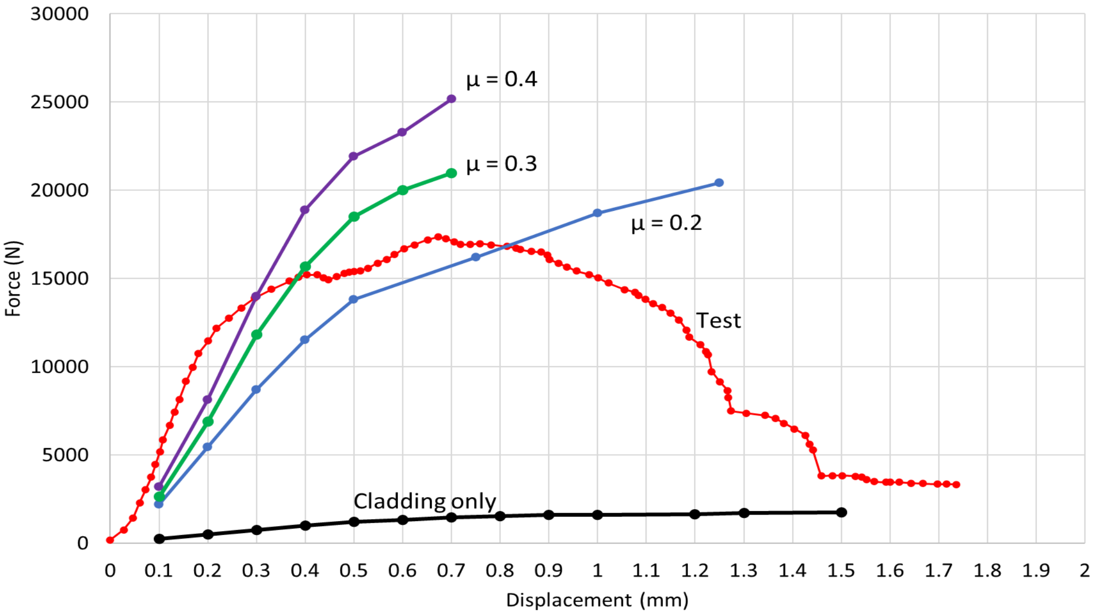

Figure E-61. Reaction load as a function of displacement.

The pellet-to-cladding model underwent analysis using ANSYS LS-DYNA to simulate pellet failure through element deletion during a ring compression test. In this simulation, the elements within the pellet were configured to fail and to be deleted when their true strain reached the failure strain. Given that the pellet is made of a brittle material, it does not exhibit ductile behavior, and failure occurs at a strain close to the yield strain. For this analysis, the failure strain was set at 2.2%.

To control displacement, a boundary condition was applied at the top of the fixture, causing it to displace by 0.5 mm with an end time of 0.5 seconds, as shown in Figure E-62. To expedite the simulation and reduce runtime, mass scaling was employed which involves adding nonphysical mass to the structure to allow for a larger explicit time step.

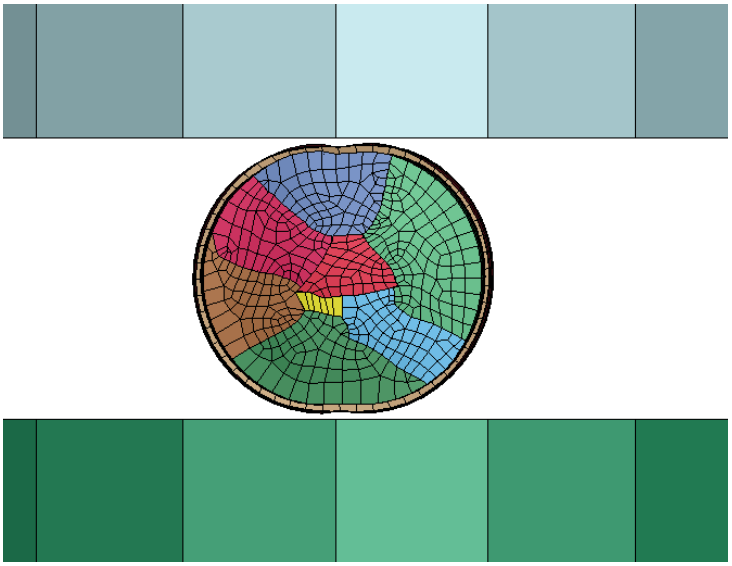

Figure E-62. ANSYS LSDYNA simulation snapshot.

The reaction load and displacement of the top fixture were plotted to visualize the force-displacement curve of this model. ANSYS LS-DYNA results were then compared with experimental data (Figure E-63). The force-displacement results from ANSYS LS-DYNA successfully captured the behavior of element failure as evidenced by the sudden drop in force when the pellet reached its failure strain and elements were deleted. After element deletion, there was less material to resist compression, thus resulting in a decreased force required to displace the rod.

However, it is noteworthy that when compared to the experimental data, the reaction force in ANSYS LS-DYNA was significantly higher. This indicates that the ANSYS LS-DYNA model is stiffer in the compression direction compared to the physical test sample. To address this discrepancy and to decrease the compressive stiffness of the finite element model, several potential options can be considered:

1. **Improve the material model.** Enhance the material model for the pellet, specifically considering its brittle nature. Implement a model that accurately captures the brittle behavior of the material.
2. **Input stress-strain curve.** Provide a detailed stress-strain curve for the pellet material to better characterize its behavior under compression.
3. **Utilize crack propagation tools.** Employ ANSYS crack propagation tools to simulate crack initiation and growth within the pellet which can significantly affect its mechanical response.
4. **Change pellet orientation.** Modify the orientation of the pellet with respect to the compression fixture. Adjusting the orientation can influence how the pellet responds to the applied load and could align the simulation more closely with experimental results.

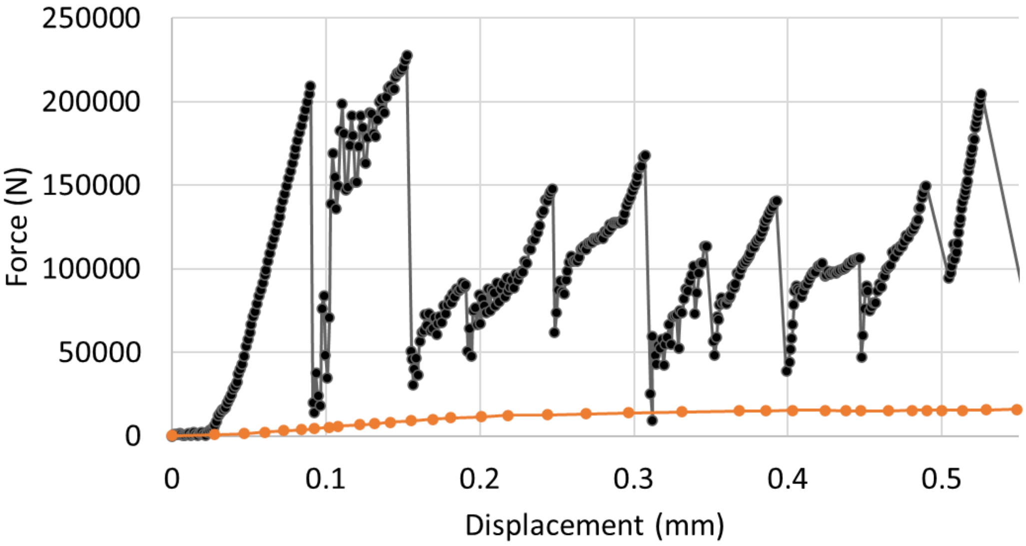

Figure E-63. ANSYS LSDYNA force displacement results.

By exploring these options and refining the simulation parameters, it may be possible to achieve a more accurate representation of the pellet-to-cladding behavior during the ring compression test and to bring the simulation results into better agreement with experimental data.

A final implicit, transient dynamic simulation of the sister rod undergoing a ring compression test was conducted using ANSYS transient analysis, which is a time history analysis. In this type of analysis, the displacement of the top fixture is defined as a function of time. Specifically, the top fixture was set to move 0.5 mm over a duration of 2 seconds, resulting in a rate of 0.25 mm/s. It's worth noting that this displacement rate is slower than what was used in ANSYS LS-DYNA. To enhance the chances of convergence, the displacement input was applied in multiple steps.

The force-displacement curve from the ANSYS transient model is shown in Figure E-64. It reveals that the reaction forces increase at a rate of 42 kN/mm between 0.1 mm and 0.3 mm of displacement. Notably, two distinct dips occur in the force-displacement curve. The first dip is observed at a displacement of 0.3 mm, and the second dip occurs at 0.48 mm. These dips are a consequence of pellet shifting within the model, thus leading to a reduction in the reaction force.

However, it is important to mention that the implicit, transient, dynamic simulation encountered convergence issues when displacement inputs exceeded 0.5 mm. At displacements beyond this threshold, the pellet movement becomes significant, increasing the complexity of the stiffness matrix and resulting in numerical instabilities.

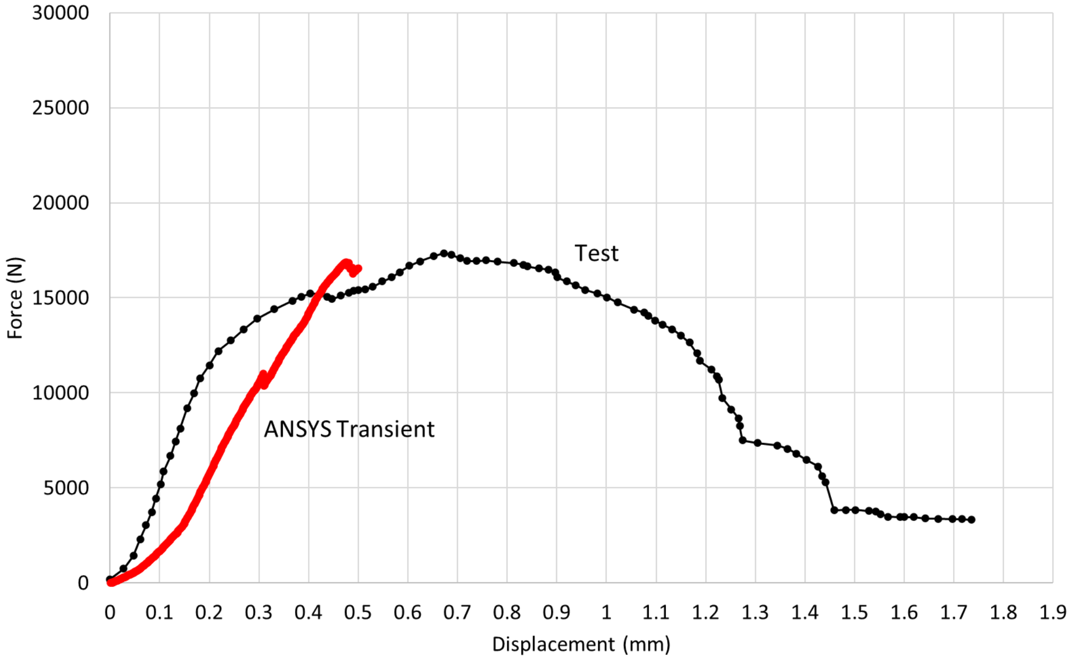

Figure E-64. ANSYS transient force vs. displacement results.

To improve this model and address convergence issues, several potential options can be considered:

1. **Increase friction coefficient.** Elevate the friction coefficient to enhance the compressive stiffness of the model, as demonstrated in Figure E-61.
2. **Set element failure criteria.** Implement element failure criteria within the pellet material to account for potential pellet failure under high compression loads.
3. **Change pellet orientation.** Alter the orientation of the pellet crack to influence its behavior under compression.
4. **Decrease load step size.** Apply the displacement in smaller increments to address the complexity of the model and to mitigate numerical instabilities.

By exploring these options and refining the model parameters, it may be possible to achieve more stable, more accurate results in the ANSYS transient analysis for the ring compression test of the sister rod.

E-6. Burst Tests

In FY21, ORNL investigated its existing equipment for use in burst testing fueled specimens. One goal of the burst tests is to capture aerosols released in the burst. To achieve this goal, a gas must be used to pressurize the test specimen, and the test must be conducted at RT. Given these criteria, the existing equipment is not capable of reaching the necessary pressure.

In FY22, ORNL has developed a pressurization system; however, pressures high enough to induce burst at RT have not been possible with this system.. In FY23, project personnel decided that burst tests of fueled segments were not needed. The SNF rods do not experience conditions in dry storage or transportation that would induce burst in a SNF rod, even in accident conditions.

In FY23, a quick connect system was developed to connect pressure fuel rod segments in the hot cell. The system was tested using surrogate fuel rod segments. The assembly was tested on the MiniMight using the 4PB fixturing and the aerosol collection apparatus. All components were found to work together without conflict and should be operable in the hot cell. The test assembly uses off-the-shelf Swagelok compression tube fittings (Figure E-65) and has been demonstrated to hold pressures up to 1,500 psi. Pressure is monitored by a miniature diaphragm pressure transducer (Omega PX600-2KGV). Procedures for attaching the Swagelok fittings in the hot cell were previously developed and have been adapted to an assembly jig (Figure E-65). The process will be implemented to pressurize 6-inch sister rod segments in the ORNL's IFEL in early FY 2024.

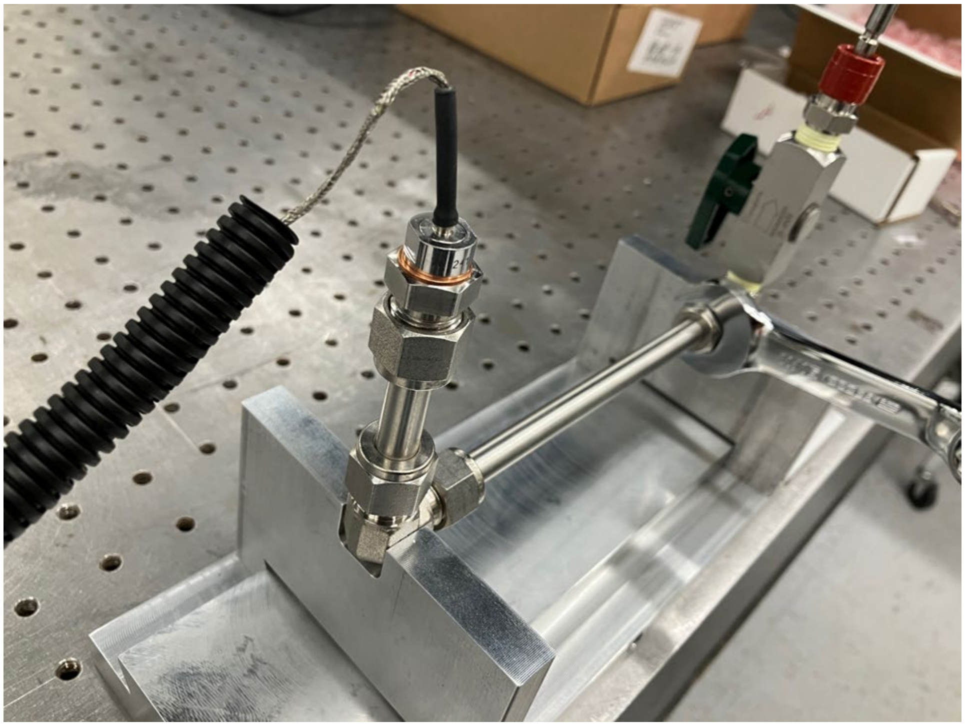

Figure E-65. Fuel rod segment test assembly resting in a special jig designed to allow final assembly and compression of fittings in the hot cell. The pressure transducer is visible in the top foreground with the data cable attached.

This page is intentionally blank.

References

[E-1.] *High Burnup Dry Storage Cask Research and Development Project: Final Test Plan*, Contract no. DE-NE-0000593, Electric Power Research Institute, Palo Alto, California (2014).

[E-2.] S. Saltzstein et al., *Visualization of the High Burnup Spent Fuel Rod Phase 1 Test Plan*, SAND2018-8042-O (2018).

[E-3.] R. A. Montgomery et al., *Post-Irradiation Examination Plan for High Burnup Demonstration Project Sister Rods*, SFWD-SFWST-2017-000090 ORNL/SR-2016/708, Oak Ridge National Laboratory, Oak Ridge, Tennessee, 2016.

[E-4.] ASTM International (2018). ASTM C1161 – 18: Standard Test Methods for Flexural Strength of Advanced Ceramics at Ambient Temperature. West Conshohocken, PA: American Society for Testing and Materials.

[E-5.] ASTM International (2015). ASTM D7264/D7264M – 15: Standard Test Methods for Flexural Properties of Polymer Matrix Composite Materials. West Conshohocken, PA: American Society for Testing and Materials.

[E-6.] ASTM International (2016). ASTM E8/E8M – 16a: Standard Test Methods for Tension Testing of Metallic Materials. West Conshohocken, PA: American Society for Testing and Materials.

[E-7.] R. A. Montgomery et al., *Sister Rod Nondestructive Examination Final Report*, SFWD-SFWST-2017-000003 Rev. 1 (M2SF-17OR010201021) / ORNL/SPR-2017/484 Rev. 1 (ORNL/SPR-2018/801), Oak Ridge National Laboratory, Oak Ridge, Tennessee, 2019.

[E-8.] R. W. Shimskey et al., *FY2020 Sibling Pin Testing Results,* M2SF-21PN010201055 / PNNL-31036, Pacific Northwest National Laboratory, Richland, Washington, 2020

[E-9.] M. C. Billone, *Ductility of High-Burnup-Fuel ZIRLO™ following Drying and Storage*, ANL-19/14, M2SF-19AN010201011 Rev. 3, Argonne National Laboratory, June 30, 2019.

[E-10.] J. RIBIS et al., "*Experimental and Modeling Approach of Irradiation Defects Recovery in Zirconium Alloys: Impact of an Applied Stress,*" Journal of ASTM International, **5**, 3, 2008.

[E-11.] M. Topping et al., "*Investigating the thermal stability of irradiation-induced damage in a zirconium alloy with novel in situ techniques*", Acta Materialia, 145, 255-263, 2017.

[E-12.] R. Einzinger and R. Kohli, "*Low-temperature Rupture Behavior of Zircaloy-Clad Pressurized Water Reactor Spent Fuel Rods Under Dry Storage Conditions*", Nuclear Technology, 67, 107-123, 1984.

[E-13.] M. Griffiths et al., "*Neutron Damage in Zirconium Alloys Irradiated at 644 and 710K*", Journal of Nuclear Materials, 150, 159-168, 1987.

[E-14.] H. R. Higgy and F. H. Hammond, "*Effect of Fast Neutron Irradiation on the Mechanical Properties of Some Zirconium Alloys and Stainless Steels*", Recent Advanced in Science and Technology, Volume 2, 391-408, 1974.

[E-15.] M.C. Billone, T.A. Burtseva, Y. Chen and Z. Han, Ductility of M5® and ZIRLO® Sibling Pin Cladding, M2SF-20AN010201012/ANL-20/47 (2020).

[E-16.] K. Geelhood, C. Beyer, and W. Luscher, "PNNL Stress/Strain Correlation for Zircaly," PNNL-17700, July 2008.

[E-17.] R. W. Shimskey et al., *PNNL FY 2021 Sibling Pin Testing Results*, M2SF-21PN010101057/PNNL-32783, Pacific Northwest National Laboratory, March 2022

[E-18.] J.-A. Wang et al., "FY 2016 Status Report: Documentation of All CIRFT Data including Hydride Reorientation Tests," ORNL/TM-2016/424, September 14, 2016.